ELECTRONIC PHOTODISSOCIATION SPECTROSCOPY OF IONS IN THE GAS PHASE

by

JASON E. COLLEY

(Under the Direction of Michael A. Duncan)

ABSTRACT

Electronic spectroscopy is employed to study the electronic structure and bonding of gas phase metal-ligand and carbon cluster ions. These ions are mass-selected and investigated using photodissociation spectroscopy. Metal ions such as Ag^+, Mg^+, Fe^+, and U^+ complexed with organic ligands like benzene are relevant as model systems for organometallic molecules, catalysts, charge transfer, and actinide chemistry. The bond dissociation energies of these complexes are determined by the onset wavelength of the photodissociation products. Carbon cluster cations are suspected to be in the interstellar medium, but their spectroscopy is difficult to measure. A new spectrum for C_6^+ was measured, consisting of a strong origin band, two vibronic bands, and four hot bands corresponding to a linear isomer. The deep UV spectroscopy of carbon clusters C_n^+, n = 6 – 20, is measured due to astrochemical relevance. These studies are accompanied by theoretical calculations to assign measured spectra and calculate bond dissociation energies.

INDEX WORDS: Laser Vaporization, Electronic Spectroscopy, Gas Phase Spectroscopy, Carbon Clusters, Uranium, Quantum Chemistry

ELECTRONIC PHOTODISSOCIATION SPECTROSCOPY OF IONS IN THE GAS-PHASE

by

JASON E. COLLEY

B.S., Troy University, 2017

A Dissertation Submitted to the Graduate Faculty of The University of Georgia in Partial Fulfillment of the Requirements for the Degree

DOCTOR OF PHILOSOPHY

ATHENS, GEORGIA

2024

ELECTRONIC PHOTODISSOCIATION SPECTROSCOPY OF IONS IN THE GAS-PHASE

by

JASON E. COLLEY

Major Professor:	Michael A. Duncan
Committee:	Melanie A. R. Reber
	Gary E. Douberly

Electronic Version Approved:

Ron Walcott
Vice Provost for Graduate Education and Dean of the Graduate School
The University of Georgia
May 2024

DEDICATION

I dedicate this work to my family, friends, and colleagues who supported me through these trying years in graduate school. A special thanks to my wife, Lindsey, who kept me strong through the worst of it. To Dylan, who worked with me and was there for me through the truly trying years. To Ian, Connor, Wade, Charles, and Dakota, coworkers all whose whimsy kept me sane in and out of the lab.

ACKNOWLEDGEMENTS

I would like to acknowledge Mike Duncan for giving me this opportunity to learn and grow as a scientist. I am especially grateful for all the direction he gave to my scientific work, and I truly admire his drive in his scientific pursuits and his respect for the storied history of our field. I would like to thank Dr. Gary Douberly and Dr. Melanie Reber for their efforts in my classroom instruction and their role on my committee. Finally, I'd like to thank the University of Georgia Department of Chemistry and the Georgia Advanced Computing Resource Center for providing me with the tools and the opportunity to pursue my doctoral studies.

TABLE OF CONTENTS

Page

LIST OF TABLES

Page

LIST OF FIGURES

Page

CHAPTER 1

INTRODUCTION AND REVIEW

Electronic spectroscopy provides a look into the fundamental properties of the electronic structure and the bonding of chemicals vital to physical phenomena throughout every field of science. The spectroscopy of ions is significant for gaining insight into a multitude of processes, such as the charge transfer of solar cells, single-atom catalysts, and the role of dopants in semiconductor efficiency. Spectroscopy of isolated ions in the gas phase provides information on their intrinsic properties without perturbations from solvation effects. This dissertation presents electronic spectroscopy of carbon cations as well as spectroscopy as a tool to investigate the bonding of metal ion complexes.

Bulk material has a myriad of physical properties that are strongly dependent on the chemical bonding and electronic structure of the composite particles. However, the properties of the bulk material can differ from those of the molecules. As such, investigating the characteristics of groupings of these particles, or clusters, can give insight into the chemical origin of these properties.[1-4] Clusters can be made up of anywhere from a few atoms or molecules to several hundred and lie in the nanometer size range. Metallic and semiconductor clusters in particular can have very different chemistry and electronic structures compared to their bulk material; as such, the structure, reactivity, and optical and electrical properties of a material depend (sometimes strongly) on the size of the cluster. Observing these attributes as the cluster size increases shows the progression toward bulk properties.[3] The effects of cluster size on a material's characteristics have implications for applied fields such as catalysis and

nanoelectronics. It is of great scientific interest to study the reactivity and bonding present in small clusters and their impact on the properties of bulk material.

Early scientific work on clusters used high-temperature Knudsen ovens to create clusters for mass spectrometer studies. Chupka,[5,6] Inghram,[5-7] and Drowart[7] made clusters of pure carbon with such ovens, though they only detected clusters up to C_5 whereas later experiments were able to observe much larger carbon clusters.[3] It is now understood that cluster growth occurs through collisions of vaporized atoms or molecules.[4] However, early studies had limited cluster concentrations due to the oven vaporization source. Additionally, the clusters created by an oven require extreme temperatures and are therefore very hot. Modern cluster sources include a gas to collisionally cool the resulting vapor. The lower internal temperature of molecules in the vapor also prevents fragmentation.[1,3] Other vaporization sources soon followed, including ion sputtering, discharge, and laser vaporization sources.[8-11] A distinct difference with these later sources is that, while they still mostly produce neutrals, they also produce ions, which can be studied with mass spectrometry to learn the vapor composition. Ion sputtering involves the bombardment of an inert gas on the surface of the sample material.[8-11] However, while larger cluster sizes can be created with this technique, this technique does not produce cold clusters, which limits the study of a wide distribution of ions to species that have high relative stability.

The laser vaporization source (also called the "Smalley source") was developed in 1981 simultaneously by the Smalley group at Rice University[12-17] and by Dr. Vladimir Bondybey at AT&T Laboratories.[18] While lasers were used previous to the development of this technique,[19-23] these were the first labs to employ a collisional gas to cool the resulting metal vapor. Smalley's experimental design allowed the collisional gas to be pulsed over the vaporization site for cooling, allowing for studies of cold ions in a molecular beam. The first applications utilizing

this ion source were fundamental studies of metal atom clusters composed of transition metals[13-15] and main group metals[12,24,25]. Afterward, laser vaporization has shown its versatility for sourcing ions of carbon,[26-30] silicon,[30,31] and germanium clusters.[31,32] The laser vaporization target can be made of an alloy to observe mixed clusters.[32-35] Furthermore, solvents can be added to the gas flow in order to form clusters and complexes with the metal material.[36] Similarly, the same can be achieved by coating the metal target with a film, where the laser will penetrate the film.[37-39] The laser vaporization source can create a multitude of metal and mixed clusters, neutral and ionic.

Much scientific work has been done on mixed metal clusters in the gas phase. Clusters of metal carbides were created using a laser vaporization source with a hydrocarbon collisional gas; the plasma of the laser vaporization eliminates the hydrogen from the hydrocarbon molecule which will bind to the metal vapor.[40-46] The efficiency of metal carbide production heavily relies on the metal used, where less-reactive metals will not readily eliminate the hydrogen and instead form metal-hydrocarbon complexes (though these also have scientific relevance).[47] Instead, it may be more efficient to coat a *carbon* rod with vaporized metal,[37,38] which has been done to study copper and gold carbides.[48,49] Similar mixed clusters have been made with silane and O_2 as the collision gas, giving rise to metal silicon[48-52] and metal oxide clusters.[53-63]

The laser vaporization source can create many different assemblies of metal cluster ions. Additionally, the vaporization site can be altered to further control the types of clusters made. As Ref. 44 details, when the vaporization occurs in an enclosed space and the collisional gas carries the resulting plasma through a channel, the ions created are given time to condense further. In this way, the solvation of metal with inert gases,[64-74] water,[75-81] and organic ligands[82-89] (to name a few) can be observed and investigated. More still can be studied when the metal ion produced

is doubly charged.[77,78,80,81,90,91] Laser vaporization can be used in conjunction with other ion sources to create mixed ions in the gas phase.[92-98]

Many different experiments have investigated clusters produced by a laser vaporization source,[12-15,24-98] the earliest of which would of course be the identification of ions produced using mass spectrometry.[12,15,24-36,40,44,53,55,58] A time-of-flight mass spectrometer provides the exceptional capability to isolate an ion size for further study. For instance, ion mobility measurements were used to categorize the different 3D structures that an ion size can exhibit.[99,100] These experiments were used to characterize the chain, ring, and cage structures of carbon clusters in various sizes.[101] Further structural information can be provided by infrared spectroscopy. Many of the ion clusters discussed are loosely held together with van der Waals forces more so than covalent bonds, which are only stable at sub-100 K temperatures. When enough energy is inserted into the complex, it is a statistical eventuality that enough of the energy will distribute into the vibration displacing the molecule from the ion, which will result in the complex dissociating; this process is called intramolecular vibrational energy redistribution (IVR).[102,103] The density of these ions is too low to detect their absorbance; however, measuring the photodissociation of these ion complexes following IVR allows one to observe their absorption spectra.

Photodissociation spectroscopy has been used to investigate many clustered ions in the gas phase.[28,44,54-56,61-64,66-86,89,103] This process requires the photon energy to be greater than the binding energy of the complex, so the studies of many species are limited to their electronic spectroscopy. However, some complexes are produced with loosely bound inert gases such as N_2, H_2, or rare gases; in such cases, an infrared photon may have enough energy to overcome the binding energy; in this way, the vibrational spectra of metal complexes can be

measured.[67,71,75,79,80,81,89,104-106] Specifically, significant work has been done on metallocarbohedrenes (called "Met-Cars"),[44-46,53] metal ion-carbonyl,[74] and metal ion-benzene complexes,[89] measuring their binding and structure. A related experiment is collision-induced dissociation, where mass-selected ion complexes are passed through a collision cell at a known kinetic energy in order to measure their bond dissociation energy.[107-112] This will be discussed more in Chapter 3. Photodissociation spectroscopy is an excellent tool for investigating the chemistry and structure of ions without the perturbation of solvation effects and for benchmarking the accuracy of theoretical approach development.

The primary motivation behind the research presented herein is to better understand the electronic structure of complexes and clusters, namely metal ion-ligand complexes and carbon cluster cations. These species prove challenging for theoretical chemistry to accurately describe, and there is a lack of experimental data necessary for a complete picture of them. The electronic spectroscopy of a species in the gas phase would provide insight into the chemistry of these species without perturbations from solvation effects that convolute their interactions. Chapter 2 presents the apparatus with which photodissociation spectroscopy of mass-selected ions is measured. Chapters 3 and 4 present the findings on the electronic spectroscopy of metal ion-ligand complexes and carbon cluster cations, respectively.

REFERENCES

1. Mingos, D. M. P. *Introduction to Cluster Chemistry*; Englewood Cliffs, N.J. : Prentice Hall, 1990.
2. Duncan, M. A. *Advances in Metal and Semiconductor Clusters: Cluster Materials*, 1st edition.; JAI Press, 1998.
3. *Clusters of Atoms and Molecules: Theory, Experiment, and Clusters of Atoms*, Softcover reprint of the original 1st ed. 1994 edition.; Haberland, H., Ed.; Springer: Berlin, 2011.
4. Johnson, R.; Johnston, R. L. *Atomic & Molecular Clusters*, 1st edition.; CRC Press: London, 2002.
5. Chupka, W. A.; Inghram, M. G. Investigation of the Heat of Vaporization of Carbon. *J. Chem. Phys.* **1953**, *21*, 371–372.
6. Chupka, W. A.; Inghram, M. G. Direct Determination of the Heat of Sublimation of Carbon. *J. Chem. Phys.* **1954**, *22*, 1472.
7. Drowart, J.; Burns, R. P.; DeMaria, G.; Inghram, M. G. Mass Spectrometric Study of Carbon Vapor. *J. Chem. Phys.* **1959**, *31*, 1131–1132.
8. Behrisch, R.; Hauffe, W.; Hofer, W. O.; Laegreid, N.; McClanahan, E. D.; Sundqvist, B. U. R.; Wittmaack, K. *Sputtering by Particle Bombardment III: Characteristics of Sputtered Particles, Technical Applications*, Softcover reprint of the original 1st ed. 1991 edition.; Behrisch, R., Wittmaack, K., Eds.; Springer, 2014.
9. (a) Leleyter, M.; Ortoli, S.; Joyes, P. Secondary Emission of Ti_pC_n Ions from TiC Alloy. *Sur. Sci.* **1981**, *106*, 293–300. (b) Leleyter, M.; Joyes, P. SIMS Study of Normal and Transition Element Carbides. *Sur. Sci.* **1985**, *156*, 800–813.

10. Yamamoto, H.; Asaoka, H. Formation of Binary Clusters by Molecular Ion Irradiation. *Appl. Sur. Sci.* **2001**, *169*, 305–309.

11. Belykh, S. F.; Rasulev, U. K.; Samartsev, A. V.; Stroev, L. V.; Zinoviev, A. V. High Non-Additive Sputtering of Silicon as Large Positive Cluster Ions under Polyatomic Ion Bombardment. *Vacuum* **2000**, *56*, 257–262.

12. Dietz, T. G.; Duncan, M. A.; Powers, D. E.; Smalley, R. E. Laser Production of Supersonic Metal Cluster Beams. *J. Chem. Phys.* **1981**, *74*, 6511–6512.

13. Powers, D. E.; Hansen, S. G.; Geusic, M. E.; Puiu, A. C.; Hopkins, J. B.; Dietz, T. G.; Duncan, M. A.; Langridge-Smith, P. R. R.; Smalley, R. E. Supersonic Metal Cluster Beams: Laser Photoionization Studies of Cu_2. *J. Chem. Phys.* **1982**, *86*, 2556–2560.

14. Powers, D. E.; Hansen, S. G.; Geusic, M. E.; Michalopoulos, D. L.; Smalley, R. E. Supersonic Copper Clusters. *J. Chem. Phys.* **1983**, *78*, 2866–2881.

15. Zheng, L. -S.; Brucat, P. J.; Pettiette, C. L.; Yang, S.; Smalley, R. E. Formation and Photodetachment of Cold Metal Cluster Negative Ions. *J. Chem. Phys.* **1985**, *83*, 4273–4274.

16. Brucat, P. J.; Zheng, L. -S.; Pettiette, C. L.; Yang, S.; Smalley, R. E. Metal Cluster Ion Photofragmentation. *J. Chem. Phys.* **1986**, *84*, 3078–3088.

17. Maruyama, S.; Anderson, L. R.; Smalley, R. E. Direct Injection Supersonic Cluster Beam Source for FT-ICR Studies of Clusters. *Rev. Sci. Instrum.* **1990**, *61*, 3686–3693.

18. Bondybey, V. E.; English, J. H. Laser Induced Fluorescence of Metal Clusters Produced by Laser Vaporization: Gas Phase Spectrum of Pb_2. *J. Chem. Phys.* **1981**, *74*, 6978–6979.

19. Lincoln, K. A. Improved Instrumentation for Time-Resolved Mass Spectrometry with Application to Laser-Vaporization of Solid Materials. *Int. J. Mass Spectrom. Ion Processes* **1969**, *2*, 75–83.

20. Friichtenicht, J. F. Laser-generated Pulsed Atomic Beams. *Rev. Sci. Instrum.* **1974**, *45*, 51–56.

21. Utterback, N. G.; Tang, S. P.; Friichtenicht, J. F. Atomic and Ionic Beam Source Utilizing Pulsed Laser Blow Off. *Phys. Fluids* **1976**, *19*, 900–905.

22. Wicke, B. G.; Utterback, N. G.; Tang, S. P.; Friichtenicht, J. F. Comment on Pulsed High-density Source of Cesium Atoms. *Rev. Sci. Instrum.* **1980**, *51*, 151–153.

23. Bingham, R. A.; Salter, P. L. Analysis of Solid Materials by Laser Probe Mass Spectrometry. *Anal. Chem.* **1976**, *48*, 1735–1740.

24. LaiHing, K.; Wheeler, R. G.; Wilson, W. L.; Duncan, M. A. Photoionization Dynamics and Abundance Patterns in Laser Vaporized Tin and Lead Clusters. *J. Chem. Phys.* **1987**, *87*, 3401–3409.

25. Geusic, M. E.; Freeman, R. R.; Duncan, M. A. Neutral and Ionic Clusters of Antimony and Bismuth: A Comparison of Magic Numbers. *J. Chem. Phys.* **1988**, *89*, 223–229.

26. Rohlfing, E. A.; Cox, D. M.; Kaldor, A. Production and Characterization of Supersonic Carbon Cluster Beams. *J. Chem. Phys.* **1984**, *81*, 3322–3330.

27. Kroto, H. W.; Heath, J. R.; O'Brien, S. C.; Curl, R. F.; Smalley, R. E. C_{60}: Buckminsterfullerene. *Nature* **1985**, *318*, 162–163.

28. Geusic, M. E.; Jarrold, M. F.; McIlrath, T. J.; Freeman, R. R.; Brown, W. L. Photodissociation of Carbon Cluster Cations. *J. Chem. Phys.* **1987**, *86*, 3862–3869.

29. Heath, J. R.; Zhang, Q.; O'Brien, S. C.; Curl, R. F.; Kroto, H. W.; Smalley, R. E. The Formation of Long Carbon Chain Molecules during Laser Vaporization of Graphite. *J. Am. Chem. Soc.* **1987**, *109*, 359–363.

30. Bloomfield, L. A.; Geusic, M. E.; Freeman, R. R.; Brown, W. L. Negative and Positive Cluster Ions of Carbon and Silicon. *Chem. Phys. Lett.* **1985**, *121*, 33–37.

31. Heath, J. R.; Liu, Y.; O'Brien, S. C.; Zhang, Q.-L.; Curl, R. F.; Tittel, F. K.; Smalley, R. E. Semiconductor Cluster Beams: One- and Two-Color Ionization Studies of Si_x and Ge_x. *J. Chem. Phys.* **1985**, *83*, 5520–5526.

32. O'Brien, S. C.; Liu, Y.; Zhang, Q.; Heath, J. R.; Tittel, F. K.; Curl, R. F.; Smalley, R. E. Supersonic Cluster Beams of III–V Semiconductors: Ga_xAs_y. *J. Chem. Phys.* **1986**, *84*, 4074–4079.

33. Rohlfing, E. A.; Cox, D. M.; Petkovic-Luton, R.; Kaldor, A. Alloy Cluster Beams: Nickel/Chromium and Nickel/Aluminum. *J. Phys. Chem.* **1984**, *88*, 6227–6231.

34. Wheeler, R. G.; LaiHing, K.; Wilson, W. L.; Allen, J. D.; King, R. B.; Duncan, M. A. Neutral Gas-Phase Analogs of Condensed-Phase Post-Transition-Metal Cluster Ions: Laser Vaporization and Photoionization of Tin-Bismuth and Lead-Antimony Alloys. *J. Am. Chem. Soc.* **1986**, *108*, 8101–8102.

35. Wheeler, R. G.; LaiHing, K.; Wilson, W. L.; Duncan, M. A. Growth Patterns in Binary Clusters of Group IV and V Metals. *J. Chem. Phys.* **1988**, *88*, 2831–2839.

36. LaiHing, K.; Cheng, P. Y.; Duncan, M. A. Ultraviolet Photolysis in a Laser Vaporization Cluster Source: Synthesis of Novel Mixed-Metal Clusters. *J. Phys. Chem.* **1987**, *91*, 6521–6525.

37. Yeh, C. S.; Robbins, D. L.; Pilgrim, J. S.; Duncan, M. A. Photoionization Electronic Spectroscopy of AgK. *Chem. Phys. Lett.* **1993**, *206*, 509–514.

38. Brock, L. R.; Pilgrim, J. S.; Duncan, M. A. Photoionization Spectroscopy of LiAl. *Chem. Phys. Lett.* **1994**, *230*, 93–98.

39. Brock, L. R.; Knight, A. M.; Reddic, J. E.; Pilgrim, J. S.; Duncan, M. A. Photoionization Spectroscopy of Ionic Metal Dimers: LiCu and LiAg. *J. Chem. Phys.* **1997**, *106*, 6268–6278.

40. Guo, B. C.; Kerns, K. P.; Castleman, A. W. $Ti_8C_{12}^+$-Metallo-Carbohedrenes: A New Class of Molecular Clusters? *Science* **1992**, *255*, 1411–1413.

41. Guo, B. C.; Wei, S.; Purnell, J.; Buzza, S.; Castleman Jr, A. W. Metallo-Carbohedrenes [$M_8C_{12}^+$ (M= V, Zr, Hf, and Ti)]: A Class of Stable Molecular Cluster Ions. *Science* **1992**, *256*, 515–516.

42. Wei, S.; Guo, B. C.; Purnell, J.; Buzza, S.; Castleman Jr, A. W. Metallo-Carbohedrenes: Formation of Multicage Structures. *Science* **1992**, *256*, 818–820.

43. Castleman, A. W. Met-Cars: A New Family of Metal - Carbon Clusters. In *Applications of Organometallic Chemistry in the Preparation and Processing of Advanced Materials*; Harrod, J. F., Laine, R. M., Eds.; Springer Netherlands: Dordrecht, 1995.

44. Pilgrim, J. S.; Duncan, M. A. Photodissociation of Metallo-Carbohedrene ("Met-Cars") Cluster Cations. *J. Am. Chem. Soc.* **1993**, *115*, 4395–4396.

45. Pilgrim, J. S.; Duncan, M. A. Metallo-Carbohedrenes: Chromium, Iron, and Molybdenum Analogs. *J. Am. Chem. Soc.* **1993**, *115*, 6958–6961.

46. Pilgrim, J. S.; Duncan, M. A. Beyond Metallo-Carbohedrenes: Growth and Decomposition of Metal-Carbon Nanocrystals. *J. Am. Chem. Soc.* **1993**. *115*, 9724–9727.

47. Duncan, M. A. Invited Review Article: Laser Vaporization Cluster Sources. *Rev. Sci. Instrum.* **2012**, *83*, 041101.

48. Beck, S. M. Studies of Silicon Cluster–Metal Atom Compound Formation in a Supersonic Molecular Beam. *J. Chem. Phys.* **1987**, *87*, 4233–4234.

49. Beck, S. M. Mixed Metal–Silicon Clusters Formed by Chemical Reaction in a Supersonic Molecular Beam: Implications for Reactions at the Metal/Silicon Interface. *J. Chem. Phys.* **1989**, *90*, 6306–6312.

50. Beck, S. M. Photophysical Studies of Bare and Metal-Containing Silicon Clusters. *Adv. Metal & Semicon. Clusters* **1993**, *1*, 241.

51. Hiura, H.; Miyazaki, T.; Kanayama, T. Formation of Metal-Encapsulating Si Cage Clusters. *Phys. Rev. Lett.* **2001**, *86*, 1733–1736.

52. Negishi, A.; Kariya, N.; Sugawara, K.; Arai, I.; Hiura, H.; Kanayama, T. Size-Selective Formation of Tungsten Cluster-Containing Silicon Cages by the Reactions of W_n^+(n=1–5) with SiH_4. *Chem. Phys. Lett.* **2004**, *388*, 463–467.

53. Reddic, J. E.; Duncan, M. A. Composite Samples and the Generation of Novel Metal Carbide Clusters. *Chem. Phys. Lett.* **1997**, *264*, 157–162.

54. Ticknor, B. W.; Bandyopadhyay, B.; Duncan, M. A. Photodissociation of Noble Metal-Doped Carbon Clusters. *J. Phys. Chem. A* **2008**, *112*, 12355–12366.

55. Deng, H. T.; Kerns, K. P.; Castleman, A. W. Formation, Structures, and Reactivities of Niobium Oxide Cluster Ions. *J. Phys. Chem.* **1996**, *100*, 13386–13392.

56. Kooi, S. E.; Castleman, A. W. Photofragmentation of Vanadium Oxide Cations. *J. Phys. Chem. A* **1999**, *103*, 5671–5674.

57. Bell, R. C.; Zemski, K. A.; Justes, D. R.; Castleman, A. W., Jr. Formation, Structure and Bond Dissociation Thresholds of Gas-Phase Vanadium Oxide Cluster Ions. *J. Chem. Phys.* **2001**, *114*, 798–811.

58. Foltin, M.; Stueber, G. J.; Bernstein, E. R. On the Growth Dynamics of Neutral Vanadium Oxide and Titanium Oxide Clusters. *J. Chem. Phys.* **1999**, *111*, 9577–9586.

59. Foltin, M.; Stueber, G. J.; Bernstein, E. R. Investigation of the Structure, Stability, and Ionization Dynamics of Zirconium Oxide Clusters. *J. Chem. Phys.* **2001**, *114*, 8971–8989.

60. Shin, D. N.; Matsuda, Y.; Bernstein, E. R. On the Iron Oxide Neutral Cluster Distribution in the Gas Phase. II. Detection through 118 nm Single Photon Ionization. *J. Chem. Phys.* **2004**, *120*, 4157–4164.

61. Molek, K. S.; Jaeger, T. D.; Duncan, M. A. Photodissociation of Vanadium, Niobium, and Tantalum Oxide Cluster Cations. *J. Chem. Phys.* **2005**, *123*, 144313.

62. Molek, K. S.; Reed, Z. D.; Ricks, A. M.; Duncan, M. A. Photodissociation of Chromium Oxide Cluster Cations. *J. Phys. Chem. A* **2007**, *111*, 8080–8089.

63. Molek, K. S.; Anfuso-Cleary, C.; Duncan, M. A. Photodissociation of Iron Oxide Cluster Cations. *J. Phys. Chem. A* **2008**, *112*, 9238–9247.

64. Buthelezi, T.; Bellert, D.; Lewis, V.; Brucat, P. J. The C ← X Transition in $CaKr^+$ and $CaAr^+$. *Chem. Phys. Lett.* **1995**, *246*, 145–149.

65. Bellert, D.; Buthelezi, T.; Hayes, T.; Brucat, P. J. The Binding Energy and Vibronic Structure of $NbXe^+$. *Chem. Phys. Lett.* **1997**, *277*, 27–32.

66. Hayes, T.; Bellert, D.; Buthelezi, T.; Brucat, P. J. The Bond Length of VAr^+. *Chem. Phys. Lett.* **1998**, *287*, 22–28.

67. Velegrakis, M. Stability, Structure and Optical Properties of Metal-Ion Doped Noble Gas Clusters. *Adv. Met. Semicon. Clusters* **2001**, *5*, 227-265.

68. Asher, R. L.; Bellert, D.; Buthelezi, T.; Brucat, P. J. Optical Excitation of $Co^+ \cdot N_2$. *J. Phys. Chem.* **1955**, *99*, 1068–1072.

69. Asher, R. L.; Bellert, D.; Buthelezi, T.; Brucat, P. J. The $Co^+ \cdot CO_2$ Electrostatic Complex: Geometry and Potential. *Chem. Phys. Lett.* **1994**, *227*, 623–627.

70. Asher, R. L.; Bellert, D.; Buthelezi, T.; Weerasekera, G.; Brucat, P. J. The Binding Energy of $Ni^+ \cdot CO_2$. *Chem. Phys. Lett.* **1994**, *228*, 390–392.

71. Bellert, D.; Buthelezi, T.; Brucat, P. J. The Structure of $Co^+ \cdot OCO$. *Chem. Phys. Lett.* **1998**, *290*, 316–322.

72. Ricks, A. M.; Bakker, J. M.; Douberly, G. E.; Duncan, M. A. IR Spectroscopy of $Co^+(CO)_n$ Complexes in the Gas Phase. *J. Phys. Chem. A* **2009**, *113*, 4701–4708.

73. Ricks, A. M.; Reed, Z. D.; Duncan, M. A. Seven-Coordinate Homoleptic Metal Carbonyls in the Gas Phase. *J. Am. Chem. Soc.* **2009**, *131*, 9176–9177.

74. Ricks, A. M.; Reed, Z. E.; Duncan, M. A. Infrared Spectroscopy of Mass-Selected Metal Carbonyl Cations. *J. Mol. Spectrosc.* **2011**, *266*, 63–74.

75. Lessen, D. E.; Asher, R. L.; Brucat, P. J. Vibrational Structure of an Electrostatically Bound Ion–Water Complex. *J. Chem. Phys.* **1990**, *93*, 6102–6103.

76. Sanekata, M.; Misaizu, F.; Fuke, K. Photodissociation Study on $Ca^+(H_2O)_n$, n=1–6: Electron Structure and Photoinduced Dehydrogenation Reaction. *J. Chem. Phys.* **1996**, *104*, 9768–9778.

77. Thompson, C. J.; Husband, J.; Aguirre, F.; Metz, R. B. Photodissociation Dynamics of Hydrated Ni^{2+} Clusters: $Ni^{2+}(H_2O)_n$ (n = 4−7). *J. Phys. Chem. A* **2000**, *104*, 8155–8159.

78. Faherty, K. P.; Thompson, C. J.; Aguirre, F.; Michne, J.; Metz, R. B. Electronic Spectroscopy and Photodissociation Dynamics of Hydrated Co^{2+} Clusters: $Co^{2+}(H_2O)_n$ (n = 4−7). *J. Phys. Chem. A* **2001**, *105*, 10054–10059.

79. Walters, R. S.; Pillai, E. D.; Duncan, M. A. Solvation Dynamics in $Ni^{+}(H_2O)_n$ Clusters Probed with Infrared Spectroscopy. *J. Am. Chem. Soc.* **2005**, *127*, 16599–16610.

80. Carnegie, P. D.; Bandyopadhyay, B.; Duncan, M. A. Infrared Spectroscopy of $Cr^{+}(H_2O)$ and $Cr^{2+}(H_2O)$: The Role of Charge in Cation Hydration. *J. Phys. Chem. A* **2008**, *112*, 6237–6243.

81. Carnegie, P. D.; Bandyopadhyay, B.; Duncan, M. A. Infrared Spectroscopy of $Sc^{+}(H_2O)$ and $Sc^{2+}(H_2O)$ via Argon Complex Predissociation: The Charge Dependence of Cation Hydration. *J. Chem. Phys.* **2011**, *134*, 014302.

82. Hayes, T.; Bellert, D.; Buthelezi, T.; Brucat, P. J. The Photodissociation of $V^{+}\cdot CH_4$. *Chem. Phys. Lett.* **1997**, *264*, 220–224.

83. Kleiber, P. D.; Chen, J. Spectroscopy and Chemical Dynamics of Weakly Bound Alkaline-Earth Metal Ion-H and Alkaline-Earth Metal Ion-Hydrocarbon Complexes 2. *Int. Rev. Phys. Chem.* **1998**, *17*, 1–34.

84. Chen, J.; Wong, T.-H.; Kleiber, P. D.; Yang, K.-H. Photofragmentation Spectroscopy of $Al^{+}(C_2H_4)$. *J. Chem. Phys.* **1999**, *110*, 11798–11805.

85. Husband, J.; Aguirre, F.; Thompson, C. J.; Laperle, C. M.; Metz, R. B. Photofragment Spectroscopy of $FeCH_2^+$, $CoCH_2^+$, and $NiCH_2^+$ near the $M^+–CH_2$ Dissociation Threshold. *J. Phys. Chem. A* **2000**, *104*, 2020–2024.

86. Kleiber, P. D. Photodissociation Spectroscopy as a Probe of Molecular Dynamics: Metal Ion-Ethylene Interactions. *Adv. Met. Semicon. Clusters* **2001** *5*, 267–294.

87. Sohnlein, B. R.; Yang, D.-S. Pulsed-Field Ionization Electron Spectroscopy of Group 6 Metal (Cr, Mo, and W) Bis(Benzene) Sandwich Complexes. *J. Chem. Phys.* **2006**, *124*, 134305.

88. Sohnlein, B. R.; Lei, Y.; Yang, D.-S. Electronic States of Neutral and Cationic Bis(Benzene) Titanium and Vanadium Sandwich Complexes Studied by Pulsed Field Ionization Electron Spectroscopy. *J. Chem. Phys.* **2007**, *127*, 114302.

89. Duncan, M. A. Structures, Energetics and Spectroscopy of Gas Phase Transition Metal Ion–Benzene Complexes. *Int. J. Mass Spectrom.* **2008**, *272*, 99–118.

90. Velegrakis, M.; Lüder, Ch. Formation and Stability of Singly and Doubly Charged $MgAr_n$ Clusters. *Chem. Phys. Lett.* **1994**, *223*, 139–142.

91. Walker, N. R.; Grieves, G. A.; Jaeger, J. B.; Walters, R. S.; Duncan, M. A. Generation of "Unstable" Doubly Charged Metal Ion Complexes in a Laser Vaporization Cluster Source. *Int. J. Mass Spectrom.* **2003**, *228*, 285–295.

92. Jarrold, M. F.; Bower, J. E.; Kraus, J. S. Collision Induced Dissociation of Metal Cluster Ions: Bare Aluminum Clusters, Al^+_n (n= 3–26). *J. Chem. Phys.* **1987**, *86*, 3876–3885.

93. Tast, F.; Malinowski, N.; Frank, S.; Heinebrodt, M.; Billas, I. M. L.; Martin, T. P. Transition Metal Coated Fullerenes. *Z. Phys. D* **1997**, *40*, 351–354.

94. Branz, W.; Billas, I. M. L.; Malinowski, N.; Tast, F.; Heinebrodt, M.; Martin, T. P. Cage Substitution in Metal–Fullerene Clusters. *J. Chem. Phys.* **1998**, *109*, 3425–3430.

95. Duncan, M. A.; Knight, A. M.; Negishi, Y.; Nagao, S.; Nakamura, Y.; Kato, A.; Nakajima, A.; Kaya, K. Production of Jet-Cooled Coronene and Coronene Cluster Anions and Their Study with Photoelectron Spectroscopy. *Chem. Phys. Lett.* **1999**, *309*, 49–54.

96. Duncan, M. A.; Knight, A. M.; Negishi, Y.; Nagao, S.; Judai, K.; Nakajima, A.; Kaya, K. Photoelectron Spectroscopy of $V_x(Coronene)_y$ and $Ti_x(Coronene)_y$ Anions. *J. Phys. Chem. A* **2001**, *105*, 10093–10097.

97. Sun, M.; Halfen, D. T.; Min, J.; Harris, B.; Clouthier, D. J.; Ziurys, L. M. The Rotational Spectrum of CuCCH($\tilde{X}\ ^1\Sigma^+$): A Fourier Transform Microwave Discharge Assisted Laser Ablation Spectroscopy and Millimeter/Submillimeter Study. *J. Chem. Phys.* **2010**, *133*, 174301.

98. Lee, J. S.; Krasnokutski, S. A.; Yang, D.-S. High-Resolution Electron Spectroscopy, Preferential Metal-Binding Sites, and Thermochemistry of Lithium Complexes of Polycyclic Aromatic Hydrocarbons. *J. Chem. Phys.* **2011**, *134*, 024301.

99. Shvartsburg, A. A.; Hudgins, R. R.; Dugourd, P.; Jarrold, M. F. Structural Information from Ion Mobility Measurements: Applications to Semiconductor Clusters. *Chem. Soc. Rev.* **2001**, *30*, 26–35.

100. Ibrahim, Y.; Alsharaeh, E.; Mabrouki, R.; Momoh, P.; Xie, E.; El-Shall, M. S. Ion Mobility of Ground and Excited States of Laser-Generated Transition Metal Cations. *J. Phys. Chem. A* **2008**, *112*, 1112–1124.

101. von Helden, G.; Hsu, M. T.; Gotts, N.; Bowers, M. T. Carbon Cluster Cations with up to 84 Atoms: Structures, Formation Mechanism, and Reactivity. *J. Phys. Chem*. **1993**, *97*, 8182–8192.

102. Bondybey, V. E. Relaxation and Vibrational Energy Redistribution Processes in Polyatomic Molecules. *Annu. Rev. Phys. Chem*. **1984**, *35*, 591–612.

103. Boyall, D.; L. Reid, K. Modern Studies of Intramolecular Vibrational Energy Redistribution. *Chem. Soc. Rev.* **1997**, *26*, 223–232.

104. Duncan, M. A. Spectroscopy of Metal Ion Complexes: Gas-Phase Models for Solvation. *Annu. Rev. Phys. Chem*. **1997**, *48*, 69–93.

105. Duncan, M. A. Infrared Spectroscopy to Probe Structure and Dynamics in Metal Ion-Molecule Complexes. *Int. Rev. Phys. Chem*. **2003**, *22*, 407–435.

106. Walker, N. R.; Walters, R. S.; Duncan, M. A. Frontiers in the Infrared Spectroscopy of Gas Phase Metal Ion Complexes. *New J. Chem*. **2005**, *29*, 1495–1503.

107. Rodgers, M. T.; Armentrout, P. B. Cationic Noncovalent Interactions: Energetics and Periodic Trends. *Chem. Rev.* **2016**, *116*, 5642–5687.

108. Meyer, F.; Khan, F. A.; Armentrout, P. B. Thermochemistry of Transition Metal Benzene Complexes: Binding Energies of $M(C_6H_6)_x^+$ (x = 1, 2) for M= Ti to Cu. *J. Am. Chem. Soc.* **1995**, *117*, 9740–9748.

109. Armentrout, P. B. Reactions and Thermochemistry of Small Transition Metal Cluster Ions. *Annu. Rev. Phys. Chem*. **2001**, *52*, 423–461.

110. Armentrout, P. B.; Braga, D.; Dedieu, A.; Gisdakis, P.; Görling, A.; Grepioni, F.; Maseras, F.; Rösch, N.; Trickey, S. B. *Organometallic Bonding and Reactivity:*

Fundamental Studies; Brown, J. M., Hofmann, P., Eds.; Springer: Berlin Heidelberg, 1999.

111. Rowland, T. G.; Sztáray, B.; Armentrout, P. B. Metal–Cyclopentadienyl Bond Energies in Metallocene Cations Measured Using Threshold Collision-Induced Dissociation Mass Spectrometry. *J. Phys. Chem. A* **2013**, *117*, 1299–1309.
112. Armentrout, P. B. Methane Activation by 5d Transition Metals: Energetics, Mechanisms, and Periodic Trends. *Chem. Eur. J.* **2017**, *23*, 10–18.

CHAPTER 2

EXPERIMENTAL AND THEORETICAL METHODS

EXPERIMENTAL APPARATUS

Laser vaporization has been well-studied and has been described in Chapter 1 and elsewhere.[1,2] Most metals will break down and ablate under sufficient laser fluence, ejecting neutral and ionized atoms and electrons as plasma. The density of the plasma is such that condensation and recombination can occur, even in a vacuum. Recombination can proceed such that a cluster can grow in the plasma, especially when a collision gas is introduced. Additionally, the metal neutrals and ions can form complexes with the collision gas. In this way, metal ion complexes are created via laser vaporization of a metal rod in the presence of a collision gas. The metal rod is rotated and translated to keep a fresh metal surface at the vaporization site. The second or third harmonics of a focused, pulsed Nd:YAG laser (532 and 355 nm, respectively) are used as the vaporization laser. The vaporization occurs in a vacuum chamber, where the resulting plasma is cooled by the supersonic expansion of a gas. The gas is pulsed into the chamber using a Series 9 General Valve by Parker Hannifin Corp. The vaporization of metal creates a hot plasma where reactions with the expansion gas may occur. As the cooling efficiency of the expansion depends on the makeup of the gas, a mix of gases may be used for the expansion to efficiently cool while still having reactions (e.g. 1% acetylene in argon for metal ion-acetylene complexation). Furthermore, liquid can be added to the gas lines to have an expansion gas seeded with a potential ligand, such as benzene or toluene. The extent of this reaction can be controlled by changing the expansion gas (argon, helium, carbon dioxide, etc.), the vaporization

laser wavelength, and the source block that holds the metal rod (different block configurations are shown in Figure 2.1 and discussed elsewhere[3]). Varying the channel length and diameter after the site of laser vaporization changes the degree of clustering, mostly due to the change in interaction time and temperature. The cutaway source block has the vaporization site at the start of the supersonic expansion cone, resulting in fewer reactions and the coldest expansion. The offset source is the coldest source, allowing both the metal vapor and the gas to expand before mixing. The molecules move with uniform velocity through the skimmer to form a molecular beam and pass into a differentially-pumped mass spectrometer. The volume of gas that the pumps handle requires a large pumping speed. The pumps used for the cluster source chamber and the mass spectrometer vacuum chambers are VHS-10 (6600 L/s of He) and VHS-6 (3000 L/s) diffusion pumps, respectively.

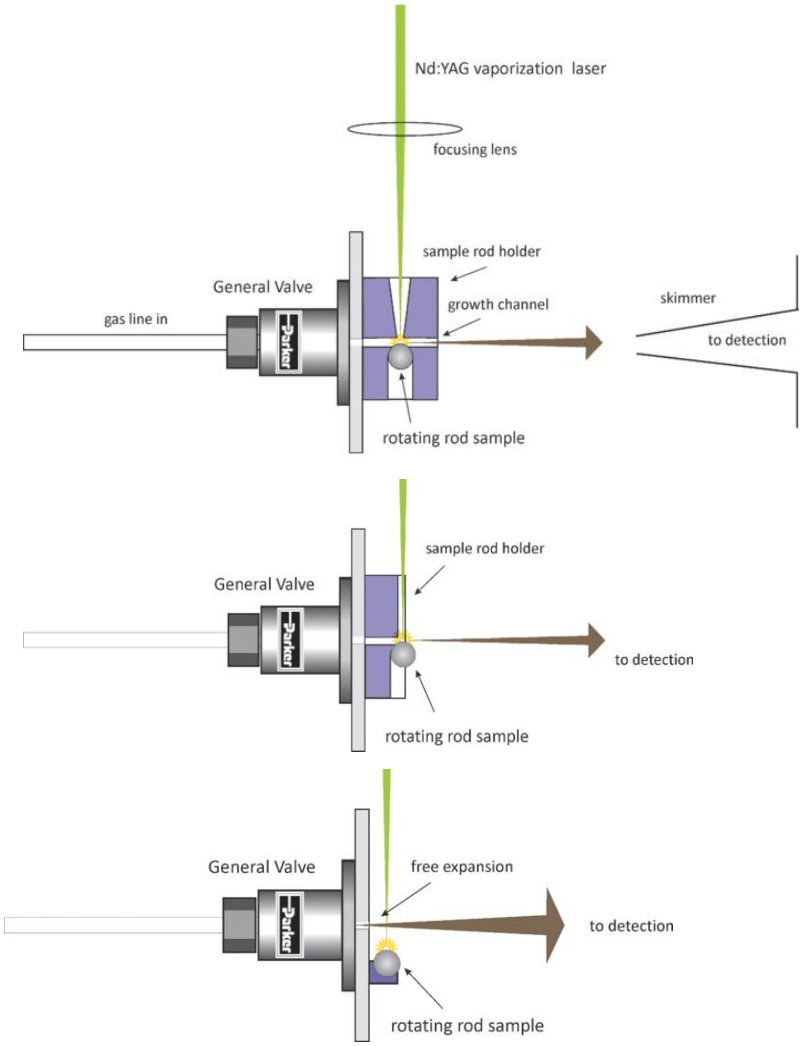

Figure 2.1. Commonly used source blocks in laser vaporization experiments. The standard block can have various channel diameters and lengths to promote cluster growth.

A Wiley-McLaren time-of-flight mass spectrometer is used for mass analysis, ion separation, and photodissociation spectroscopy.[4] A diagram of this instrument is shown in Figure 2.2. The molecular beam is sent through a skimmer into a second vacuum chamber, where Wiley-McLaren electrodes (a repeller plate and a draw-out grid) are pulsed to extract ions into the orthogonal flight tube. Deflection plates are used to adjust the horizontal trajectory of the ions into the flight tube. Biased electric rings are used as an ion lens to focus the ion beam to

counteract space-charge effects before the beam enters a field-free region of the flight tube. Ions extracted into the flight tube are given the same kinetic energy by the electric fields, so the ions are separated by flight velocity depending on mass, as described in Equation 2.1.

$$\text{Kinetic Energy} = \tfrac{1}{2} mv^2 \qquad \text{Eq. 2.1}$$

The ions then enter the reflectron, where they are slowed and then reaccelerated towards the detector. This serves to resolve ions of the same mass moving at different speeds and therefore improves resolution of the arrival time. Ions are detected with an electron multiplier tube detector (Hamamatsu Photonics R-595). Plotting the arrival time versus signal intensity and calibrating with known ion masses gives a mass spectrum. Ions can be deflected in the flight tube to select a mass size to be detected. The region of the flight tube after the reflectron is electrically isolated from the rest of the instrument and can be pulsed to accelerate ions further as they exit (a so-called post-accelerator), which increases the ion signal. The collected signal is amplified with a pre-amp and displayed on an oscilloscope. A typical mass spectrum of carbon clusters is shown in Figure 2.3, using a glassy carbon rod and helium backing gas.

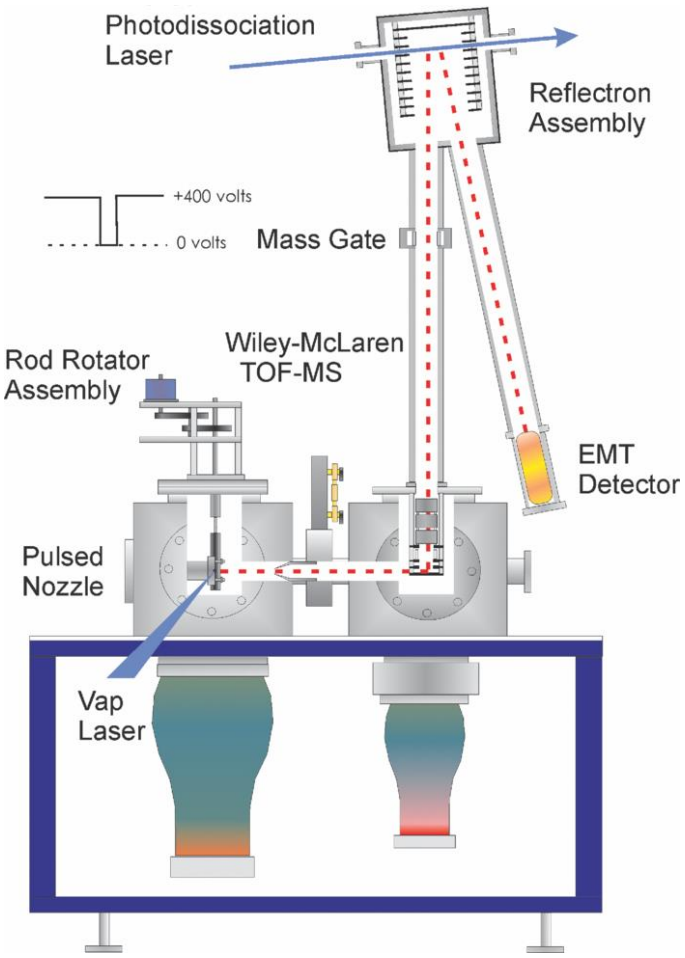

Figure 2.2. Illustration of the differentially-pumped reflectron time-of-flight mass spectrometer.

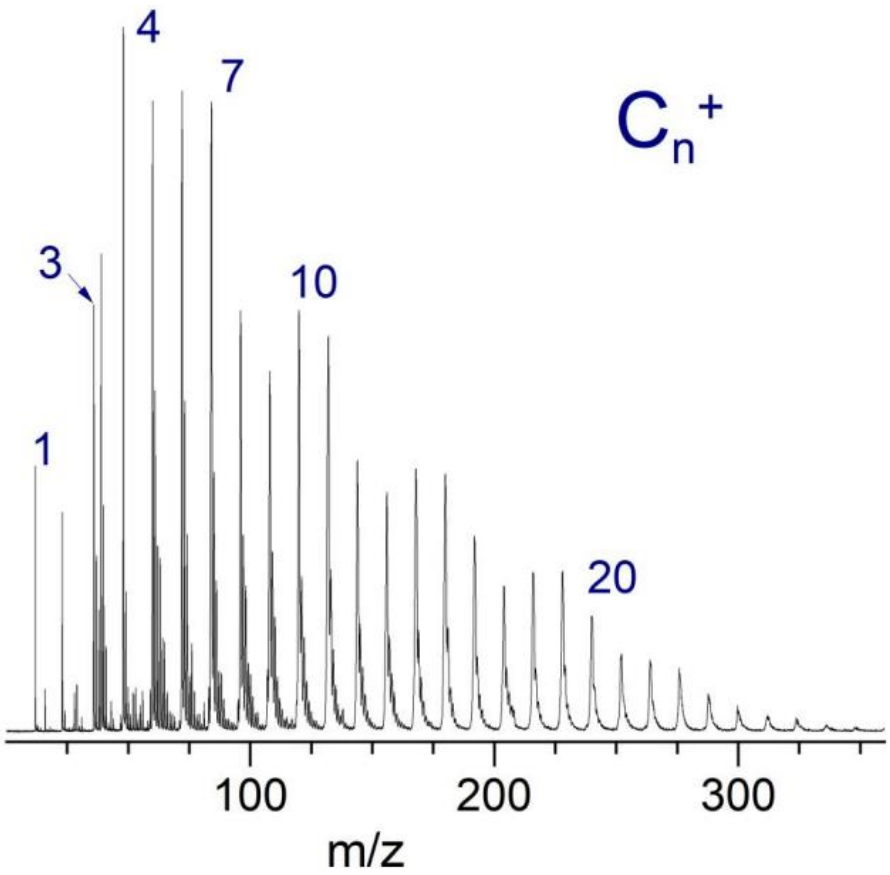

Figure 2.3. An example mass spectrum of carbon clusters collected using the described instrument.

As mentioned, a specified ion size can be isolated by deflecting other ions off the flight path before the reflectron. The turning point of the reflectron is an ideal region to induce photodissociation: ions are easier to illuminate with the pulsed photodissociation laser when they are slowed, and the dissociation products are reaccelerated in the reflectron field so as to arrive at the detector at different times. If an ion size is selected using the mass gate, the only signals detected are the selected ion and photodissociation products. The photodissociation process only occurs when the laser light is absorbed by the ion in question and when the photon energy is sufficient to overcome the binding energy of the ionic complex. The binding energy of the complex may limit what wavelength of light can be used for photodissociation, but the binding energy of aromatic ligands to transition metal ions usually falls in the visible light region. The

tunable photodissociation laser used is the Amplitude Laser Inc. Horizon II Optical Parametric Oscillator (OPO) system, which produces 192 – 2750 nm light (UV – near IR) with a 7 cm^{-1} linewidth. To prevent multiphoton absorption, the power is attenuated to 1 mJ/pulse, and the beam is unfocused. The intensity of the photodissociation product is plotted versus wavelength to create an action spectrum.

DATA ACQUISITION SOFTWARE

The photodissociation product yield is plotted against the OPO output wavelength to make an action spectrum, so data acquisition software was written to communicate with both the OPO control computer and the oscilloscope capturing the detector signal. Travis Jones created a LabVIEW program to scan a dye laser and acquire data from a scope (see his thesis[5]), which serves as the basis to communicate with the Horizon II OPO. Several changes were necessary: the code had to instead communicate with a separate computer controlling the OPO, and the scanning function needed to be modified to take discreet steps rather than sampling at time intervals and assuming the laser wavelength based on the scanning speed, but much of the framework remains the same. More information on this code can be found in the Appendix.

COMPUTATIONAL METHODS

To complement the photodissociation spectra collected, the electronic spectrum of each complex is predicted. Ideally, CCSD(T)/aug-cc-pVTZ would be used, as it is considered the golden standard level of theory. However, this level requires a considerable computational cost, and even though there are at times only 5 atoms involved, the number of electrons to consider for transition metals quickly makes this unfeasible for the complexes studied. These computations

are carried out using the Gaussian 16 package[6] using density functional theory (DFT). From previous work in the lab, B3LYP is a hybrid functional that has been shown to provide accurate vibrational and electronic data at a reasonable computational cost for the metal ion-ligand complexes of interest. In Chapter 3, B3LYP calculations of transition metals are tested against MN15L and M06L, which are functionals designed to better handle transition metals. The calculations shown in Chapters 3 and 4 are all made using a Def2-TZVP basis set. All calculations were carried out using an "ultrafine" integration grid, and the optimization threshold for energy and structure optimizations was set to "tight." The "stable=opt" keyword was used on all structures to check for electronic wavefunction stability. All electronic energies are corrected for zero-point vibrational energy. Depending on the system, the first 100 or 150 electronic transitions were calculated using TD-DFT.

REFERENCES

1. Fridman, A. *Plasma Chemistry*; Cambridge University Press: Cambridge, 2008.
2. Anisimov, S. I.; Bityurin, N. M.; Luk'yanchuk, B. S. Models for Laser Ablation. In *Photo-Excited Processes, Diagnostics and Applications: Fundamentals and Advanced Topics*; Peled, A., Ed.; Springer US: Boston, MA, 2003.
3. Duncan, M. A. Invited Review Article: Laser Vaporization Cluster Sources. *Rev. Sci. Instrum*. **2012**, *83*, 041101.
4. Wiley, W. C.; McLaren, I. H. Time-of-Flight Mass Spectrometer with Improved Resolution. *Rev. Sci. Instrum*. **1955**, *26*, 1150–1157.
5. T. M. Jones. M.S. thesis (University of Georgia, 2008).
6. Frisch, M. J.; Trucks, G. W.; Schlegel, H. B.; Scuseria, G. E.; Robb, M. A.; Cheeseman, J. R.; Scalmani, G.; Barone, V.; Petersson, G. A.; Nakatsuji, H.; Li, X.; Caricato, M.; Marenich, A. V.; Bloino, J.; Janesko, B. G.; Gomperts, R.; Mennucci, B.; Hratchian, H. P.; Ortiz, J. V.; Izmaylov, A. F.; Sonnenberg, J. L.; Williams-Young, D.; Ding, F.; Lipparini, F.; Egidi, F.; Goings, J.; Peng, B.; Petrone, A.; Henderson, T.; Ranasinghe, D.; Zakrzewski, V. G.; Gao, J.; Rega, N.; Zheng, G.; Liang, W.; Hada, M.; Ehara, M.; Toyota, K.; Fukuda, R.; Hasegawa, J.; Ishida, M.; Nakajima, T.; Honda, Y.; Kitao, O.; Nakai, H.; Vreven, T.; Throssell, K.; Montgomery, J. A., Jr.; Peralta, J. E.; Ogliaro, F.; Bearpark, M. J.; Heyd, J. J.; Brothers, E. N.; Kudin, K. N.; Staroverov, V. N.; Keith, T. A.; Kobayashi, R.; Normand, J.; Raghavachari, K.; Rendell, A. P.; Burant, J. C.; Iyengar, S. S.; Tomasi, J.; Cossi, M.; Millam, J. M.; Klene, M.; Adamo, C.; Cammi, R.; Ochterski, J. W.; Martin, R. L.; Morokuma, K.; Farkas, O.; Foresman, J. B.; Fox, D. J. Gaussian, Inc., Wallingford CT, 2016.

CHAPTER 3

METAL ION-LIGAND COMPLEX ELECTRONIC SPECTROSCOPY AND BOND DISSOCIATION THRESHOLDS

Covalent and non-covalent processes involving metals are found throughout chemistry, biology, and industry, including the Haber-Bosch process, the Fischer-Tropsch synthesis, and many biomolecules having a metal binding site, such as hemoglobin.[1-7] The coordination, bonding, and reactivity of transition metals hinges on their spin state. However, the relative energy of transition metal spin states can be difficult for theory to correctly predict, and for some, the number of electrons makes high-level theory too expensive to use. There has been much research into the interactions of transition metals and ligands in the gas phase to avoid solvent effects: mass spectrometry and computational chemistry provide information on the reactivity and thermochemistry of these metal ions with small hydrocarbons.[8-33] In some systems, the spectroscopy of metal ion-ligand complexes has been measured.[34-38] More recently, spectroscopy of transition metal ions coordinated to small hydrocarbons has been measured,[37-50] where the catalysis of benzene cyclization has been observed.[48-50] Metal ion-ligand complexes have been well-studied, but they still prove challenging for theory to correctly describe. Metal ions complexed with acetylene and benzene in the gas phase provide model systems against which to benchmark new theoretical models.

The bonding of transition metals to acetylene and benzene is known to form intriguing structures and provide some of the most basic organometallic systems.[51-58] It was observed early on that metal salts added to liquid benzene would react to change the color of the solution, leading to the discovery of covalent metal-benzene complexes.[59-64] The continued synthesis of

compounds such as ferrocene[65,66] and di-benzene chromium[67] would be the starting point for modern organometallic chemistry. Many traditional spectroscopy techniques were employed to understand the stability of these compounds.[68-77] In more recent years, mass spectrometry has been used to explore these same concepts in the gas phase. This is especially true for metal-benzene complexes but also includes ionic complexes and complexes with other ligands. Some of the most remarkable findings are the metal "multiple decker sandwich" clusters that metal-benzene complexes form, a structure of benzene-metal-benzene-metal… chain of varying length, keeping a stoichiometry of $[M_n(benzene)_{n+1}^+]$.[78-83] These sandwiches are most apparent for early transition metals, but they are also seen for several other metals. The bonding and electronic structure of these sandwiches have been well studied, and these complexes are now known to be very stable.[84-95]

Spectroscopy would fully describe the structural and electronic structure of these metal ion-ligand complexes, but because their density is so low, measurements have been limited to mass-selected photoelectron and photodissociation spectroscopy in the gas phase.[45] Anion photoelectron spectroscopy was used to determine the electron affinities and ionization potentials of these complexes,[96-99] with pulsed-field ionization-zero electron kinetic energy photoelectron spectroscopy later providing high enough resolution to observe vibronic transitions.[100-103] Further information about the structure of these organometallic complexes was probed using infrared photodissociation spectroscopy of the complex with a rare gas tag[45,104-106] and infrared resonance-enhanced multiphoton photodissociation.[45,107,108] These complexes represent model systems for larger, more complicated metal-arenes that can be unwieldy for computational chemistry to calculate. For this reason, high-level calculations (such as the "gold standard"

CCSD(T)) on these systems can take months. Transition metals in particular are challenging for theory, thus more gas phase measurements are needed for benchmarking.

Perhaps the most fundamental properties that can give insight into this organometallic bonding are the dissociation energies of these complexes. Collision-induced dissociation can be used to determine the bond dissociation energy of each complex. To do so, the complex is produced in a molecular beam, size-selected, and injected into a collision cell with an adjusted, known kinetic energy. Armentrout and colleagues have measured the bond dissociation energies of many organometallic complexes in this manner.[31,109-113] These experiments have been demonstrated to accurately determine an upper limit for the binding energy. However, this determination assumes that the ions only have one collision in the cell. Furthermore, the collisions occurring for large molecules with kinetic energy just slightly above the dissociation energy have a lower yield due to energy being randomly distributed over all internal vibrations, creating what is known as a kinetic shift. More information on this can be found in reference 113. These caveats are corrected for in each calculation, but these values should be tested against other methods. Another determination of an upper limit of the bond dissociation energy of a complex is the photodissociation threshold, the lowest photon energy at which photodissociation of a complex is detected. The photodissociation threshold serves as an upper limit to the binding energy, and it will only give a good determination for the bond dissociation energy when the species studied is cold, the complex absorbs continuously near that energy, and the dissociation process is single-photon. For many transition metal ion-benzene complexes, for example, the bond dissociation energy falls between 25 and 60 kcal/mol;[45] the threshold for these complexes would therefore lie in the visible or near-UV. Transition metals with low-lying excited spin states such as iron and chromium will absorb light throughout this region. This can be clearly

seen in Reference 114, where Brucat *et al.* measured the photodissociation of Fe_2^+. Photodissociation thresholds have been studied for some metal ion complexes, but without lasers whose wavelength can be tuned over a wide range, uncertainties were at around 5 nm.[115] There is scientific merit to remeasuring these values with less uncertainty.

These metal ion-ligand complexes are model systems for more complicated organometallics. Gas phase spectroscopy of these complexes provides information on their bonding, structure, and chemical interactions that are unperturbed by solvation effects. Computational methods have been developed to accurately describe the characteristics of these systems, but these methods may still underperform unspecialized functionals that are more commonly used, which will be explored in the experiments below. Therefore, more benchmarking is necessary for computational method development.

RESULTS AND DISCUSSION

Ag^+(toluene) and Ag^+(benzene)

Chapter 1 discusses the laser vaporization source and how it can be used to produce transition metal ion-ligand complexes in the gas phase, which was used for all complexes discussed in this chapter. Figure 3.1 shows a mass spectrum of $Ag^+(toluene)_n$ complexes produced by laser vaporization of a silver rod in an expansion of argon; liquid toluene was added to the gas lines, where the vapor pressure of toluene is sufficient for complexation with the silver.

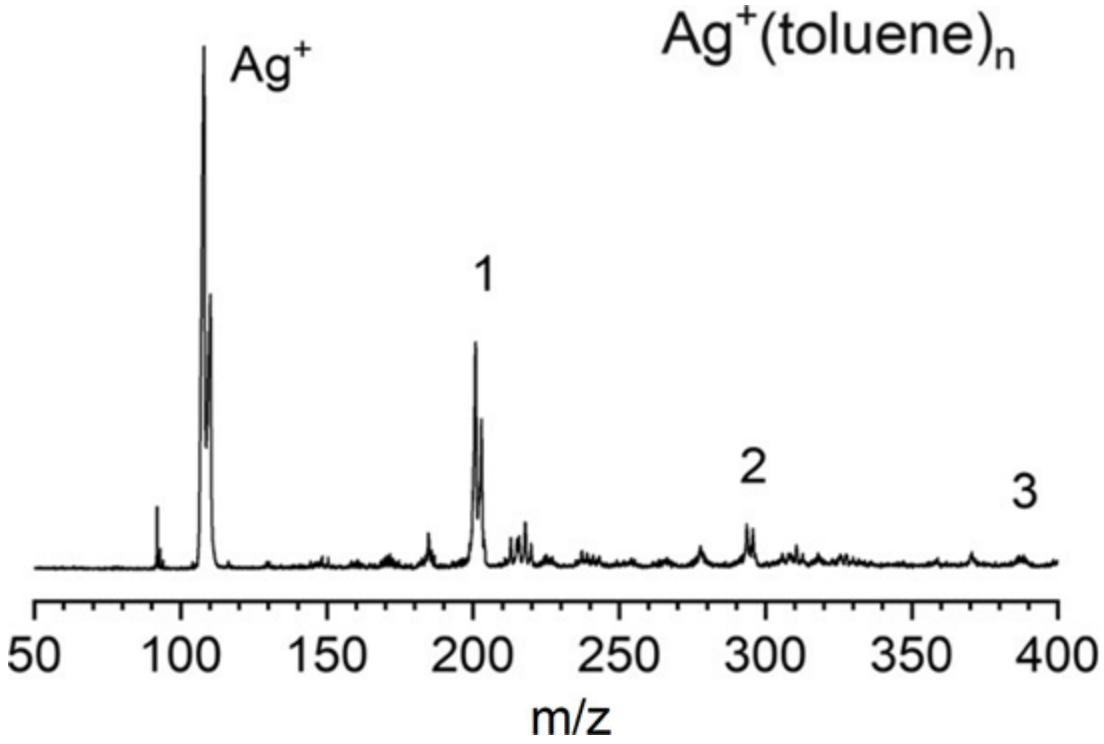

Figure 3.1. The mass spectrum of a silver rod in a toluene-seeded expansion of argon.

The photodissociation apparatus is discussed in more detail in Chapter 2. An ion size can be isolated by deflecting the other ions in the flight tube, ensuring that only one peak in the mass spectrum remains. The mass-selected ions are then illuminated with the photodissociation laser, and any photodissociation products are detected at a different arrival time. Figure 3.2 shows the photodissociation mass spectrum of Ag^+(toluene) at 355 nm. The photodissociation product observed is the toluene cation. Silver cation is expected to be the photodissociation product, as silver has an ionization energy of 7.58 eV while toluene has an ionization energy of 8.83 eV. This kind of photodissociation is therefore a charge-transfer process, which has been seen previously.[45] The silver cation photodissociation product was not observed in any spectral region in this experiment.

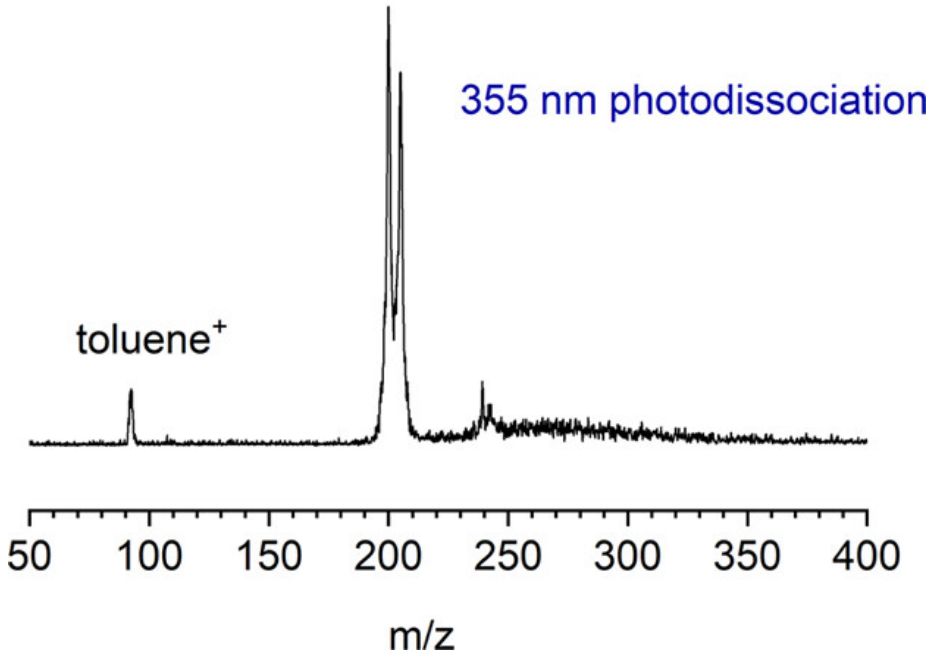

Figure 3.2. Photodissociation mass spectrum of the mass-selected Ag^+(toluene) ion at 355 nm, which produces the toluene cation as the only photofragment. Peaks containing silver are doubled from the two naturally occurring isotopes (m/z = 107/109).

The photodissociation product yield varies with the wavelength of the laser, thereby creating a photodissociation spectrum. Figure 3.3 presents the charge transfer photodissociation spectrum of Ag^+(toluene). The bottom two traces are spectra predicted by TD-DFT without a scaling factor. Two isomers were predicted; the silver is over a C – C bond in both structures, but the positions of the metal ion differ with respect to the methyl group. Although most transition metal ions complex with aromatic rings in the sixfold symmetric position, silver is known from previous work to form this kind of asymmetric structure.[116,117] Isomer 1 was predicted to be more stable than isomer 2 by 0.83 kcal/mol, though it is not clear that this difference is significant. The spectrum of Ag^+(toluene) has a broad band near 30,800 cm^{-1} with a reproducible dip near the middle, with smaller, broad bands deeper in the UV at 38,000 and 44,400 cm^{-1}.

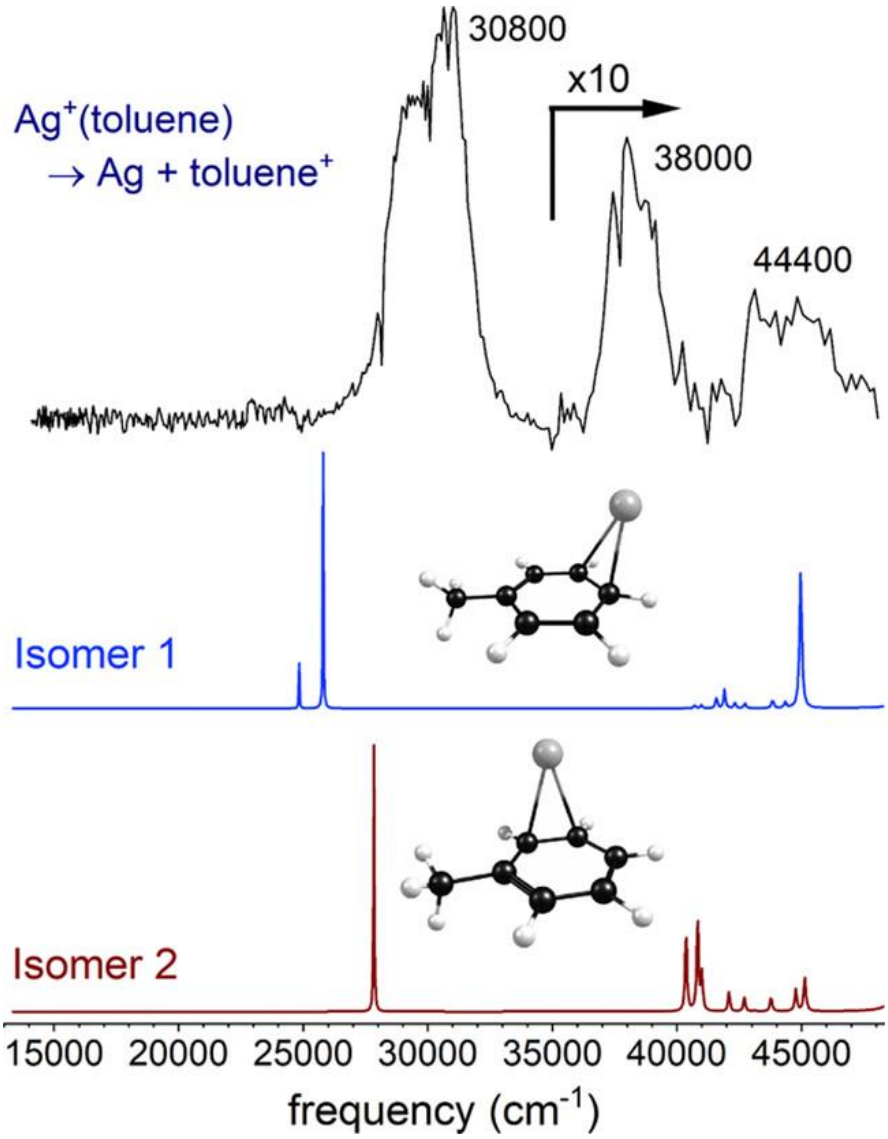

Figure 3.3. Photodissociation spectrum measured for Ag^+(toluene) → Ag + $toluene^+$.

Figure 3.4 shows a potential energy diagram for Ag^+(toluene). The ground state of the complex has the charge on the silver due to its lower ionization energy. This is confirmed in a collision-induced dissociation experiment producing silver cation, where the dissociation happens on the ground electronic state potential energy surface.[118] The silver cation has a $4d^{10}$ (^1S) electron configuration. The first excited state of the silver cation occurs at 39,168 cm^{-1} and is shown as transition (a). The first excited state of toluene occurs at 37,580 and is labeled transition (b). There are two excitations considered for the charge transfer excited state

whereupon dissociation occurs. The first is the first excited state of *neutral* silver, occurring at 29,552 cm^{-1} for the $^2S \rightarrow {}^2P$ transition and labeled (c). Finally, there is the first excited state of the toluene cation occurring at 17,700 cm^{-1} and labeled (d).[119]

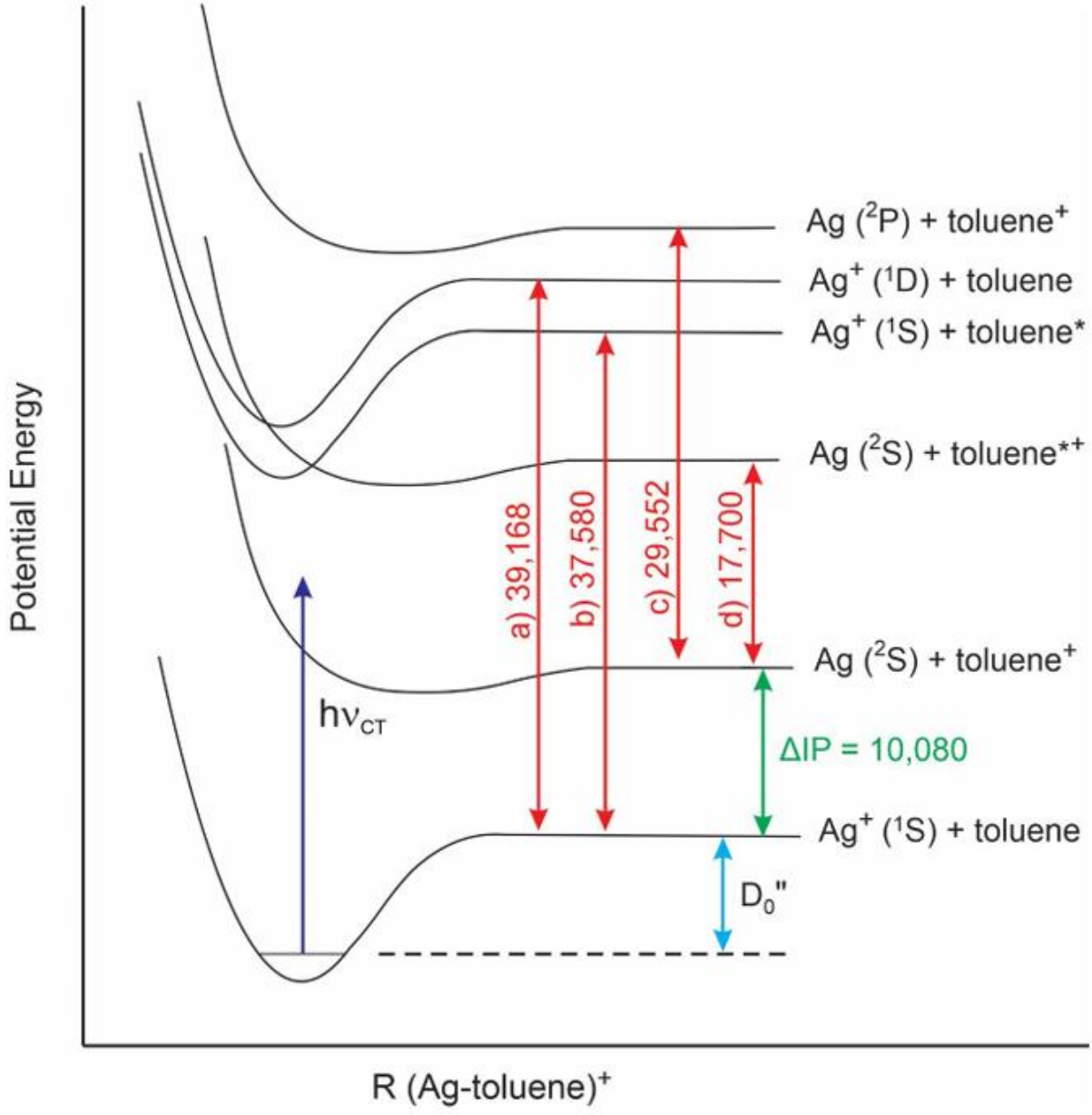

Figure 3.4. Potential energy diagram for Ag^+(toluene).

Figure 3.5 presents the mass spectrum for Ag^+(benzene), which was detected in much the same way described for Ag^+(toluene).

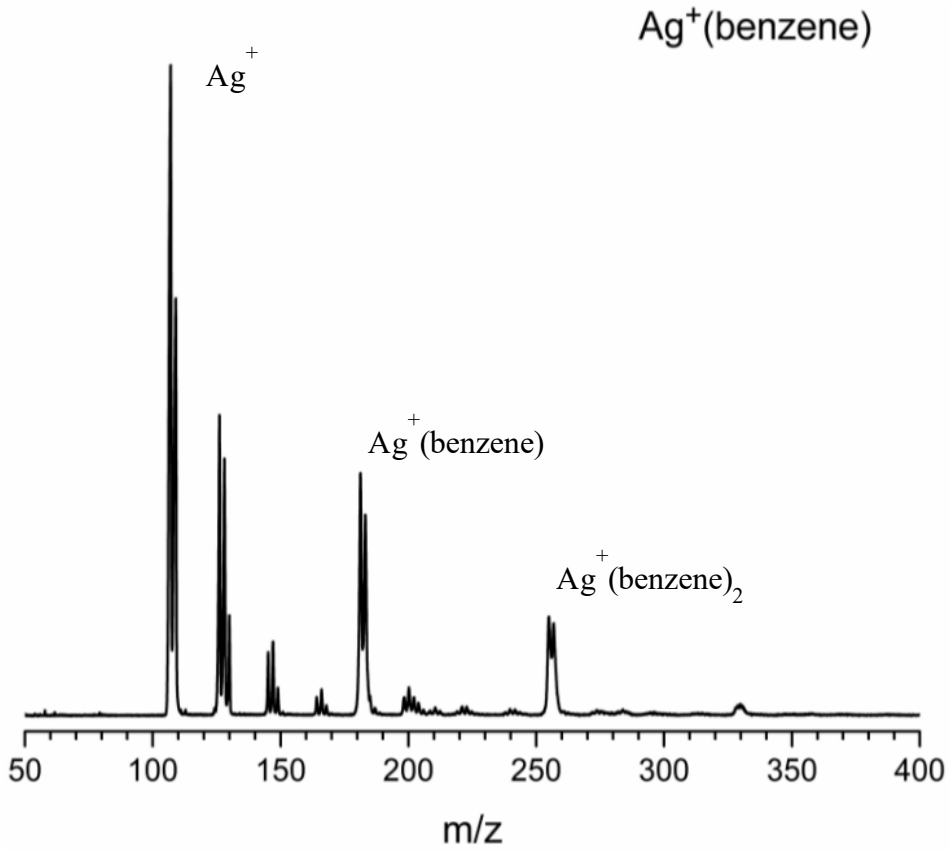

Figure 3.5. Mass spectrum of Ag^+(benzene) clusters.

Figure 3.6 shows the photodissociation spectrum for the Ag^+(benzene) complex. The spectrum has a broad peak at 31,000 cm^{-1} and two smaller bands at 38,700 and 45,300 cm^{-1}, which are all at frequencies similar to those in the Ag^+(toluene) spectrum.

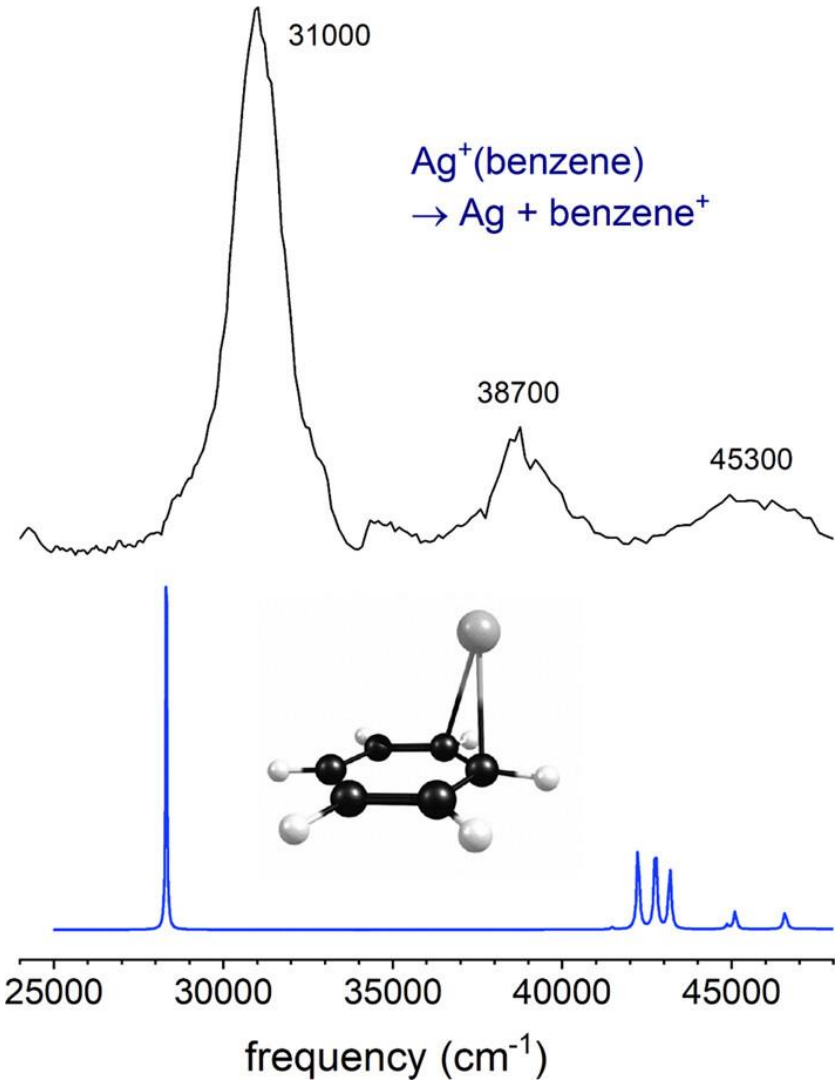

Figure 3.6. Photodissociation spectrum of Ag^+(benzene) → Ag + $benzene^+$ (top) and the spectrum predicted by TD-DFT (bottom).

It is known that TD-DFT is not reliably quantitative for frequencies of predicted excitations, so usually a scaling factor is used to better match experimental spectra.[120] However, the predicted spectra here match the experiment reasonably well without scaling. The calculated spectra in Figures 3.3 and 3.5 predict the observed photodissociation spectra reasonably well, especially for the lowest energy transition measured. It should be noted that TD-DFT does not predict vibrational structure for electronic transitions nor Franck–Condon factors. The intense bands predicted for both isomers of Ag^+(toluene) near 26,000 cm^{-1} and Ag^+(benzene) near

28,000 cm^{-1} both correspond to charge transfer transitions, from Ag^+ to the ligand. The higher-energy transitions differ in nature between the isomers. The transition at 44,966 cm^{-1} predicted for isomer 1 involves a π(toluene) → π(toluene) transition with little interaction from the electron orbitals of the silver. In contrast, the three transitions predicted between 40,000 and 41,000 cm^{-1} for isomer 2 involve *d* (Ag^+) → *s* (Ag^+) excitations. Similarly, the three transitions predicted for Ag^+(benzene) near 43,000 cm^{-1} are also *d* (Ag^+) → *s* (Ag^+) excitations, though these excited states have increased electron density on the benzene. These transitions are shown in Figure 3.7.

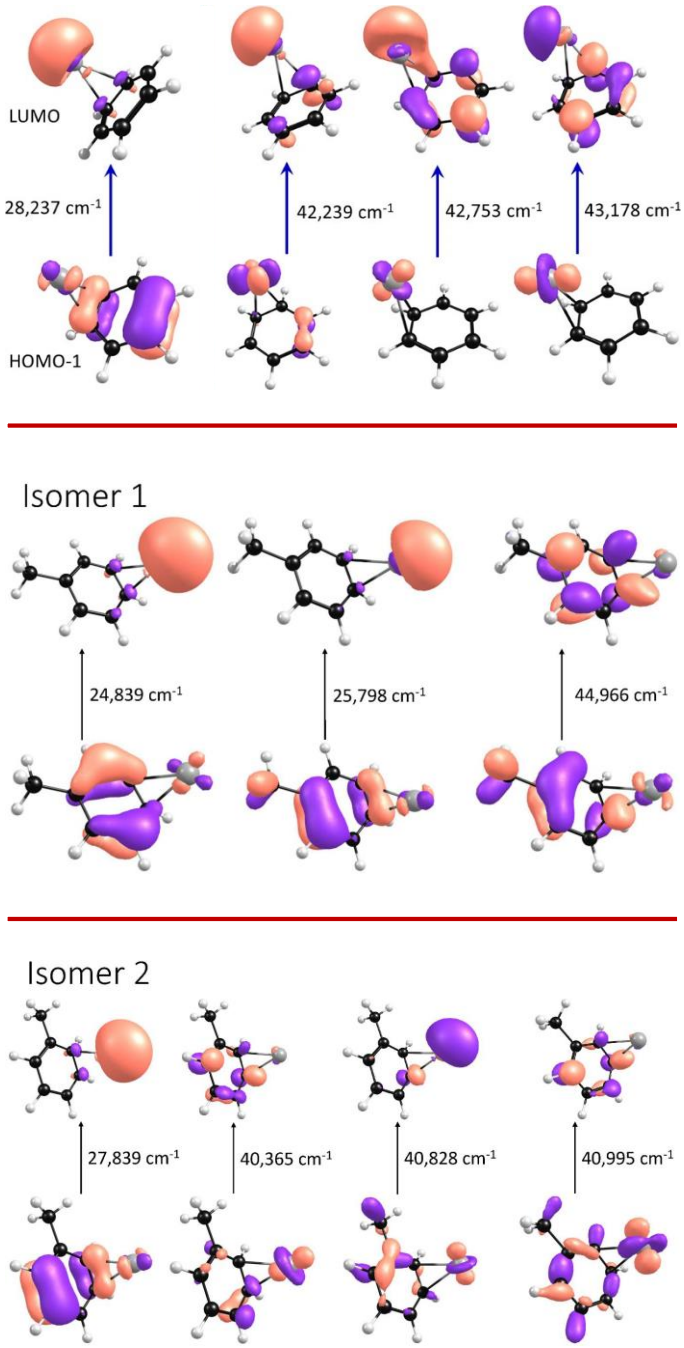

Figure 3.7. Molecular orbitals involved with each excited state transition for Ag^+(benzene) (top) and Ag^+(toluene) isomers 1 (middle) and 2 (bottom), calculated using TD-DFT (B3LYP/def2-TZVP).

The expansion used to create the ions in this study also produced ions of the complex with weakly-bound argon (e.g., Ag^+(toluene)Ar). Figure 3.8 shows the effect of an argon tag on the photodissociation spectrum of Ag^+(toluene) and predicted spectra for isomers 1 and 2 when

they are tagged with argon. The signal of the tagged complex is worse than that without the tag due to the lower ion signal in the mass spectrum. Theory for this complex and that of Ag^+(benzene)Ar predict that the argon attaches to the silver opposite to the ligand. The argon tag has a large effect on the spectrum for Ag^+(toluene). Firstly, the lowest-energy peak is shifted up in energy by about 6,000 cm^{-1}, to possibly overlap with the peak already present. Theory correctly predicts this shift. This would be consistent with a stronger solvation effect on the ground state, where the charge is localized on the silver, than the excited state, where the charge is delocalized on the toluene.

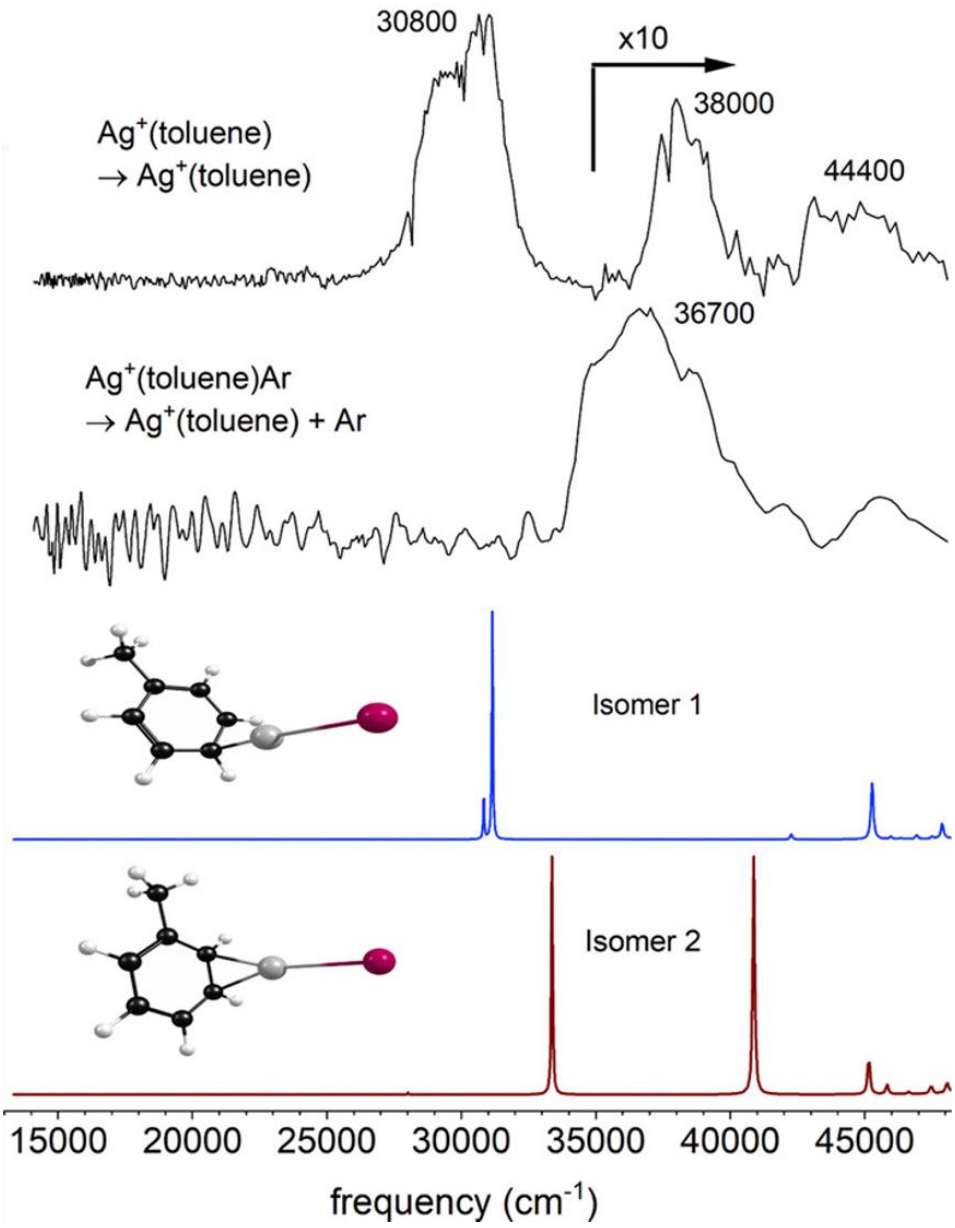

Figure 3.8. Photodissociation spectra of bare Ag^+(toluene) compared to Ag^+(toluene)Ar (top) and the TD-DFT predicted spectra of isomers 1 and 2 when tagged with argon (bottom). The photodissociation spectrum of the tagged complex measures the appearance of the Ag^+(toluene) ion.

Figure 3.9 shows the same argon tagging comparison with Ag^+(benzene)Ar. Similar to the results for Ag^+(toluene)Ar, theory predicts a shift of the main peak to higher energy, but the observed peak is instead shifted lower by about 7,000 cm^{-1}. The band observed is also narrower. Furthermore, neither higher-energy bands (in the untagged or predicted spectrum) are observed.

Interestingly, the photodissociation channel measured is the appearance of Ag^+, fully dissociated from the benzene and the argon tag. The tagging of these complexes with argon significantly affects their dissociation process. It is not clear how this solvation differs between the toluene and benzene ligands from the spectra alone. It is clear that the argon "tag" is not inert.

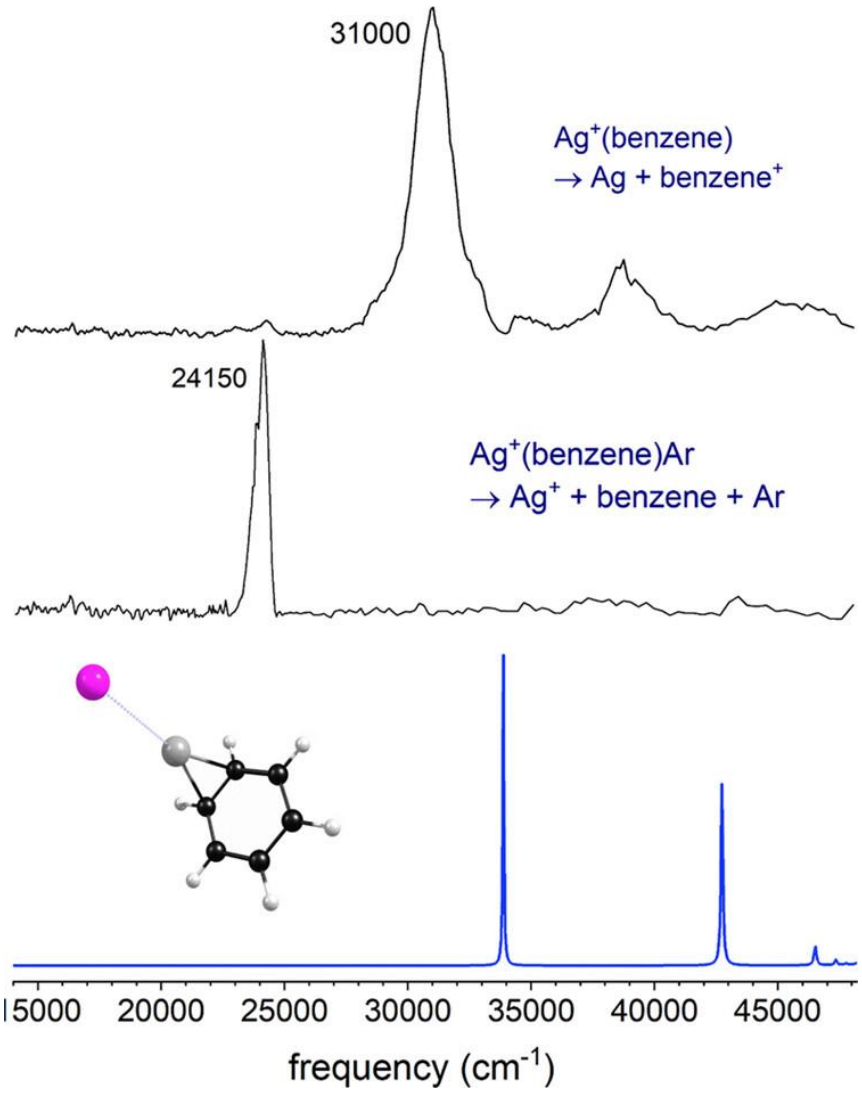

Figure 3.9. The photodissociation spectra of Ag^+(benzene) and Ag^+(benzene)Ar (top). The absorption spectrum for Ag^+(benzene)Ar was predicted using TD-DFT.

Mg^+(benzene)

Mg^+(benzene) was investigated to further understand the charger transfer in a metal ion-ligand system. Figure 3.10 shows the mass spectrum collected for Mg^+(benzene), and Figure 3.11 shows the difference mass spectrum for Mg^+(benzene) photodissociation.

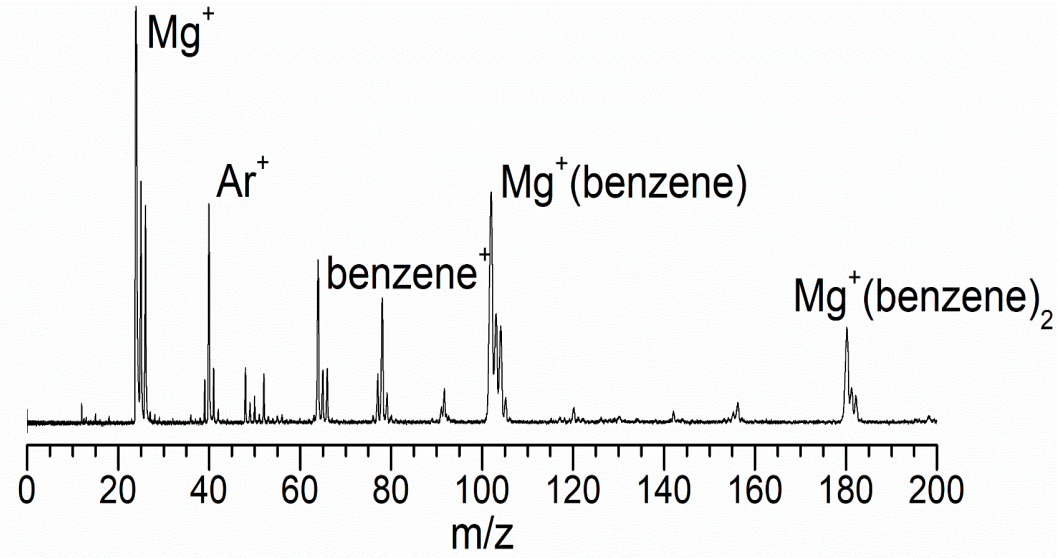

Figure 3.10 Mass spectrum of laser ablation of a magnesium rod in an expansion of benzene-seeded argon. Peaks for argon-tagged Mg^+ and $benzene^+$ are also present.

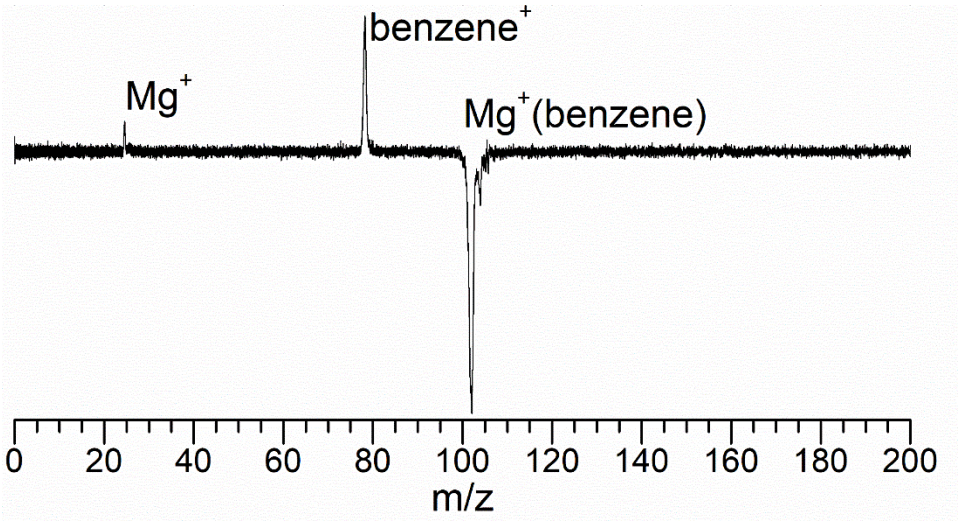

Figure 3.11. Photodissociation difference mass spectrum of Mg^+(benzene), where the mass spectrum with the photodissociation laser off is subtracted from the mass spectrum with the photodissociation laser on.

The photodissociation spectra of Mg^+(benzene) on both the Mg^+ mass channel and the $benzene^+$ channel are shown in Figure 3.12. Intriguingly, the spectra are very similar, with two large peaks at 330 and 240 nm. The predicted transitions are labeled on the figure and agree well with detected photodissociation peaks. The laser power is inconsistent through 310 – 292 nm

where the photodissociation laser changes which frequencies of the YAG are mixed. Unfortunately, while it looks as if a band is detected here, its entire profile was not measured. The ionization energy of a magnesium atom (7.65 eV) is lower than that of a benzene molecule (9.24 eV), so the charge is expected to be located on the magnesium. The transition predicted around 280 nm corresponds to a charge transfer electronic excitation. Interestingly, the benzene cation photodissociation product is still detected below this energy. The energy imparted by the photon is less than the energy necessary for the charge-transfer excitation. The atomic transitions of Mg^+ are well studied and known to be very intense, more so than the sodium D line.[121] Studies of the spectroscopy of Mg^+X (X = Ne, Ar, Kr, Xe, N_2, CO_2, H_2O, D_2O, C_2H_2) complexes also observe very strong electronic transitions that are located on Mg^+.[122-127] It is likely that the complex is absorbing a second photon and then undergoing excited state curve crossing in order to transfer the charge to the benzene and then dissociate. The strength of the Mg^+ atomic transitions would also explain the larger intensities of the transitions that are assigned to excitations located on Mg^+.

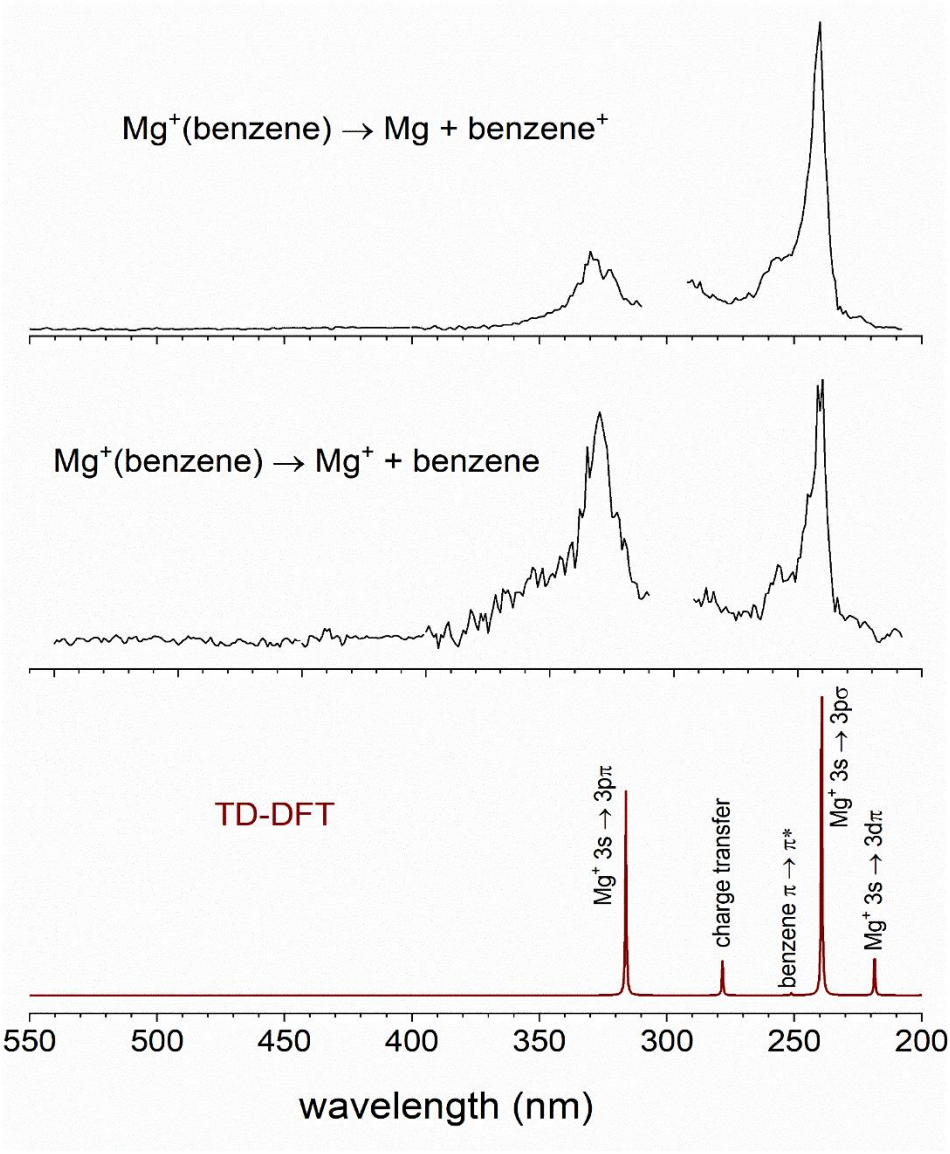

Figure 3.12. Photodissociation spectra of Mg^+(benzene) on the Mg^+ and benzene$^+$ mass channels (top) compared to the electronic spectrum predicted by TD-DFT/B3LYP/Def2-QZVP.

Fe^+(benzene) and Fe^+(benzene)$_2$

Figure 3.13 presents the mass spectrum collected for $Fe^+(benzene)_n$ using an iron rod and benzene-seeded argon. Complexes up to n = 5 are detected. Figure 3.14 shows the photodissociation mass spectrum of Fe^+(benzene) at 266 nm, where both the Fe^+ and the benzene$^+$ photodissociation products are seen, though the Fe^+ cation appears with more intensity.

Figure 3.15 shows the photodissociation mass spectrum for $Fe^+(benzene)_2$ at 260 nm, where $Fe^+(benzene)$ and a small amount of Fe^+ are observed.

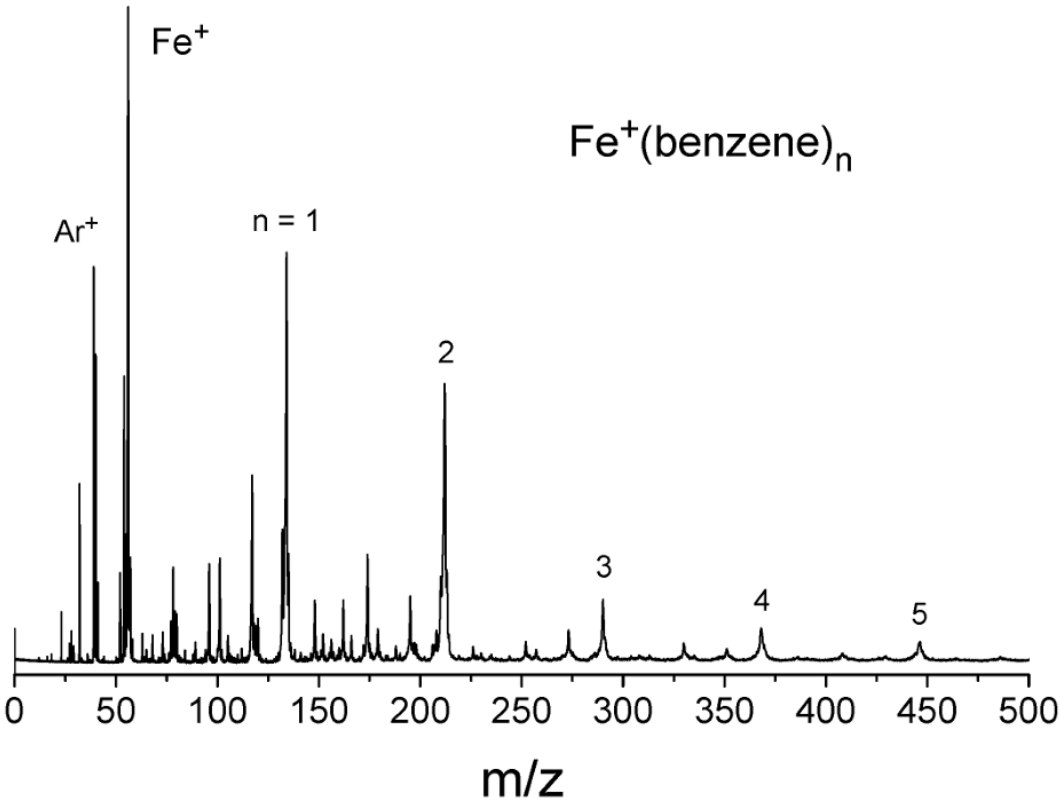

Figure 3.13. A mass spectrum of laser vaporization of an iron rod with a benzene-seeded expansion of argon.

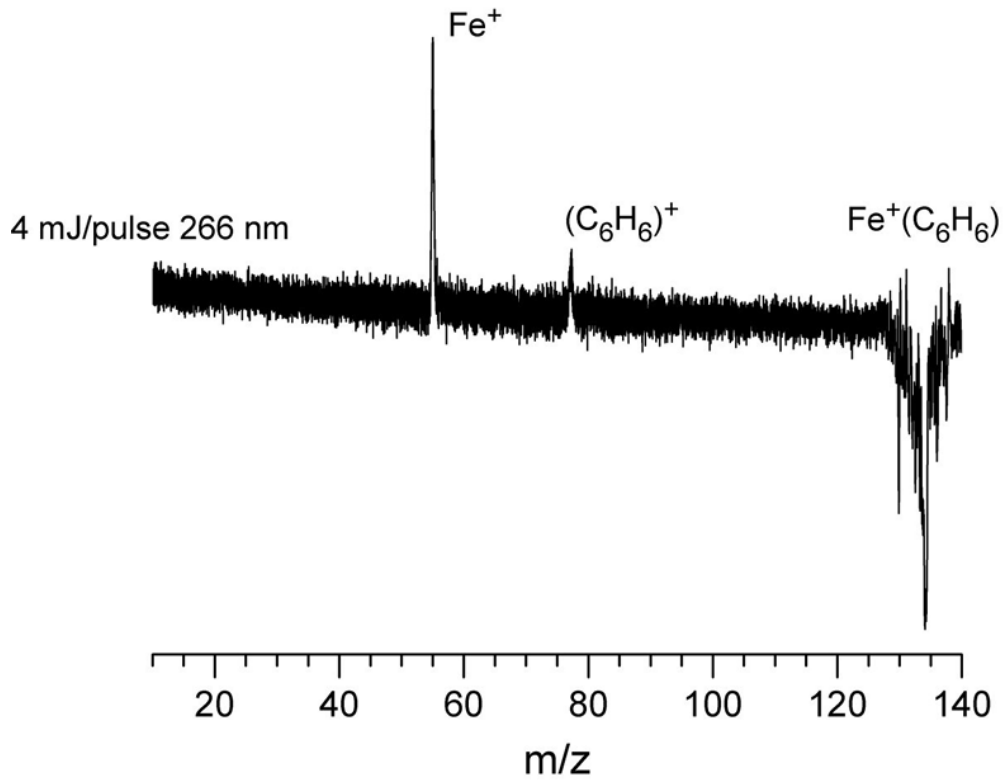

Figure 3.14. Difference mass spectrum of the photodissociation of Fe^+(benzene) at 266 nm, which produces both the Fe^+ and benzene$^+$ photofragments.

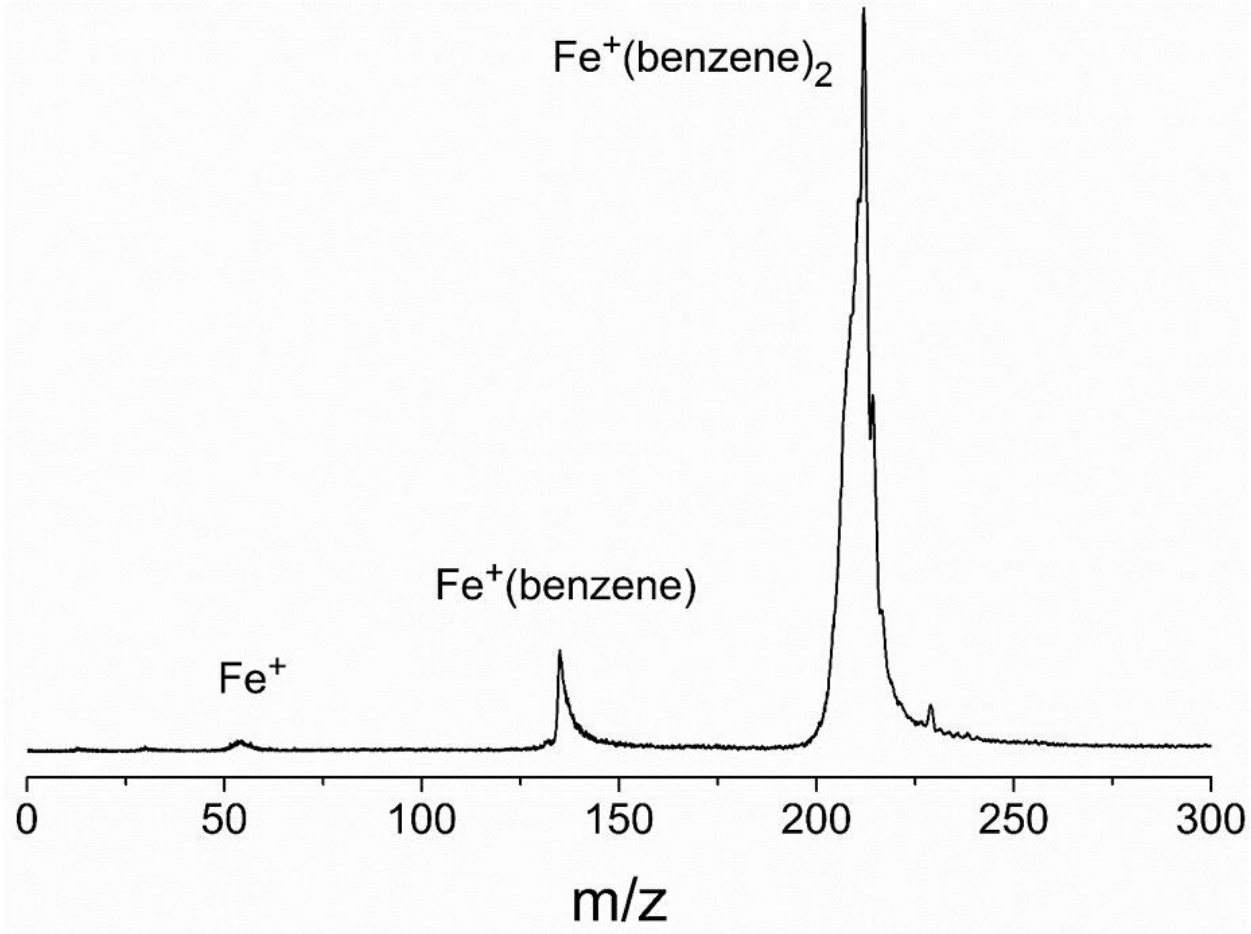

Figure 3.15. Photodissociation mass spectrum of $Fe^+(benzene)_2$ which produces primarily the Fe^+(benzene) photofragment. The photodissociation laser used 2 mJ/pulse at 260 nm.

Transition metals with partially filled *d* orbitals have multiple spin states and electronic states. These transition metals have a large density of electronic excitations that occur close in energy. An apt example is Fe^+.[121] This generally makes for uninformative electronic spectra. An example of this is shown in Figure 3.16, the photodissociation spectrum of Fe^+(benzene), along with spectra predicted using TD-DFT for spin states with multiplicities $m = 2,4,6$. The large dips in photodissociation signal at 400, 292, and 234 nm come from the instability of the photodissociation laser output. As there is no discernable structure to the spectrum, no assignment can be made by comparing to theory. However, this continuum can be exploited in photodissociation spectroscopy: the photon adding energy to the complex needs to overcome the

bond dissociation energy; ergo, the threshold at which the complex begins to photodissociate is an upper limit to the bond dissociation energy. Figure 3.17 provides a closer look at the visible region of the photodissociation spectra of both Fe^+(benzene) and Fe^+(benzene)$_2$ complexes.

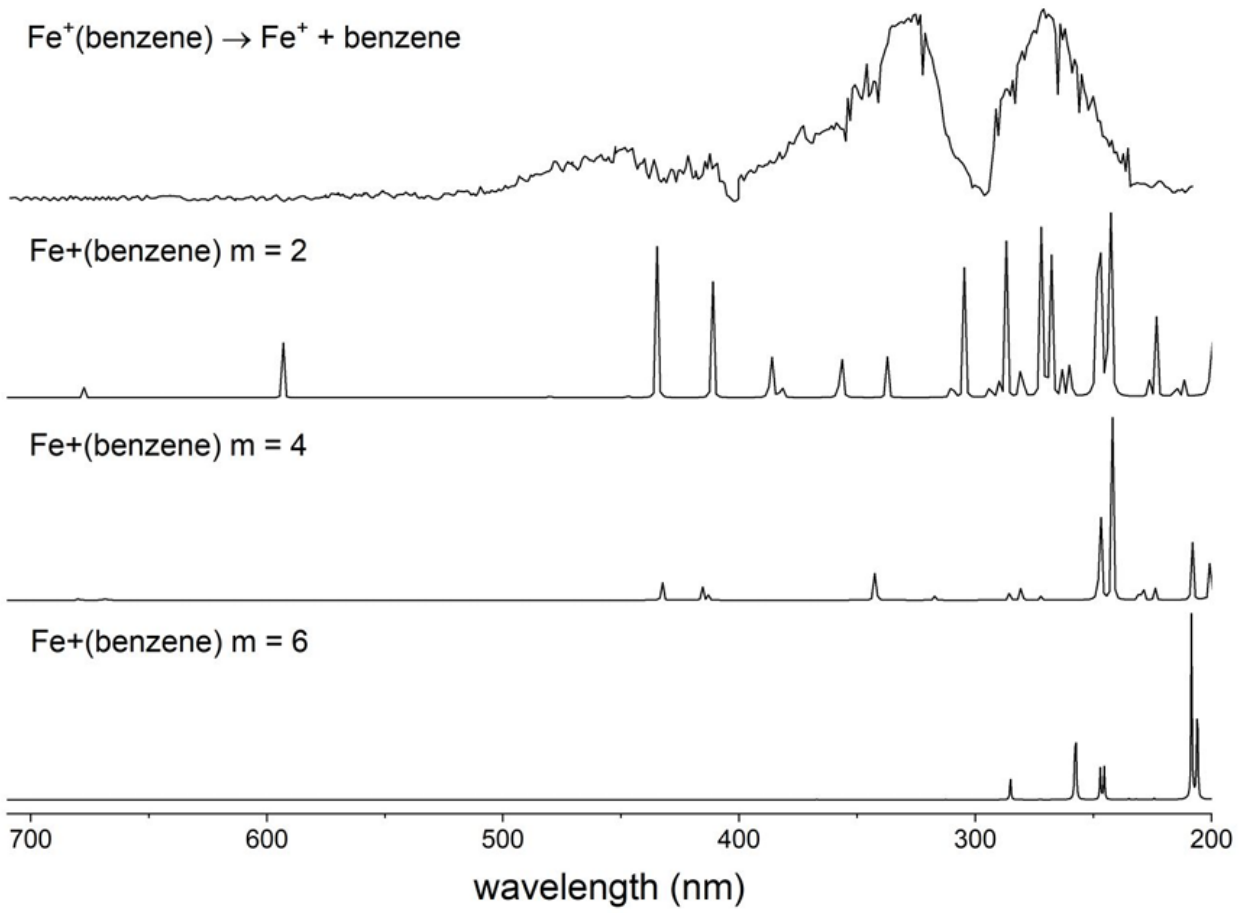

Figure 3.16. Measured photodissociation spectrum of Fe^+(benzene) → Fe^+ + benzene. The lower traces show the spectra predicted by TD-DFT for spin states of m = 2,4,6. While there is a difference in photodissociation intensity throughout the spectrum, when the photon energy overcomes the BDE threshold, the photodissociation signal becomes continuous.

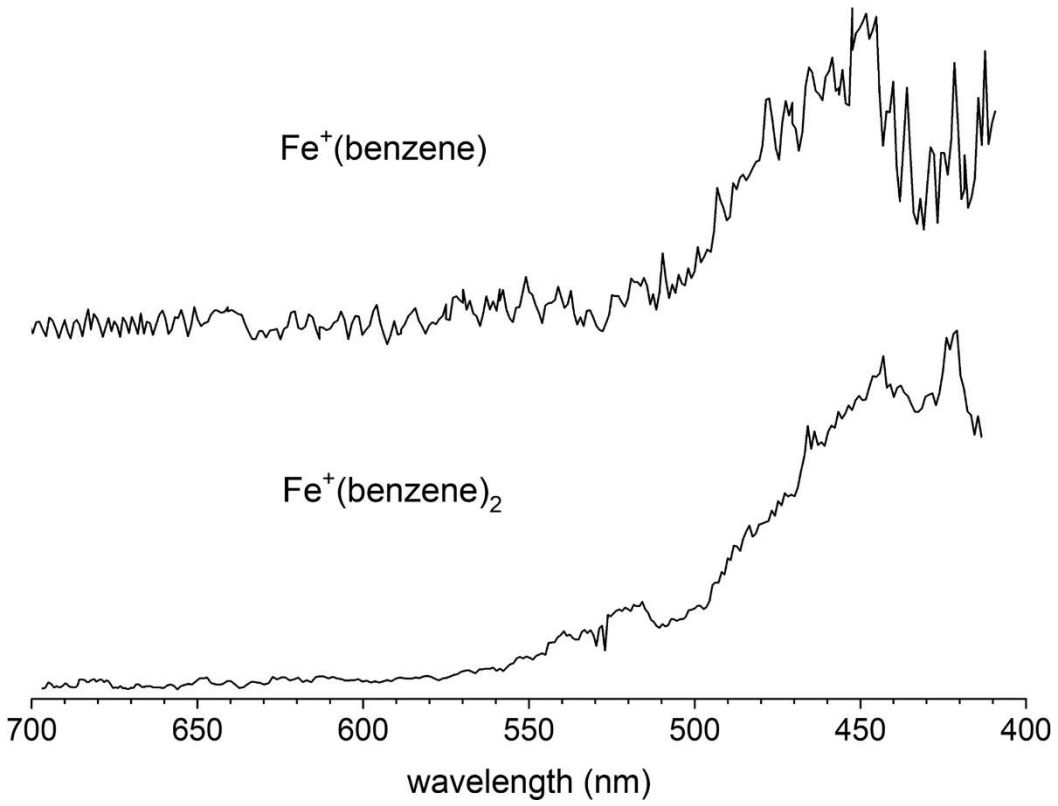

Figure 3.17. Photodissociation spectra in the visible wavelength region of Fe^+(benzene) (top trace) and Fe^+(benzene)$_2$ (bottom), measured in the Fe^+ and Fe^+(benzene) fragment ion channels, respectively. The photodissociation laser was scanned in 1 nm steps.

Figure 3.18 presents the same spectra of Fe^+(benzene) and Fe^+(benzene)$_2$ with a smaller photodissociation laser step size. The peak seen near 532 is where the laser has difficulty separating the fundamental harmonic frequency of the Nd:YAG laser from the output of the OPO, and the nearby dips are where the separation prism of the OPO overcompensates. A closer look allows the threshold to be determined to within 2 nm. The threshold wavelengths correspond to the upper limits of the dissociation energies for Fe^+(benzene) and Fe^+(benzene)$_2$ of 53.7 ± 0.2 and 48.4 ± 0.2 kcal/mol, respectively. The error limits are determined by the noise level in the spectrum near the threshold.

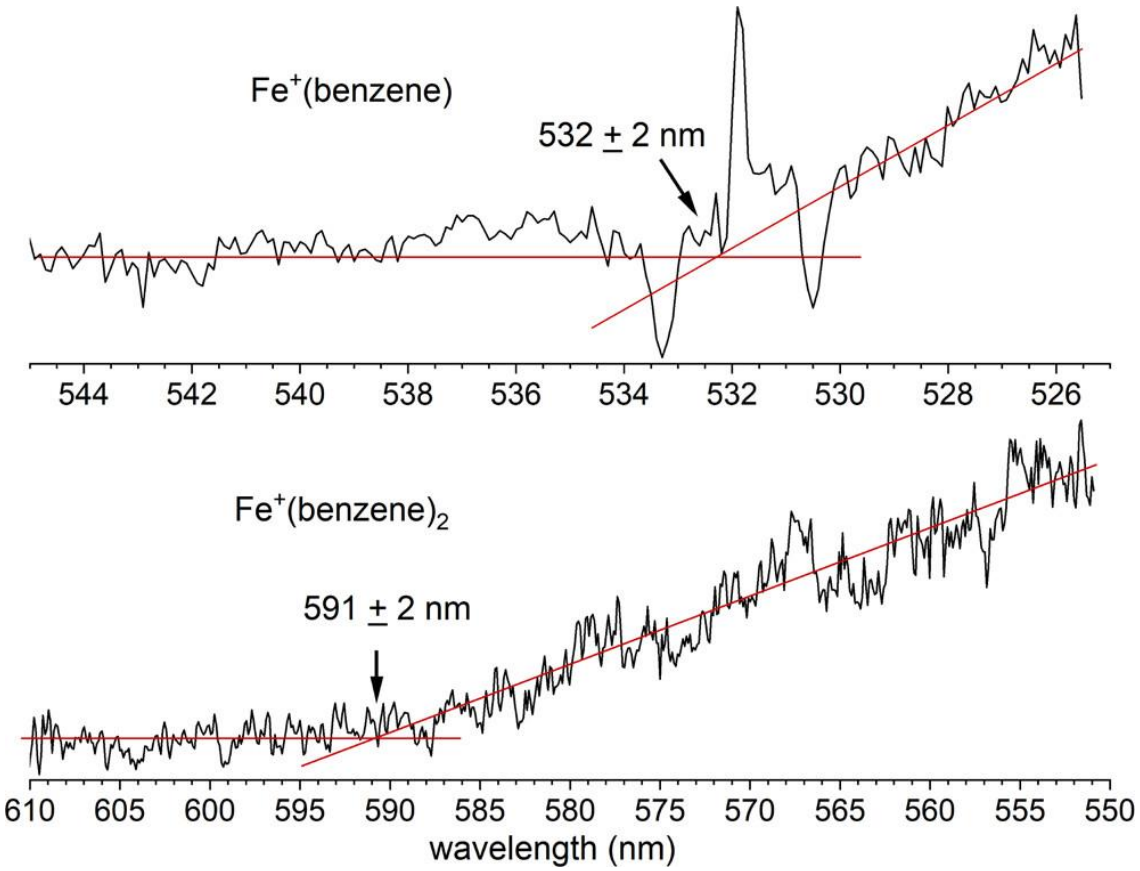

Figure 3.18. Photodissociation spectra of Fe^+(benzene) (top trace) and $Fe^+(benzene)_2$ (bottom) in the respective threshold regions. The photodissociation laser was scanned with a 0.1 nm step size.

Importantly, the ground state of Fe^+(benzene) was predicted to be $^4A_1$; an optical transition for the ground state of this complex must therefore excite into a quartet state. A schematic of the energy levels for this system is shown in Figure 3.19. The dissociation of the Fe^+(benzene) complex occurs after the excitation into a quartet state, so the upper limit for the binding energy determined by the photodissociation threshold is for the dissociation of a metastable Fe^+ in the ^4F state, not the ^6D ground state. To obtain the adiabatic dissociation energy, the energy difference of the ^6D and ^4F atomic electronic states (1873 cm^{-1}) must be accounted for.[121] After this correction, the upper limit of the dissociation energy of Fe^+(benzene) is 48.4 $\pm$ 0.2 kcal/mol. The ground state, excited state, and dissociative state for the

$Fe^+(benzene)_2$ complex are all quartets, so no correction needs to be considered, and the upper limit of the bond dissociation energy remains 48.4 $\pm$ 0.2 kcal/mol.

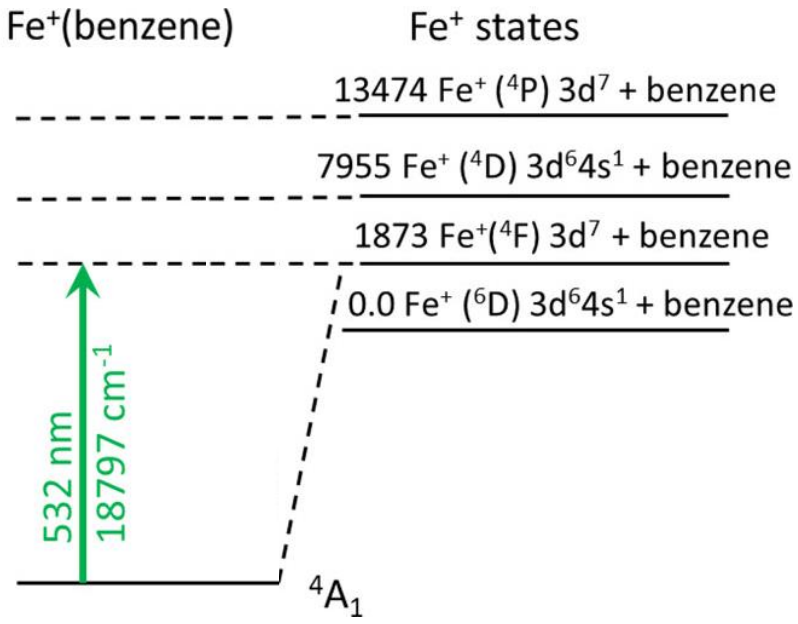

Figure 3.19. Energy level diagram for the Fe^+(benzene) complex as related to the excitations of atomic Fe. The green arrow represents the dissociation threshold measured with the tunable laser.

The bond dissociation energies determined via photodissociation threshold agree quite well with previous determinations by collision-induced dissociation, falling inside the error bars.[109] Table 3.1 provides the thermochemistry of the ions and complexes involved in this study, calculated with multiple TD-DFT methods at the Def2-TZVP level. Theory predicts the *m = 4* spin state to be the most stable for Fe^+, Fe^+(benzene), and $Fe^+(benzene)_2$. The bond dissociation energy of Fe^+(benzene) calculated by B3LYP agrees with the experimental value determined above. However, the value calculated for the dibenzene complex by all methods is significantly different than those determined by photodissociation threshold and collision-induced dissociation.[109]

Table 3.1. Zero-point corrected relative energies (in Hartrees/particle) for Fe^+, Fe^+ (benzene), and $Fe^+(benzene)_2$, as well as dissociation energies (in kcal/mol) for $Fe^+(benzene) \rightarrow Fe^+ +$ benzene and $Fe^+(benzene)_2 \rightarrow Fe^+(benzene) +$ benzene. The functional B3LYP is commonly used in the Duncan lab. M06-L and MN15-L are functionals that are specially designed for use on transition metal systems. *m = 2s + 1* denotes multiplicity. The experimentally determined upper limit for the dissociation energy of both the monobenzene and dibenzene complexes were found to be the same value.

Relative energies	**B3LYP**	**M06-L**	**MN15-L**
Benzene	– 232.237193	–232.193605	–232.022192
Fe^+ (*m* = 2)	–1263.369688	–1263.283754	–1263.228030
Fe^+ (*m* = 4)	–1263.411346	–1263.323876	–1263.304679
Fe^+ (*m* = 6)	–1263.404095	–1263.310728	–1263.311894
Fe^+(benzene) (*m* = 2)	–1495.702108	–1495.604750	–1495.394283
Fe^+(benzene) (*m* = 4)	–1495.735843	–1495.628604	–1495.443364
Fe^+(benzene) (*m* = 6)	–1495.703477	–1495.587757	–1495.422972
$Fe^+(benzene)_2$ (*m* = 2)	–1728.010477	–1727.898373	–1727.534614
$Fe^+(benzene)_2$ (*m* = 4)	–1728.023016	–1727.894086	–1727.550259
$Fe^+(benzene)_2$ (*m* = 6)	–1727.956849	–1727.820005	–1727.477227
Dissociation energies	**B3LYP**	**M06-L**	**MN15-L**
Fe^+(benzene) (*m* = 2)	59.75	79.94	90.40
Fe^+(benzene) (*m* = 4)	54.78	69.73	73.10
Fe^+(benzene) (*m* = 6)	39.02	52.35	55.78
$Fe^+(benzene)_2$ (*m* = 2)	44.66	62.76	74.13
$Fe^+(benzene)_2$ (*m* = 4)	31.36	45.10	53.15
$Fe^+(benzene)_2$ (*m* = 6)	10.15	24.35	20.12
Experimental dissociation energies			
Fe^+(benzene)		48.4 $\pm$ 0.2	
$Fe^+(benzene)_2$		48.4 $\pm$ 0.2	

The charge transfer photodissociation spectrum of the Fe^+(benzene) complex, obtained by recording the wavelength dependence of the benzene cation, was also investigated and is shown in Figure 3.20. A noisy, broad band is observed at 260 nm. This band does not match any predicted transitions for this complex (see Figure 3.16). Instead, this band is where benzene is known to have an electronic transition for the HOMO → LUMO gap.[129] The signal is not resolved enough to fully investigate. This charge transfer process was investigated in more detail using photofragment imaging by other members of the Duncan lab.[117] Using the difference in the

ionization energies of the Fe and the benzene, the known energy of the photodissociation laser, and the kinetic energy released by the complex upon dissociation, the bond dissociation energy of Fe^+(benzene) was found to be 49.3 $\pm$ 3.2 kcal/mol, which agrees well with the value determined here by the photodissociation threshold and that determined previously by collision induced dissociation.[109]

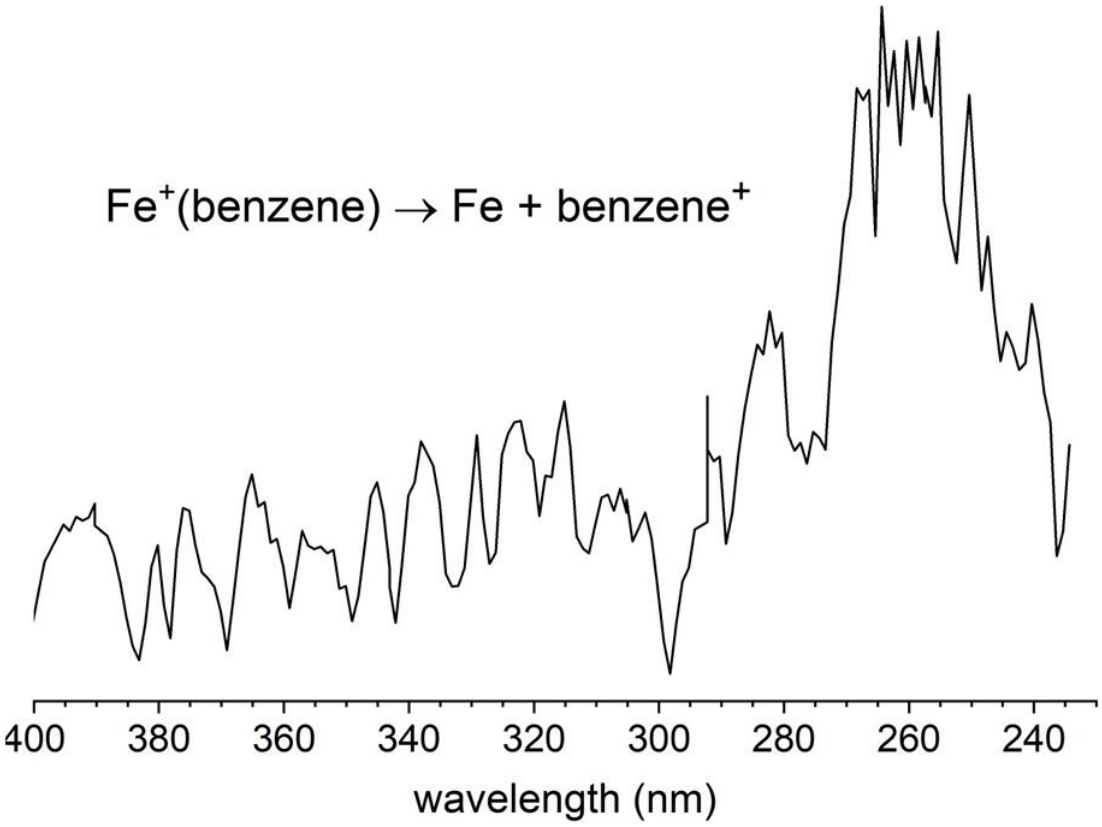

Figure 3.20. Measured photodissociation spectrum of the *charge transfer* process of Fe^+(benzene) → Fe + benzene$^+$. The signal-to-noise ratio suffers due to small amount of parent ion signal.

Fe^+(acetylene)

The bond dissociation energy of a metal ion-ligand complex can be determined by its photodissociation threshold as long as the absorption in that region of light is continuous. The

chromophore in the Fe^+(benzene) complex comes from the atomic transitions of the Fe^+ cation, so complexes of Fe^+ with similar ligands are also ideal targets for this technique. A similar cation-π bond is seen in the Fe^+(acetylene) complex. Figure 3.21 presents the mass spectrum of $Fe^+(acetylene)_n$, and Figure 3.22 shows the photodissociation difference mass spectrum of the n = 1 complex. These complexes are created using a mixture of gas (1% acetylene in argon).

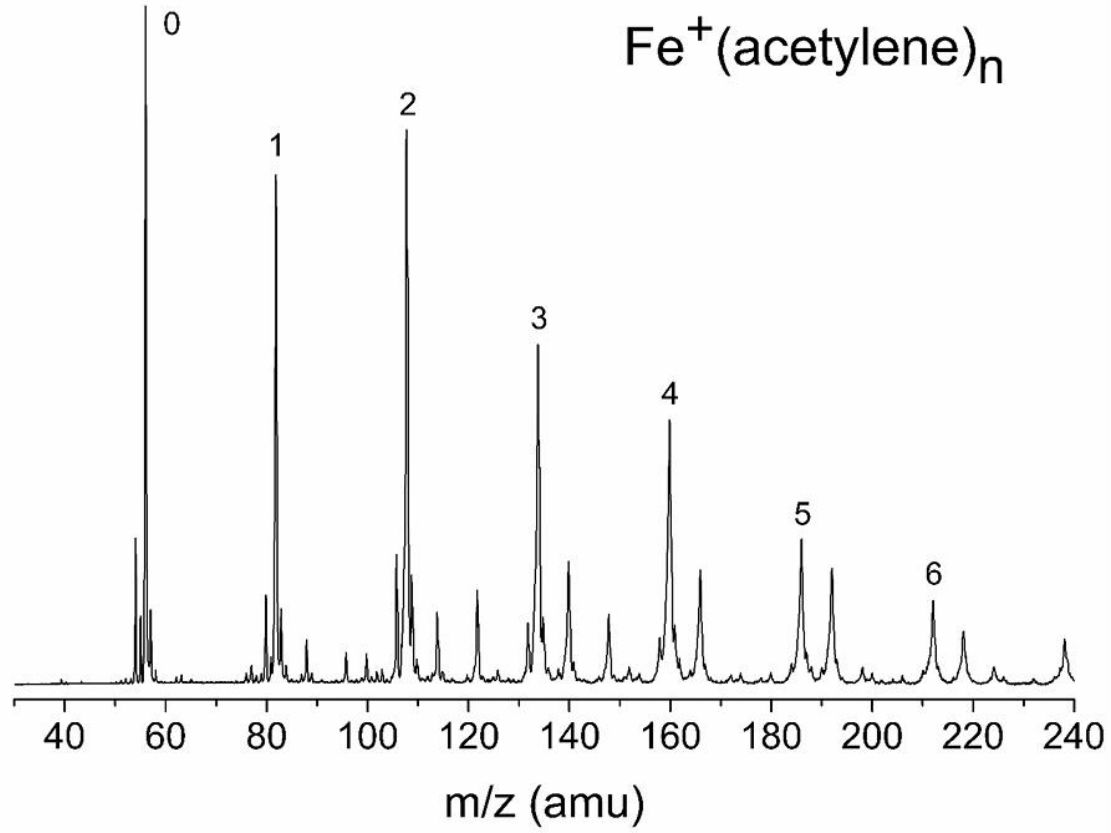

Figure 3.21. Mass spectrum of an iron rod vaporized in an expansion of a mix of 1% acetylene in argon.

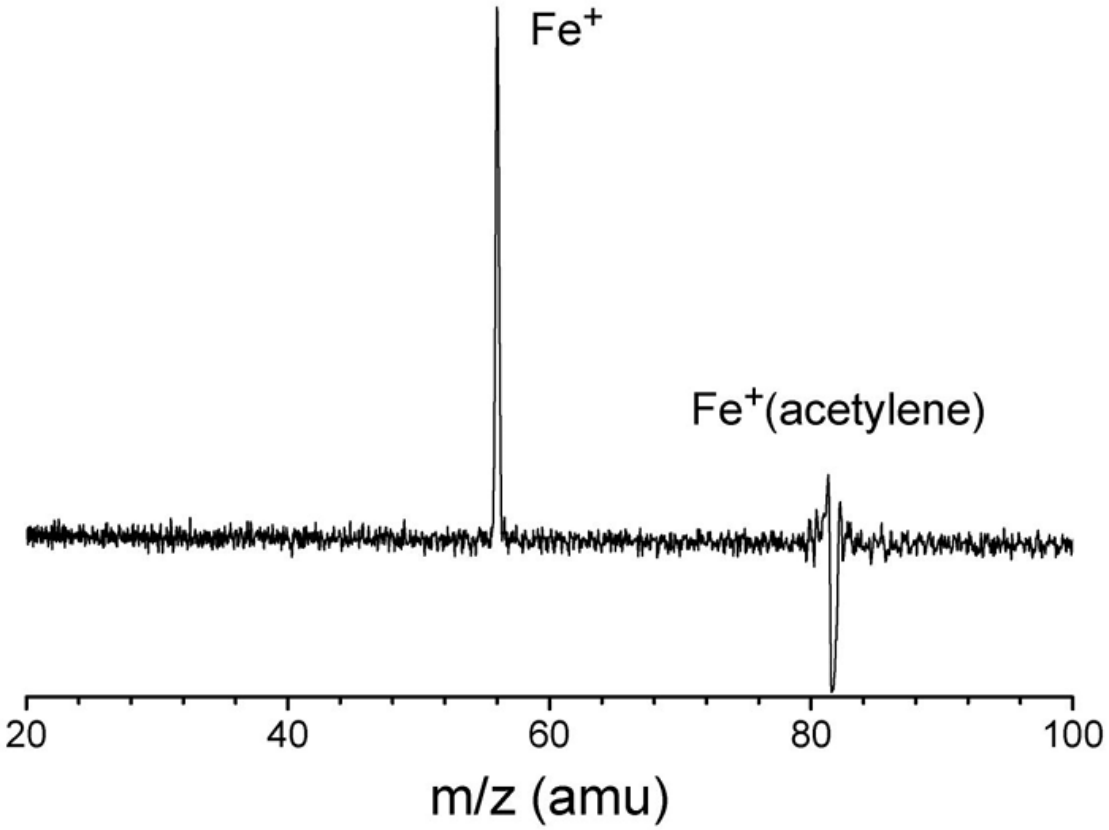

Figure 3.22. Photodissociation mass spectrum of Fe^+(acetylene) → Fe^+ + acetylene, obtained at 532 nm.

Figure 3.23 shows the photodissociation spectrum of the Fe^+(acetylene) complex, observing the appearance of Fe^+ cation. Again, there are different electronic and spin states that need to be considered: *m = 2,4,6*. Though the scale is significantly different, there is photodissociation measured throughout the visible up to about 680 nm. Theory optimizes the complex into a C_{2v} symmetry for all spin states, where the Fe^+ is above the C-C bond and the hydrogens are pushed out of line from the C-C bond. There are no transitions predicted in the visible region for *m = 2*, and those predicted for *m = 6* lie below 450 nm, so only the *m = 4* spin state is consistent with the spectrum measured. This spin state is also calculated to be the most stable by TD-DFT using B3LYP, MN15-L, and M06-L as shown in Table 3.2.

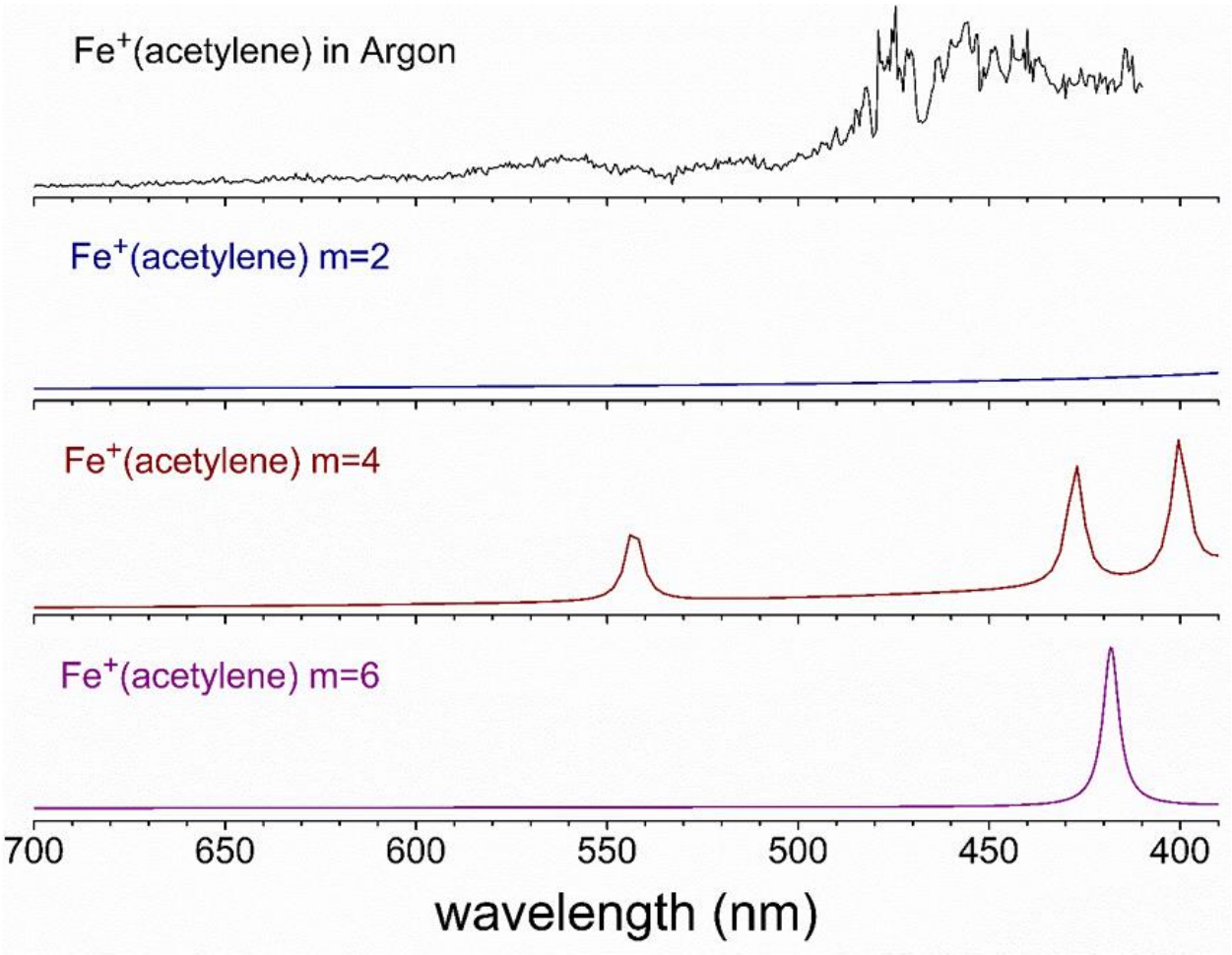

Figure 3.23. Photodissociation spectrum and electronic spectra of spin states *m = 2,4,6* predicted by TD-DFT for the Fe^+(acetylene) complex. There are no low-lying electronic transitions predicted for the *m = 2* state.

Table 3.2. Computed energetics for $Fe^+(C_2H_2)$ complexes employing different DFT functionals. Energies are in Hartrees/particle, except for dissociation energies (D_0) which are in kcal/mol. The dissociation energies are for the potential energy surface corresponding to the same spin state and are zero-point corrected.

	B3LYP	**M06-L**	**MN15-L**
acetylene	–77.338432	–77.320401	–77.260029
Fe^+ (m = 2)	–1263.369688	–1263.283754	–1263.28030
Fe^+ (m = 4)	–1263.411346	–1263.323876	–1263.304679
Fe^+ (m = 6)	–1263.404095	–1263.310728	–1263.311894
$Fe^+(C_2H_2)$ (m = 2)	–1340.785482	–1340.691221	–1340.586590
$Fe^+(C_2H_2)$ (m = 4)	–1340.823713	–1340.738484	–1340.656796
$Fe^+(C_2H_2)$ (m = 6)	–1340.777256	–1340.678001	–1340.616880
Fe^+–(C_2H_2) (m = 2) D_0	48.5	54.6	61.8
Fe^+–(C_2H_2) (m = 4) D_0	46.4	59.1	57.8
Fe^+–(C_2H_2) (m = 6) D_0	21.8	29.4	28.2

The spectrum is shown again in Figure 3.24 with assignments for the predicted transitions for the *m = 4* complex. In order of lowest-to-highest energy, there are predictions for transitions from the ground state ($^4B_1$) into a $^4B_2$, then a $^4B_1$, then another $^4B_2$ state. These predicted transitions do not take into consideration any vibronic structure, so the density of states that are predicted is sparse compared to the continuous spectrum measured.

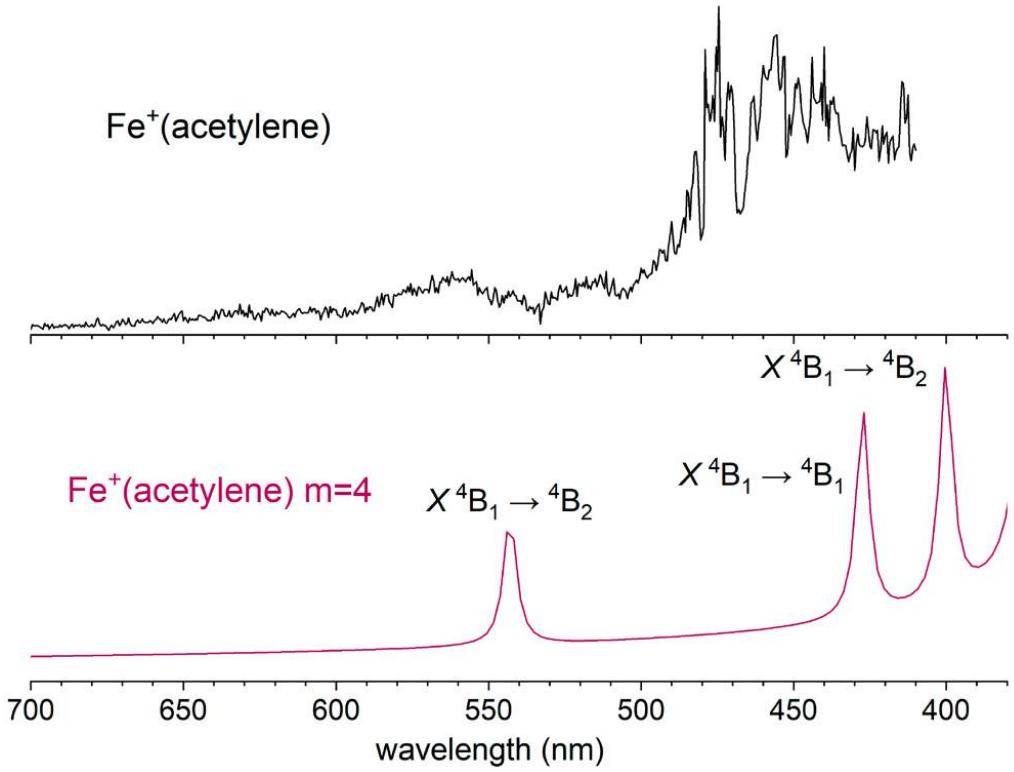

Figure 3.24. Measured photodissociation spectrum of Fe^+(acetylene) → Fe^+ + acetylene. The lower trace is the spectrum predicted by TD-DFT for a spin state of m = 4. While there is a difference in photodissociation intensity throughout the spectrum, when the photon energy overcomes the BDE threshold, the photodissociation signal becomes continuous.

The same bond dissociation energy determination made previously for Fe^+(benzene) can be made using the photodissociation threshold in the spectrum of Fe^+(acetylene). Figure 3.25 shows an expanded view of the photodissociation threshold. The onset of dissociation is 679 $\pm$ 3 nm or 42.1 $\pm$ 0.2 kcal/mol. The same consideration of the ground spin state of the Fe^+ must be taken into consideration, which is a difference of 1873 cm^{-1} (or 5.4 kcal/mol).[121] After this correction, the adiabatic dissociation energy for Fe^+(acetylene) is 36.8 $\pm$ 0.2 kcal/mol. This value compares well with the bond energy determined by collision-induced dissociation, 38.0 $\pm$ 2.6 kcal/mol.[130] The photofragment image of dissociative charge transfer was also investigated by other members of the Duncan lab.[131] Again, this determination uses the difference in ionization energy of Fe and acetylene, the known energy per photon of the photodissociation laser, and the

kinetic energy released upon photodissociation. The bond energy for the Fe^+(acetylene) complex measured with photofragment imaging was determined to be 34.6 $\pm$ 3.2 kcal/mol, which agrees well with those found by the photodissociation threshold here and by the collision induced dissociation measured previously.

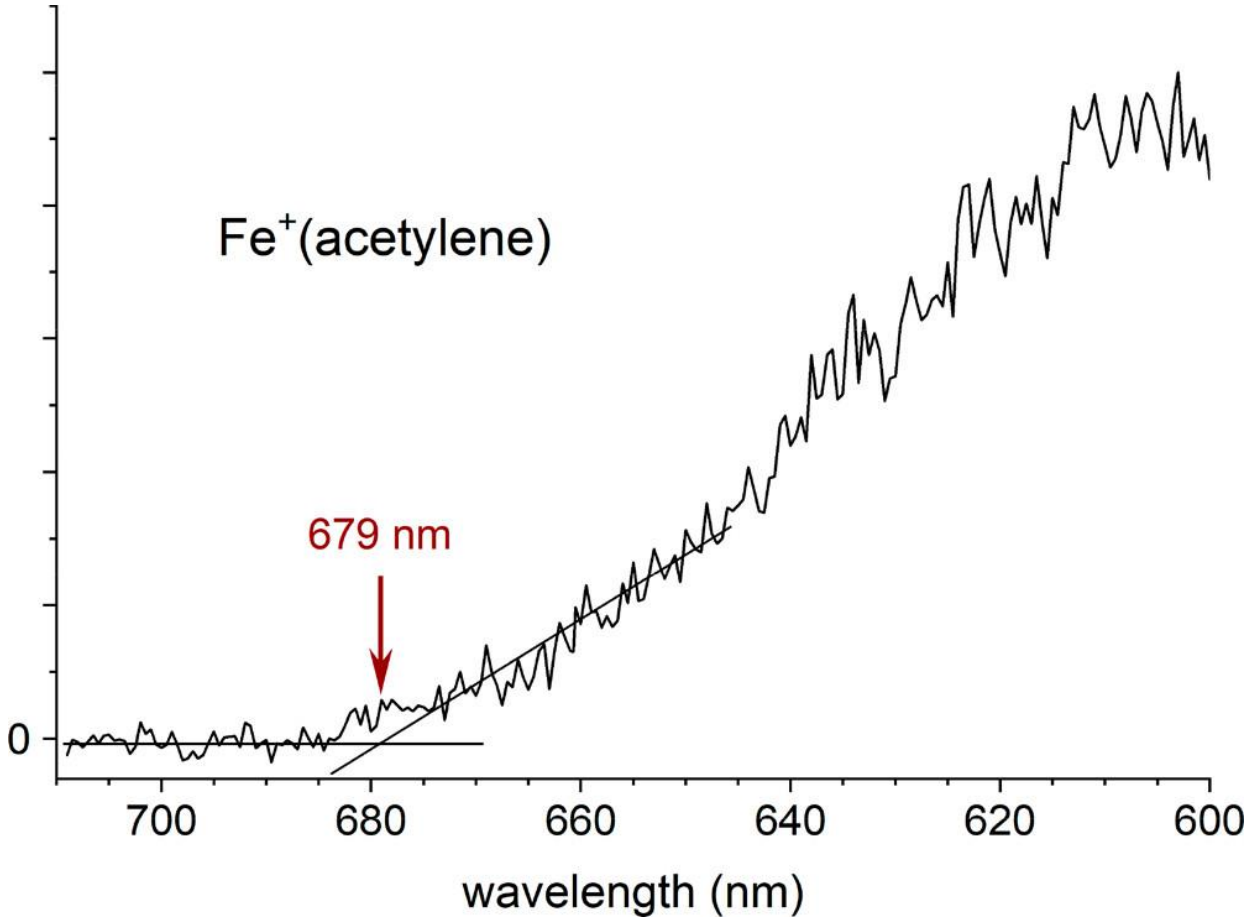

Figure 3.25. The photodissociation threshold of Fe^+(acetylene) → Fe^+ + acetylene.

Another interesting feature of the photodissociation spectrum of Fe^+(acetylene) is the change in the level of signal near 480 nm. This increase does not correspond to any transition predicted by TD-DFT. However, this energy is approximately as far above the dissociation energy (679 nm) as the energy difference between the atomic Fe^+ ^6D and ^4D states (7955 cm^{-1}). The increase in signal level is gradual and difficult to pinpoint. However, this increase in

photodissociation product has been seen previously for other systems,[132,133] occurring above the photodissociation threshold with the same spacing as the energy of the atomic transitions of the metal ion. In fact, this second threshold can be used to derive dissociation energies.

Table 3.3 shows the comparison of bond dissociation energies calculated using B3LYP, M06-L, and MN15-L. Again, it is observed that the value found by B3LYP is more accurate than those determined by the Minnesota functionals that are designed to better describe the electronic structure of transition metals.

Table 3.3. Comparison of Fe^+(acetylene) bond dissociation energy calculated with different methods for three spin states, m = 2, 4, and 6. With all methods, m = 4 was found to be the most stable. The experimentally measured dissociation threshold for Fe^+(acetylene) is 36.8 $\pm$ 0.2 kcal/mol (after correcting for the spin state difference).

Fe^+(acetylene)	B3LYP	M06-L	MN15-L
m = 2	48.5	54.6	61.8
m = 4	46.4	59.1	57.8
m = 6	21.8	29.4	28.2

U^+(benzene), UO^+(benzene), and $UO^+(CO_2)$

As there is much interest in the chemistry of actinides, our lab has recently been investigating the complexation of a uranium ion with molecules such as O_2,[134] N_2,[135] and CO_2. Again, the photodissociation threshold can be used to determine the upper limit for the bond energy of any complex that absorbs continuously. Early actinides and lanthanides have a large density of spin and electronic states, similar to Fe^+. The bonding of uranium and its ions is of particular interest due to the concerns of nuclear waste. To gain further insight into the bonding and solvation of uranium, the photodissociation thresholds of uranium complexes were measured. A mass spectrum showing the production of U^+(benzene) and $(UO)^+$(benzene) complexes is shown in Figure 3.26. The rod of uranium readily oxidizes if left in open air, so

uranium oxide cations and complexes containing it are found in most mass spectra. Uranium oxides are also present in solutions of uranium, so their chemistry is also of interest.

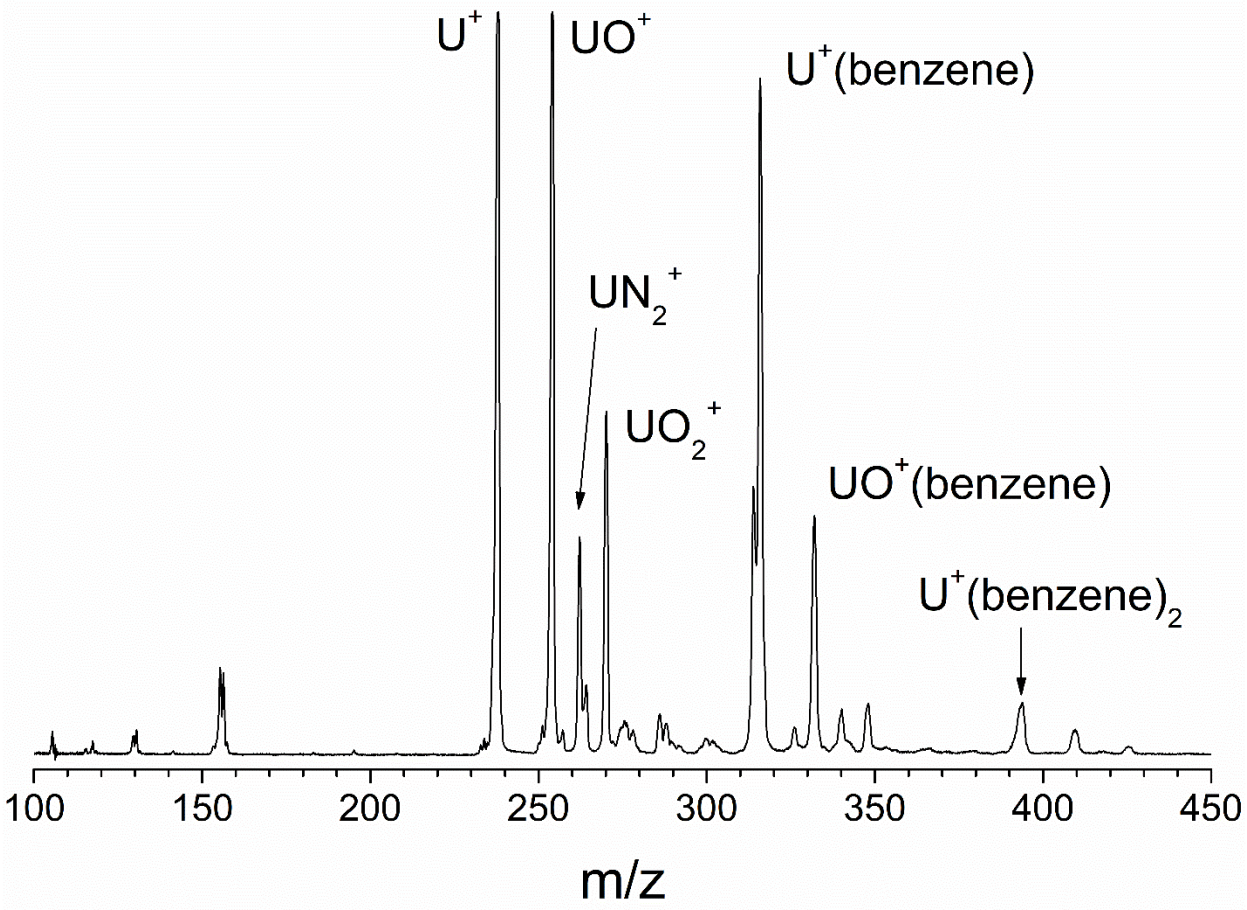

Figure 3.26. Mass spectrum of laser ablation of uranium in a benzene-seeded expansion of argon. Early mass peaks correspond to benzene clusters and other contaminates. UO_2^+(benzene) was observed, but not with enough signal to photodissociate.

The photodissociation threshold scans of these uranium complexes are shown in Figure 3.26. The bond dissociation energy of U^+(benzene) was found to be 42.5 $\pm$ 0.1 kcal/mol., while the bond dissociation energy of UO^+(benzene) was determined to be 41.0 $\pm$ 0.1 kcal/mol. The ionization energy of uranium is about 6.2 eV, and the ionization energy of UO^+ is about 5.6 eV, so the charge will be located on the U or UO. Benzene likely binds to the uranium opposite to the oxygen due to its size, and theory confirms this structure. The addition of oxygen weakens the

bond between the U^+ and benzene. The bond dissociation energy of $U^+(CO_2)$ was found to be 19.8 $\pm$ 0.1 kcal/mol. Theory on uranium atoms requires much more care than that on iron. Firstly, the number of electrons involved is much larger. Secondly, uranium is a heavy metal and thus requires a relativistic treatment of the electrons. TD-DFT calculations were carried out to find the most stable spin state and calculated bond dissociation energies. A Stuttgart/Cologne fully relativistic, 60-electron effective-core potential with the corresponding cc-pVTZ-PP basis set was used for the uranium atom in the complexes with benzene. The $UO^+(CO_2)$ complex was calculated as a part of a study on the solvation of $UO^+(CO_2)_n$, where the basis set used was cc-pVDZ (and its corresponding fully relativistic, 60-electron effective-core potential) to allow the study of further solvation, though this study is not yet published. Furthermore, the most stable structure of $UO^+(CO_2)$ found by theory has the shared oxygen atom more towards the uranium cation (i.e. $UO_2^+(CO)$); this is shown in Figure 3.28, where Isomer 1 is predicted to be more stable by 51.7 kcal/mol. The experimental and computed bond dissociation energies for all uranium ion complexes are shown in Table 3.4. The bond dissociation energy calculated for Isomer 1 of 65.0 kcal/mol is much higher than what is measured. Furthermore, the photodissociation product detected is UO^+, while Isomer 1 would likely dissociate into UO_2^+ and CO. The bond dissociation energy determined by experiment more closely agrees with the calculated binding energy of Isomer 2. There are no binding energies determined by collision-induced dissociation or photofragment imaging at this time. The calculated values agree well with the measured photodissociation threshold. More complexes must be studied, but the effective-core potentials used for these calculations show promise for accurate thermochemistry involving actinides.

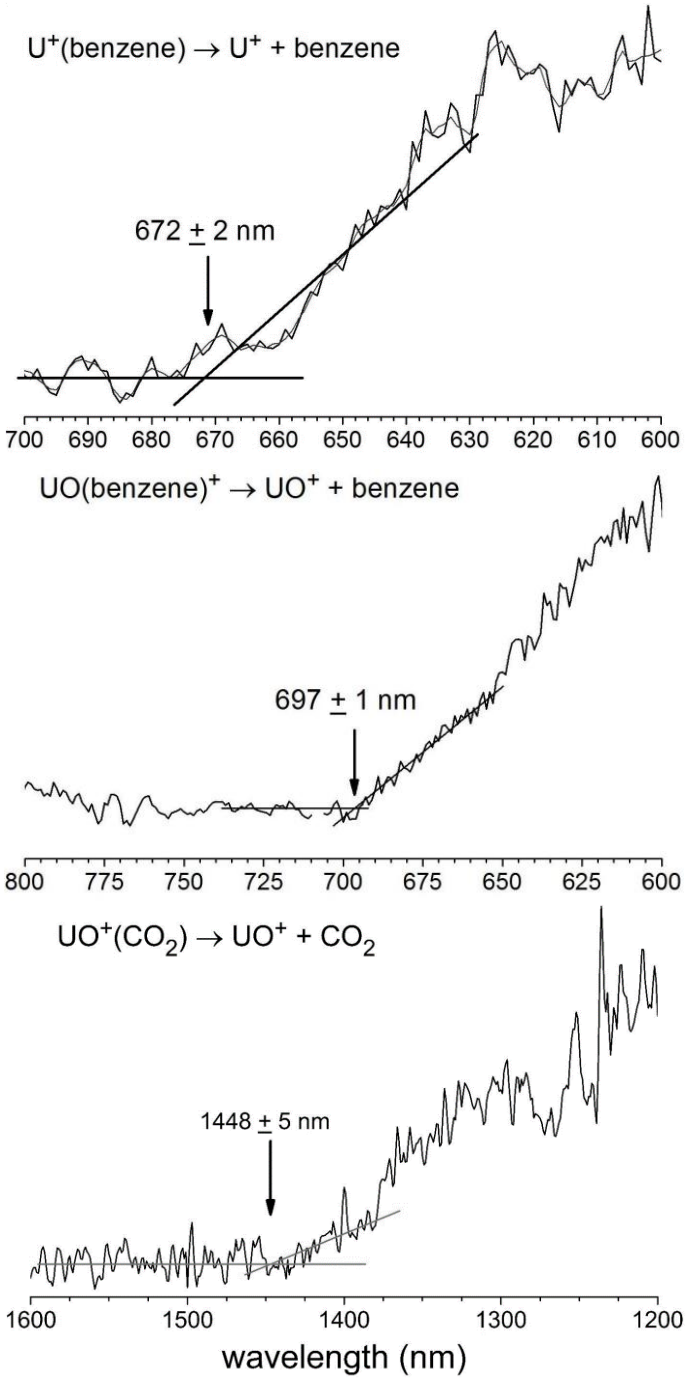

Figure 3.27. Photodissociation threshold scans of U^+(benzene), UO^+(benzene), and $U^+(CO_2)$.

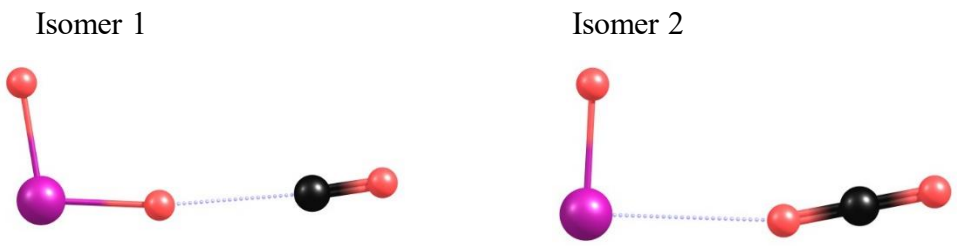

Figure 3.28. Two computed structures for $UO^+(CO_2)$. Isomer 1 is calculated to be more stable by 51.7 kcal/mol, but the bond dissociation energy measured is closer to that of Isomer 2.

Table 3.4. Bond dissociation energies determined by photodissociation threshold compared to calculated values, both given in kcal/mol. Two isomers are considered for the $UO^+(CO_2)$ complex.

Complex	Experimental Values	Theoretical Values
U^+(benzene)	42.6 ± 0.1	47.3
UO^+(benzene)	41.0 ± 0.1	41.0
$UO^+(CO_2)$	19.8 ± 0.1	65.0, 16.6

CONCLUSIONS

Electronic spectroscopy provides an invaluable look at the electronic landscape of the complexation of metal ions and organic ligands. The specific complexes investigated in this dissertation offer information on the interactions of cation-π bonding. These complexes are model systems for larger polycyclic aromatic compounds, where bonding to the π-cloud of the arene is common. Fe^+(acetylene) complexes show just how sensitive the complex is to the atomic transitions of the bare metal cation. Along with collision-induced dissociation and photofragment imaging, photodissociation threshold determination is one of the few experiments that can find the upper limit of the bond dissociation energy of metal ion-ligand complexes in the gas phase. While this threshold does represent an upper limit for the binding energy, the close agreement with collision-induced dissociation and photofragment imaging suggests it can be used to determine true dissociation energies for some complexes. Photodissociation thresholds were employed on Fe^+ and U^+-containing complexes, but there remain many different ligands

and transition metals to investigate. Transition metals with many spin states are ideal targets for this experiment, such as chromium and nickel. Complexing these metals with other organic ligands will lead to trends in bonding that can be expanded to larger, more complicated systems, such as the types of molecules used in chemosensors. Even with methods designed for transition metals, theory of these systems struggles to accurately describe the binding energies and the electronic structure that were observed in the photodissociation spectra, though on some systems, B3LYP is adequate. Metal ion-molecule complexes continue to be challenging systems for experiment and theory.

REFERENCES

1. Hartwig, J. *Organotransition Metal Chemistry: From Bonding to Catalysis*, 1st edition.; University Science Books: Sausalito, Calif, 2009.
2. Astruc, D. *Organometallic Chemistry and Catalysis*, 2007th edition.; Springer: Berlin ; New York, 2007.
3. Parshall, G. W. Organometallic Chemistry in Homogeneous Catalysis. *Science* **1980**, *208*, 1221–1224.
4. Crabtree, R. H. *The Organometallic Chemistry of the Transition Metals, 4th Edition*, 4th edition.; Wiley-Interscience: Hoboken, N.J, 2005.
5. H. Sinn, W. Kaminsky. *Ziegler-Natta catalysis. In Advances in Organometallic Chemistry, Vol. 18*; Stone, F. G. A., West, R., Eds.; Academic Press: New York, 1980.
6. Frenking, G.; Fröhlich, N. The Nature of the Bonding in Transition-Metal Compounds. *Chem. Rev.* **2000**, *100*, 717–774.
7. A. Osborn, J.; H. Jardine, F.; F. Young, J.; Wilkinson, G. The Preparation and Properties of Tris(Triphenylphosphine)Halogenorhodium(I) and Some Reactions Thereof Including Catalytic Homogeneous Hydrogenation of Olefins and Acetylenes and Their Derivatives. *J. Chem. Soc.* **1966**, 1711–1732.
8. Russell, D. H. *Gas Phase Inorganic Chemistry*; Springer Science & Business Media, 2012.
9. Eller, Karsten.; Schwarz, Helmut. Organometallic Chemistry in the Gas Phase. *Chem. Rev.* **1991**, *91*, 1121–1177.
10. *Organometallic Ion Chemistry*, 1996th edition.; Freiser, B. S., Ed.; Springer: Dordrecht ; Boston, 1996.

11. Leary, J. A.; Armentrout, P. B. Gas Phase Metal Ion Chemistry: From Fundamentals to Biological Interactions. *Int. J. Mass Spectrom.* **2001**, *204*, 9–10.

12. Hettich, R. L.; Jackson, T. C.; Stanko, E. M.; Freiser, B. S. Gas-Phase Photodissociation of Organometallic Ions. Bond Energy and Structure Determinations. *J. Am. Chem. Soc.* **986**, *108*, 5086–5093.

13. Huang, Y.; Freiser, B. S. Gas-Phase Study of Fe^+-Benzyne with Alkanes. *J. Am. Chem. Soc.* **1989**, *111*, 2387–2393.

14. Armentrout, P. B. Electronic State-Specific Transition Metal Ion Chemistry. *Annu. Rev. Phys. Chem.* **1990**, *41*, 313–344.

15. Schröder, D.; Sülzle, D.; Hrušák, J.; Böhme, D. K.; Schwarz, H. Neutralization—Reionization Mass Spectrometry as a Novel Probe to Structurally Characterize Organic Ligands Generated in the Fe(I)-Mediated Oligomerization of Acetylene in the Gas Phase. *Int. J. Mass Spectrom.* **1991**, *110*, 145–156.

16. Sodupe, M.; Bauschlicher Jr, C. W. Theoretical Study of the Bonding of the First-and Second-Row Transition-Metal Positive Ions to Acetylene. *J. Phys. Chem.* **1991**, *95*, 8640–8645.

17. Schnabel, P.; Irion, M. P.; Weil, K. G. Evidence for Low-Pressure Catalysis in the Gas Phase by a Naked Metal Cluster: The Growth of Benzene Precursors on Iron (Fe_4^+). *J. Phys. Chem.* **1991**, *95*, 9688–9694.

18. Schnabel, P.; Weil, K. G.; Irion, M. P. Proof of the Catalytic Activity of a Naked Metal Cluster in the Gas Phase. *Angew. Chem., Int. Ed. Engl.* **1992**, *31*, 636–638.

19. Schröder, D.; Schwarz, H. Ligand Effects as Probes for Mechanistic Aspects of Remote C-H Bond Activation by Iron(I) Cations in the Gas Phase. *J. Organomet. Chem*. **1995**, *504*, 123–135.

20. Surya, P. I.; Roth, L. M.; Ranatunga, D. R. A.; Freiser, B. S. Infrared Multiphoton Dissociation of Transition Metal Containing Ions: $MC_nH_{2n}^+$ (M = Fe, Co, Ni; n = 2−5). *J. Am. Chem. Soc.* **1996**, *118*, 1118–1125.

21. Surya, P. I.; Ranatunga, D. R. A.; Freiser, B. S. Infrared Multiphoton Dissociation of $MC_4H_6^+$ [M = Fe, Co, or Ni; C_4H_6 = 1,3-Butadiene or $(C_2H_2)(C_2H_4)$]. *J. Am. Chem. Soc.* **1997**, *119*, 3351–3357.

22. Baranov, V.; Becker, H.; Bohme, D. K. Intrinsic Coordination Properties of Iron: Gas-Phase Ligation of Ground-State Fe^+ with Alkanes, Alkenes, and Alkynes and Intramolecular Interligand Interactions Mediated by Fe^+. *J. Phys. Chem. A* **1997**, *101*, 5137–5147.

23. Petrie, S.; Becker, H.; Baranov, V.; Bohme, D. K. Association Reactions of Fe^+ with Hydrocarbons: Implications for Dense Interstellar Cloud Chemistry. *Astrophys. J.* **1997**, *476*, 191-198.

24. Frenking, G.; Fröhlich, N. The Nature of the Bonding in Transition-Metal Compounds. *Chem. Rev.* **2000**, *100*, 717–774.

25. Klippenstein, S. J.; Yang, C.-N. Density Functional Theory Predictions for the Binding of Transition Metal Cations to pi Systems: From Acetylene to Coronene and Tribenzocyclyne. *Int. J. Mass Spectrom.* **2000**, *201*, 253–267.

26. Chrétien, S.; Salahub, D. R. Kohn–Sham Density-Functional Study of the Adsorption of Acetylene and Vinylidene on Iron Clusters, Fe_n/Fe_n^+ (n=1–4). *J. Chem. Phys.* **2003**, *119*, 12279–12290.

27. Jacobson, D. B.; Freiser, B. S. Studies of the Reactions of Group 8 Transition-Metal Ions Fe^+, Co^+, and Ni^+ with Linear Alkanes. Determination of Reaction Mechanisms and $MC_nH_{2n}^+$ Ion Structures Using Fourier Transform Mass Spectrometry Collision-Induced Dissociation. *J. Am. Chem. Soc.* **1983**, *105*, 5197–5206.

28. Martinez, M.; del Carmen Michelini, M.; Rivalta, I.; Russo, N.; Sicilia, E. Acetylene Cyclotrimerization by Early Second-Row Transition Metals in the Gas Phase. A Theoretical Study. *Inorg. Chem.* **2005**, *44*, 9807–9816.

29. Böhme, D. K.; Schwarz, H. Gas-Phase Catalysis by Atomic and Cluster Metal Ions: The Ultimate Single-Site Catalysts. *Angew. Chem. Int. Ed.* **2005**, *44*, 2336–2354.

30. Schlangen, M.; Schwarz, H. Effects of Ligands, Cluster Size, and Charge State in Gas-Phase Catalysis: A Happy Marriage of Experimental and Computational Studies. *Catal. Lett.* **2012**, *142*, 1265–1278.

31. Rodgers, M. T.; Armentrout, P. B. Cationic Noncovalent Interactions: Energetics and Periodic Trends. *Chem. Rev.* **2016**, *116*, 5642–5687.

32. Schwarz, H. Ménage-à-Trois: Single-Atom Catalysis, Mass Spectrometry, and Computational Chemistry. *Catal. Sci. Technol.* **2017**, *7*, 4302–4314.

33. Citek, C.; Oyala, P. H.; Peters, J. C. Mononuclear Fe(I) and Fe(II) Acetylene Adducts and Their Reductive Protonation to Terminal Fe(IV) and Fe(V) Carbynes. *J. Am. Chem. Soc.* **2019**, *141*, 15211–15221.

34. Metz, R. B. Photofragment Spectroscopy of Covalently Bound Transition Metal Complexes: A Window into C–H and C–C Bond Activation by Transition Metal Ions. *Int. Rev. Phys. Chem*. **2004**, *23*, 79–108.

35. MacAleese, L.; Maître, P. Infrared Spectroscopy of Organometallic Ions in the Gas Phase: From Model to Real World Complexes. *Mass Spectrom. Rev.* **2007**, *26*, 583–605.

36. Fioroni, M. Astro-Organometallics of Fe, Co, Ni: Stability, IR Fingerprints and Possible Locations. *Comput. Theor. Chem*. **2016**, *1084*, 196–212.

37. Duncan, M. A. Metal Cation Coordination and Solvation Studied with Infrared Spectroscopy in the Gas Phase. In *Physical Chemistry of Cold Gas-Phase Functional Molecules and Clusters*; Ebata, T., Fujii, M., Eds.; Springer: Singapore, 2019; pp 157–194.

38. Brathwaite, A. D.; Ward, T. B.; Walters, R. S.; Duncan, M. A. Cation−π and CH−π Interactions in the Coordination and Solvation of $Cu^+(Acetylene)_n$ Complexes. *J. Phys. Chem. A* **2015**, *119*, 5658–5667.

39. Ward, T. B.; Brathwaite, A. D.; Duncan, M. A. Infrared Spectroscopy of $Au(Acetylene)_n^+$ Complexes in the Gas Phase. *Top. Catal.* **2018**, *61*, 49–61.

40. Marks, J. H.; Ward, T. B.; Brathwaite, A. D.; Duncan, M. A. Infrared Spectroscopy of $Zn(Acetylene)_n^+$ Complexes: Ligand Activation and Nascent Polymerization. *J. Phys. Chem. A* **2020**, *124*, 4764–4776.

41. Batchelor, A. G.; Marks, J. H.; Ward, T. B.; Duncan, M. A. $Pt^+(C_2H_2)_n$ Complexes Studied with Selected-Ion Infrared Spectroscopy. *J. Phys. Chem. A* **2023**, *127*, 5704–5712.

42. Brathwaite, A. D.; Marks, J. H.; Webster, I. J.; Batchelor, A. G.; Ward, T. D.; Duncan, M. A. Coordination and Spin States in $Fe^+(C_2H_2)_n$ Complexes Studied with Selected-Ion Infrared Spectroscopy. *J. Phys. Chem. A* **2022**, *126*, 9680–9690.

43. Brathwaite, A. D.; Ward, T. B.; Marks, J. H.; Duncan, M. A. Coordination and Solvation in Gas-Phase $Ag^+(C_2H_2)_n$ Complexes Studied with Selected-Ion Infrared Spectroscopy. *J. Phys. Chem. A* **2020**, *124*, 8562–8573.

44. Marks, J. H.; Ward, T. B.; Duncan, M. A. Infrared Spectroscopy of Coordination and Solvation in $Cu^+(C_2H_4)_n$ (n = 1–9) Complexes. *Int. J. Mass Spectrom.* **2019**, *435*, 107–113.

45. Duncan, M. A. Structures, Energetics and Spectroscopy of Gas Phase Transition Metal Ion–Benzene Complexes. *Int. J. Mass Spectrom.* **2008**, *272*, 99–118.

46. Castro, M.; Flores, R.; Duncan, M. A. Theoretical Study of Nascent Solvation in $Ni^+(Benzene)_m$, m = 3 and 4, Clusters. *J. Phys. Chem. A* **2013**, *117*, 12546–12559.

47. Reishus, K. N.; Brathwaite, A. D.; Mosley, J. D.; Duncan, M. A. Coordination versus Solvation in $Al^+(Benzene)_n$ Complexes Studied with Infrared Spectroscopy. *J. Phys. Chem. A* **2014**, *118*, 7516–7525.

48. Marks, J. H.; Ward, T. B.; Brathwaite, A. D.; Ferguson, S.; Duncan, M. A. Cyclotrimerization of Acetylene in Gas Phase $V^+(C_2H_2)_n$ Complexes: Detection of Intermediates and Products with Infrared Spectroscopy. *J. Phys. Chem. A* **2019**, *123*, 6733–6743.

49. McDonald, D. C. I.; Sweeny, B. C.; Viggiano, A. A.; Ard, S. G.; Shuman, N. S. Cyclotrimerization of Acetylene under Thermal Conditions: Gas-Phase Kinetics of V^+ and $Fe^+ + C_2H_2$. *J. Phys. Chem. A* **2021**, *125*, 9327–9337.

50. Gan, W.; Geng, L.; Yin, B.; Zhang, H.; Luo, Z.; Hansen, K. Cyclotrimerization of Acetylene on Clusters $Co_n^+/Fe_n^+/Ni_n^+$(n = 1–16). *J. Phys. Chem. A* **2021**, *125*, 10392–10400.

51. Muetterties, E. L.; Bleeke, J. R.; Wucherer, E. J.; Albright, T. Structural, Stereochemical, and Electronic Features of Arene-Metal Complexes. *Chem. Rev.* **1982**, *82*, 499–525.

52. Ma, J. C.; Dougherty, D. A. The Cation−π Interaction. *Chem. Rev.* **1997**, *97*, 1303–1324.

53. Long, N. J. *Metallocenes: An Introduction to Sandwich Complexes*, 1st edition.; Wiley-Blackwell: Oxford, OX ; Malden, MA, USA, 1998.

54. Astruc, D. *Organometallic Chemistry and Catalysis*, 2007th edition.; Springer: Berlin ; New York, 2007.

55. Crabtree, R. H. *The Organometallic Chemistry of the Transition Metals, 4th Edition*, 4th edition.; Wiley-Interscience: Hoboken, NJ, 2005.

56. Bersuker, I. B. *Electronic Structure and Properties of Transition Metal Compounds: Introduction to the Theory*, 2nd edition.; Wiley: Hoboken, NJ, 2010.

57. Mahadevi, A. S.; Sastry, G. N. Cation−π Interaction: Its Role and Relevance in Chemistry, Biology, and Material Science. *Chem. Rev.* **2013**, *113*, 2100–2138.

58. Dougherty, D. A. The Cation−π Interaction. *Acc. Chem. Res.* **2013**, *46*, 885–893.

59. Winstein, S.; Lucas, H. J. The Coördination of Silver Ion with Unsaturated Compounds. *J. Am. Chem. Soc.* **1938**, *60*, 836–847.

60. Mulliken, R. S. Molecular Compounds and Their Spectra. II. *J. Am. Chem. Soc.* **1952**, *74*, 811–824.

61. Andrews, L. J. Aromatic Molecular Complexes of the Electron Donor-Acceptor Type. *Chem. Rev.* **1954**, *54*, 713–776.

62. Smith, H. G.; Rundle, R. E. The Silver Perchlorate-Benzene Complex, $C_6H_6 \cdot AgClO_4$, Crystal Structure and Charge Transfer Energy. *J. Am. Chem. Soc.* **1958**, *80*, 5075–5080.

63. Traynham, J. G.; Olechowski, J. R. Complexation of Cyclic Olefins with Aqueous Silver Ion and with Molecular Iodine[1,2]. *J. Am. Chem. Soc.* **1959**, *81*, 571-574.

64. Gut, R.; Rueede, J. The Formation of Silver—Arene Complexes in Liquid Anhydrous Hydrogen Fluoride. *J. Organomet. Chem.* **1977**, *128*, 89–93.

65. Kealy, T. J.; Pauson, P. L. A New Type of Organo-Iron Compound. *Nature* **1951**, *168*, 1039–1040.

66. Miller, S. A.; Tebboth, J. A.; Tremaine, J. F. Dicyclopentadienyliron. *J. Chem. Soc.* **1952**, *632*, 632-635.

67. Fischer, E. O.; Hafner, W. Di-benzol-chrom: Über Aromatenkomplexe von Metallen I. *Z Naturforsch.* **1955**, *10*, 665-668.

68. Fritz, H. P. Infrared and Raman Spectral Studies of π Complexes Formed Between Metals and C_nH_nRings. In *Advances in Organometallic Chemistry*; Stone, F. G. A., West, R., Eds.; Academic Press, 1964; Vol. 1, pp 239–316.

69. Prins, R.; Reinders, F. J. Electron Spin Resonance Measurements of Dibenzenechromium Cation. *Chem. Phys. Lett.* **1969**, *3*, 45–48.

70. Aleksanyan, V. T. Vibrational Spectra of Sandwich Complexes. In *Vibrational spectra and structure*. Amsterdam: Elsevier, 1982.

71. Cabelli, D. E.; Cowley, A. H.; Lagowski, J. J. The Bonding in Some Bis(Arene)Chromium Compounds as Indicated by U.V. Photoelectron Spectroscopy. *Inorg. Chim. Acta* **1982**, *57*, 195–198.

72. Muetterties, E. L.; Bleeke, J. R.; Wucherer, E. J.; Albright, T. Structural, Stereochemical, and Electronic Features of Arene-Metal Complexes. *Chem. Rev.* **1982**, *82*, 499–525.

73. Andrews, M. P.; Mattar, S. M.; Ozin, G. A. (η^6-C_6H_6)V and (η^6-C_6F_6)V: An Optical, EPR, and IR Spectroscopy and Xα-MO study. 1. *J. Phys. Chem.* **1986**, *90*, 744–753.

74. Caldwell, J. W.; Kollman, P. A. Cation-π Interactions: Nonadditive Effects are Critical in their Accurate Representation. *J. Am. Chem. Soc.* **1995**, *117*, 4177-4178.

75. Gallivan, J. P.; Dougherty, D. A. Cation-π Interactions in Structural Biology. *Proc. Natl. Acad. Sci.* **1999**, *96*, 9459–9464.

76. Nakamoto, K. *Infrared and Raman Spectra of Inorganic and Coordination Compounds, Part B: Applications in Coordination, Organometallic, and Bioinorganic Chemistry, 5th Edition*; Wiley-Interscience: New York, 1997.

77. Duff, A. W.; Jonas, K.; Goddard, R.; Kraus, H. J.; Krueger, C. The First Triple-Decker Sandwich with a Bridging Benzene Ring. *J. Am. Chem. Soc.* **1983**, *105*, 5479–5480.

78. Hoshino, K.; Kurikawa, T.; Takeda, H.; Nakajima, A.; Kaya, K. Structures and Ionization Energies of Sandwich Clusters (V_n(benzene)$_m$). *J. Phys Chem.* **1995**, *99*, 3053-3055.

79. Hoshino, K.; Kurikawa, T.; Takeda, H.; Nakajima, A.; Kaya, K. Structures of Organometallic Clusters: V_n(benzene)$_m$ and Co_n(benzene)$_m$. *Surf. Rev. Lett.* **1996**, *3*, 183-185.

80. Yasuike, T.; Nakajima, A.; Yabushita, S.; Kaya, K. Why Do Vanadium Atoms Form Multiple-Decker Sandwich Clusters with Benzene Molecules Efficiently? *J. Phys. Chem. A* **1997**, *101*, 5360–5367.

81. Nakajima, A.; Kaya, K. A Novel Network Structure of Organometallic Clusters in the Gas Phase. *J. Phys. Chem. A* **2000**, *104*, 176–191.

82. Kaya, K.; Nagao, S.; Negishi, Y.; Judai, K.; Kato, A.; Nakamura, Y.; Nakajima, A. A Novel Network Structure of Organometallic Clusters in Gas Phase. In *Cluster and Nanostructure Interfaces*; World Scientific, 2000; pp 301–309.

83. Kurikawa, T.; Takeda, H.; Hirano, M.; Judai, K.; Arita, T.; Nagao, S.; Nakajima, A.; Kaya, K. Electronic Properties of Organometallic Metal−Benzene Complexes [M_n(Benzene)$_m$ (M = Sc−Cu)]. *Organomet.* **1999**, *18*, 1430–1438.

84. Munakata, M.; Wu, L. P.; Ning, G. L.; Kuroda-Sowa, T.; Maekawa, M.; Suenaga, Y.; Maeno, N. Construction of Metal Sandwich Systems Derived from Assembly of Silver(I) Complexes with Polycyclic Aromatic Compounds. *J. Am. Chem. Soc.* **1999**, *121*, 4968–4976.

85. Kandalam, A. K.; Rao, B. K.; Jena, P.; Pandey, R. Geometry and Electronic Structure of $V_n(Bz)_m$ Complexes. *J. Chem. Phys.* **2004**, *120*, 10414–10422.

86. Wang, J.; Acioli, P. H.; Jellinek, J. Structure and Magnetism of V_nBz_{n+1} Sandwich Clusters. *J. Am. Chem. Soc.* **2005**, *127*, 2812–2813.

87. Wang, J.; Jellinek, J. Infrared Spectra of V_nBz_{n+1} Sandwich Clusters: A Theoretical Study of Size Evolution. *J. Phys. Chem. A* **2005**, *109*, 10180–10182.

88. Kua, J.; Tomlin, K. M. Computational Study of Multiple-Decker Sandwich and Rice-Ball Structures of Neutral Titanium−Benzene Clusters. *J. Phys. Chem. A* **2006**, *110*, 11988–11994.

89. Weis, P.; Kemper, P. R.; Bowers, M. T. Structures and Energetics of $V_n(C_6H_6)_m^+$ Clusters: Evidence for a Quintuple-Decker Sandwich. *J. Phys. Chem. A* **1997**, *101*, 8207–8213.

90. Miyajima, K.; Nakajima, A.; Yabushita, S.; Knickelbein, M. B.; Kaya, K. Ferromagnetism in One-Dimensional Vanadium−Benzene Sandwich Clusters. *J. Am. Chem. Soc.* **2004**, *126*, 13202–13203.

91. Miyajima, K.; Yabushita, S.; Knickelbein, M. B.; Nakajima, A. Stern−Gerlach Experiments of One-Dimensional Metal−Benzene Sandwich Clusters: $M_n(C_6H_6)_m$ (m = Al, Sc, Ti, and V). *J. Am. Chem. Soc.* **2007**, *129*, 8473–8480.

92. Miyajima, K.; Knickelbein, M. B.; Nakajima, A. Stern-Gerlach Studies of Organometallic Sandwich Clusters. *Eur. Phys. J. D* **2005**, *34*, 177–182.

93. Judai, K.; Sera, K.; Amatsutsumi, S.; Yagi, K.; Yasuike, T.; Yabushita, S.; Nakajima, A.; Kaya, K. A Soft-Landing Experiment on Organometallic Cluster Ions: Infrared Spectroscopy of V(Benzene)$_2$ in Ar Matrix. *Chem. Phys. Lett.* **2001**, *334*, 277–284.

94. Nagaoka, S.; Okada, E.; Doi, S.; Mitsui, M.; Nakajima, A. Trapping of V(Benzene)$_2$ Sandwich Clusters in a n-Alkanethiol Self-Assembled Monolayer Matrix. *Eur. Phys. J. D* **2005**, *34*, 239–242.

95. Nagaoka, S.; Matsumoto, T.; Ikemoto, K.; Mitsui, M.; Nakajima, A. Soft-Landing Isolation of Multidecker V_2(Benzene)$_3$ Complexes in an Organic Monolayer

Matrix: An Infrared Spectroscopy and Thermal Desorption Study. *J. Am. Chem. Soc.* **2007**, *129*, 1528–1529.

96. Judai, K.; Hirano, M.; Kawamata, H.; Yabushita, S.; Nakajima, A.; Kaya, K. Formation of Vanadium-Arene Complex Anions and Their Photoelectron Spectroscopy. *Chem. Phys. Lett.* **1997**, *270*, 23–30.
97. Gerhards, M.; Thomas, O. C.; Nilles, J. M.; Zheng, W.-J.; Bowen, K. H., Jr. Cobalt–Benzene Cluster Anions: Mass Spectrometry and Negative Ion Photoelectron Spectroscopy. *J. Chem. Phys.* **2002**, *116*, 10247–10252.
98. Zheng, W.; Nilles, J. M.; Thomas, O. C.; Bowen, K. H., Jr. Photoelectron Spectroscopy of Nickel-Benzene Cluster Anions. *J. Chem. Phys.* **2005**, *122*, 044306.
99. Zheng, W.; Nilles, J. M.; Thomas, O. C.; Bowen, K. H. Photoelectron Spectroscopy of Titanium–Benzene Cluster Anions. *Chem. Phys. Lett.* **2005**, *401*, 266–270.
100. Schlag, E. W. *ZEKE Spectroscopy*, 1st edition.; Cambridge University Press: Cambridge, UK ; New York, 1998.
101. Sohnlein, B. R.; Li, S.; Yang, D.-S. Electron-Spin Multiplicities and Molecular Structures of Neutral and Ionic Scandium-Benzene Complexes. *J. Chem. Phys.* **2005**, *123*, 214306.
102. Sohnlein, B. R.; Yang, D.-S. Pulsed-Field Ionization Electron Spectroscopy of Group 6 Metal (Cr, Mo, and W) Bis(Benzene) Sandwich Complexes. *J. Chem. Phys.* **2006**, *124*, 134305.
103. Sohnlein, B. R.; Lei, Y.; Yang, D.-S. Electronic States of Neutral and Cationic Bis(Benzene) Titanium and Vanadium Sandwich Complexes Studied by Pulsed Field Ionization Electron Spectroscopy. *J. Chem. Phys.* **2007**, *127*, 114302.

104. Bagratashvili, V. N.; Letokhov, V. S.; Makarov, A. A.; Ryabov, E. A. *Multiple Photon Infrared Laser Photophysics and Photochemistry*; Harwood Academic Pub, 1985.

105. Bowers, M. T. *Gas Phase Ion Chemistry*; Academic Press, 1979.

106. Dunbar, R. C. Photodissociation of Trapped Ions. *Int. J. Mass Spectrom.* **2000**, *200*, 571–589.

107. Baer, T.; Hase, W. L. *Unimolecular Reaction Dynamics: Theory and Experiments*, 1st edition.; Oxford University Press: New York, 1996.

108. von Helden, G.; van Heijnsbergen, D.; Meijer, G. Resonant Ionization Using IR Light: A New Tool to Study the Spectroscopy and Dynamics of Gas-Phase Molecules and Clusters. *J. Phys. Chem. A* **2003**, *107*, 1671–1688.

109. Meyer, F.; Khan, F. A.; Armentrout P. B. Thermochemistry of Transition Metal Benzene Complexes: Binding energies of $M(C_6H_6)_x^+$ (x= 1,2) for M= Ti to Cu. *J. Am. Chem. Soc.* **1995**, *117*, 9740.

110. Armentrout, P. B. Reactions and Thermochemistry of Small Transition Metal Cluster Ions. *Annu. Rev. Phys. Chem.* **2001**, *52*, 423–461.

111. Brown, J. M.; Hofmann, P. *Organometallic Bonding and Reactivity: Fundamental Studies*; Springer, 2003.

112. Rowland, T. G.; Sztáray, B.; Armentrout, P. B. Metal–Cyclopentadienyl Bond Energies in Metallocene Cations Measured Using Threshold Collision-Induced Dissociation Mass Spectrometry. *J. Phys. Chem. A* **2013**, *117*, 1299–1309.

113. Armentrout, P. B. Methane Activation by 5d Transition Metals: Energetics, Mechanisms, and Periodic Trends. *Chem. Eur. J.* **2017**, *23*, 10–18.

114. Brucat, P. J.; Zheng, L. -S.; Pettiette, C. L.; Yang, S.; Smalley, R. E. Metal Cluster Ion Photofragmentation. *J. Chem. Phys.* **1986**, *84*, 3078–3088.

115. Baer, T. Vacuum UV Photophysics and Photoionization Spectroscopy. *Annu. Rev. Phys. Chem.* **1989**, *40*, 637-669.

116. Dargel, T. K.; Hertwig, R. H.; Koch, W. How Do Coinage Metal Ions Bind to Benzene? *Molecular Physics* **1999**, *96*, 583–591.

117. Rittgers, B. M.; Leicht, D.; Duncan, M. A. Cation−π Complexes of Silver Studied with Photodissociation and Velocity-Map Imaging. *J. Phys. Chem. A* **2020**, *124*, 9166–9176.

118. Chen, Y.-M.; Armentrout, P. B. Collision-Induced Dissociation of Ag $(C_6H_6)^+$. *Chem. Phys. Lett.* **1993**, *210*, 123–128.

119. Dymerski, P. P.; Fu, E.; Dunbar, R. C. Ion Cyclotron Resonance Photodissociation Spectroscopy Spectra of Substituted Benzenes. *J. Am. Chem. Soc.* **1974**, *96*, 4109–4114.

120. Mei, Y.; Yang, W. Charge Transfer Excitation Energies from Ground State Density Functional Theory Calculations. *J. Chem. Phys.* **2019**, *150*, 144109.

121. Lias, S. G. NIST Chemistry WebBook; *NIST Standard Reference Database Number 69*; National Institute of Standards and Technology: Gaithersburg, MD.

122. Pilgrim, J. S.; Yeh, C. S.; Berry, K. R.; Duncan, M. A. Photodissociation Spectroscopy of Mg^+–Rare Gas Complexes. *J. Chem. Phys.* **1994**, *100*, 7945–7956.

123. Kreis, C.; Holdener, M.; Génévriez, M.; Merkt, F. High-Resolution Photoelectron Spectroscopy of the Ground and First Excited Electronic States of $MgKr^+$. *Mol. Phys.* **2023**, *121*, e2152746.

124. Reddic, J. E.; Duncan, M. A. Photodissociation Spectroscopy of the Mg^+-Ne Complex. *J. Chem. Phys.* **1999**, *110*, 9948–9955.

125. Willey, K. F.; Yeh, C. S.; Robbins, D. L.; Pilgrim, J. S.; Duncan, M. A. Photodissociation Spectroscopy of Mg^+–H_2O and Mg^+–D_2O. *J. Chem. Phys.* **1992**, *97*, 8886–8895.

126. Willey, K. F.; Yeh, C. S.; Robbins, D. L.; Duncan, M. A. Photodissociation Spectroscopy of Mg^+CO_2. *Chem. Phys. Lett.* **1992**, *192*, 179–184.

127. Reddic, J. E.; Duncan, M. A. Photodissociation Spectroscopy of the Mg^+–C_2H_2 π-Complex. *Chem. Phys. Lett.* **1999**, *312*, 96–100.

128. Robbins, D. L.; Brock, L. R.; Pilgrim, J. S.; Duncan, M. A. Electronic Spectroscopy of the Mg^+–N_2 Complex: Evidence for Photoinduced Activation of N_2. *J. Chem. Phys.* **1995**, *102*, 1481–1492.

129. Chewter, L. A.; Sander, M.; Müller-Dethlefs, K.; Schlag, E. W. High Resolution Zero Kinetic Energy Photoelectron Spectroscopy of Benzene and Determination of the Ionization Potential. *J. Chem. Phys.* **1987**, *86*, 4737–4744.

130. Schröder, D.; Schwarz, H. Ligand Effects as Probes for Mechanistic Aspects of Remote C-H Bond Activation by Iron(I) Cations in the Gas Phase. *J. Organomet. Chem.* **1995**, *504*, 123–135.

131. Colley, J. E.; Dynak, N. J.; Blais, J. R. C.; Duncan, M. A. Photodissociation Spectroscopy and Photofragment Imaging of the Fe^+(Acetylene) Complex. *J. Phys. Chem. A* **2023**, *127*, 1244–1251.

132. Buthelezi, T.; Bellert, D.; Hayes, T.; Brucat, P. J. The Adiabatic Binding Energy of $NbAr^+$. *Chem. Phys. Lett.* **1996**, *262*, 303–307.

133. Lessen, D. E.; Asher, R. L.; Brucat, P. J. Spectroscopically Determined Binding Energies of $CrAr^+$ and $Cr(N_2)^+$. *Chem. Phys. Lett.* **1991**, *177*, 380–382.

134. Marks, J. H.; Kahn, P.; Vasiliu, M.; Dixon, D. A.; Duncan, M. A. Photodissociation and Theory to Investigate Uranium Oxide Cluster Cations. *J. Phys. Chem. A* **2020**, *124*, 1940–1953.

135. Marks, J. H.; Rittgers, B. M.; Van Stipdonk, M. J.; Duncan, M. A. Photodissociation and Infrared Spectroscopy of Uranium–Nitrogen Cation Complexes. *J. Phys. Chem. A* **2021**, *125*, 7278–7288.

CHAPTER 4

ELECTRONIC SPECTROSCOPY OF CARBON CLUSTER CATIONS

Carbon clusters and their cations have been the subject of many studies. They are involved as intermediates of photolysis, electric discharges, and combustion of hydrocarbons.[1,2] They make up fullerenes and have many nanostructures that are relevant to modern material science.[3,4] Carbon clusters are known to be present in the interstellar medium and are expected to have a prevalent role in astrochemistry.[5,6] Carbon molecules are known to have remarkable bonding across many allotropes. Their complexity grows with their size, starting with simple linear chains that eventually form rings before restructuring into cages;[3,4] bulk quantities of carbon form the familiar layered sheets or lattices that can have interesting magnetic properties.[7] The buckminsterfullerene C_{60} provides an example of the noted stability of pure carbon molecules, having a spherical shape and the same sp^2 hybridized bonding as bulk graphite.[8,9] C_{60} and its cation C_{60}^+ have been detected in the diffuse interstellar clouds.[10] Smaller clusters of carbon have also been detected in extraterrestrial environments, including carbon-rich stars, comet trails, and interstellar clouds.[11-14] Carbon has been identified as the fourth-most abundant element in the universe, after hydrogen, helium, and oxygen.[5,6,16-19] Pure carbon molecules do not have a permanent dipole, so they have no microwave spectra to identify in interstellar environments. Instead, amine- and hydrogen-substituted carbon clusters have been identified,[21] substantiating that pure carbon molecules and their cations are present in the interstellar medium and play a role in the chemistry therein. To detect the presence of carbon clusters in the interstellar medium, observations in the infrared, visible, and ultraviolet need to match laboratory

measurements. In 1957, C_2 was identified in stars by its band in the near-infrared at 1200 nm.[11] Soon after, many stars were found to be carbon-rich mostly by observing similar C_2 transitions. C_3 and C_5 were observed in the circumstellar shell of a carbon star.[12,13] Numerous neutral carbon molecules have been identified around many carbon-rich stars and comet trails. Furthermore, large carbon molecules have been identified in comet tails and around carbon stars, taking forms such as diamonds, fullerenes, polyaromatics, and amorphous carbon. In the interstellar medium, protonated carbon clusters have been detected, so it is likely that pure carbon cations also exist in illuminated by UV radiation; however, they are much more difficult to identify due to the lack of laboratory gas phase measurements. There are many absorption bands observed from the interstellar medium, but most bands in these regions still have no identified carrier molecules or ions due to the spectral congestion; these absorption bands are called the Unassigned Infrared bands (UIRs) and the Diffuse Interstellar Bands (DIBs). Observations at and above UV frequencies observe an extinction curve caused by scattering, where the wavelength of light becomes similar to the size of particles of the medium. However, along this extinction curve is a bump at 217.5 nm, which arises from absorption rather than scattering. The molecules or ions causing this spectral feature are also unknown, but because cations of pure carbon have a multitude of low-lying excited electronic states, it is thought that they may cause or contribute to the 217.5 nm bump.[21-27]

The number of electronic states also provides a challenge for theory, requiring a multireference treatment; because of this, previous theoretical results are often conflicting. The spectroscopy of carbon cluster cations in the gas phase is necessary as a benchmark. Laboratory spectroscopic measurements of carbon cluster cations in the gas phase are necessary to confirm if they contribute to the UIRs, DIBs, and the extinction curve's absorption feature.

Carbon clusters can be created with many different techniques: (a) shock-induced decomposition of liquid benzene,[28] (b) during photodissociation of acetylene at 193 nm,[29] (c) IR multiphoton dissociation of ethylene,[30] (d) a helium + acetylene diffusion flame,[31] and (e) an organic halide-alkali metal flame.[32] More recently, carbon clusters have been produced by laser-ablating graphite in a helium expansion, after which ions produced are studied with mass spectrometry.[33] In this way, fullerenes were discovered.[8] Mass spectrometry was used to investigate structural information of carbon clusters,[33-39] such as the fact that even-numbered cluster sizes C_n^+, n = 40 – 70, were observed to be more stable than the odd-numbered sizes. The relative abundance of smaller cluster sizes (n = 6 – 30) is dependent on the vaporization laser, where multiphoton vaporization (e.g., 3.5 eV) would often cause fragmentation of clusters after vaporization, yielding a higher abundance of C_{4n-1}^+ clusters. When a higher photon energy is used for vaporization (e.g., 11 eV), even-numbered carbon clusters are more abundant. Meanwhile, even-numbered carbon cluster *anions* are found to be more stable throughout. Vapors of graphite at 2000–3000 K were found to be comprised of mostly C_3, then C_2 and C, further supporting the ease of C_3 fragmentation.[1] These clusters have exothermic growth, where the binding of additional carbon has a large barrier that leaves the cluster with excess internal energy. Their elevated internal temperature can lead to broad spectra and multiple isomers present despite attempts to cool these clusters. Ion mobility studies were able to observe the arrival times of size-selected carbon cluster cations and found linear structures for clusters C_n^+, n > 11, monocyclic structures between 7 < n < 40, and bicycles and/or 3D for n > 20.[40]

Spectroscopy of pure carbon molecules was measured by Herzberg in 1942[12] and later assigned by Douglas in 1951.[42] Since then, they have been the subject of much research, making C_2 and C_3 some of the most well-characterized molecules.[43] Rare gas matrix isolation infrared

and electronic spectroscopy have been measured for small carbon clusters[1,2,18,44-47] and for C_{60}^+.[9] Because the matrix affects the absorption spectrum measured, it is desirable to study these clusters in the gas phase. However, while the density of neutral carbon molecules allows absorption measurements in the gas phase, cold carbon cations and anions have much less density and are more difficult to study. Cryogenic ion trapping techniques have been used to mass-select and cool carbon cluster ions enough for inert-gas tagging, allowing spectroscopy via photodissociation.[48] In such an instrument, Campbell and Maier were able to trap C_{60}^+-He_n and measure the effect of tagging.[10] Photodissociation spectroscopy has been measured for several small carbon cation clusters. For example, C_5^+ was assigned to have a linear structure.[49] The electronic spectra for C_{2n}^+, n = 6 – 14, were measured by photofragmentation and elimination of a N_2 tag in an ion trap.[50,51] Photofragmentation is an ideal technique to measure the spectra of carbon cluster cations, but high binding energies for most of these small clusters limit the technique to the UV, where tunable lasers are less available. Recent work in the Duncan lab has focused on small carbon cluster cations, investigated with photodissociation[52] and photofragment imaging.[53]

Carbon clusters have been the subject of much computational chemistry.[54-56] Theoretical studies of small carbon molecules determined that cluster sizes smaller than C_{10} have linear structures, while $C_{4,6,8}$ have a stable cyclic conformation. Cluster sizes C_n, n = 10 – 20 were calculated to have cyclic structures more stable than linear structures, but experimental work finds only linear structures for n = 11, 13, and 15.[1] Theory on neutral and anionic carbon clusters has recently moved toward larger structures, such as nanotubes,[57] but for cations, the open-shell electron configuration leads to conflicting results depending on the method of theory used.

Further discussion is available in Reference 1, and relevant examples will be provided later in the chapter.

RESULTS AND DISCUSSION

Mass spectra of carbon cluster cations have been made for decades. Figure 2.3 in Chapter 2 presents the mass spectrum of carbon clusters produced by this lab. The cluster sizes, C_n, follow a pattern of 4n+2 and 4n+3 of higher abundance than the 4n and 4n+1 peaks. As mentioned previously,[1] these magic numbers are only present in mass spectra of cations using multiphoton ionization, where fragmentation occurs during the ionization.

Figure 4.1 presents the photodissociation difference mass spectra for cluster sizes relevant to the study. These clusters eliminate neutral C_3 as the most significant fragment, which is likely due to its stability and higher ionization energy.[1,33] Other fragments include the loss of C_2 and C_5 neutrals, which have previously been reported.[1,33-37] Photofragmentation depends greatly on the laser power and is only detected when the laser energy is very high (above 15 mJ/pulse), which signifies multiphoton absorption. The laser power dependence of the photofragmentation of C_{15}^+ is shown in Figure 4.2. A non-linear power dependence is observed, supporting the multiphoton process.

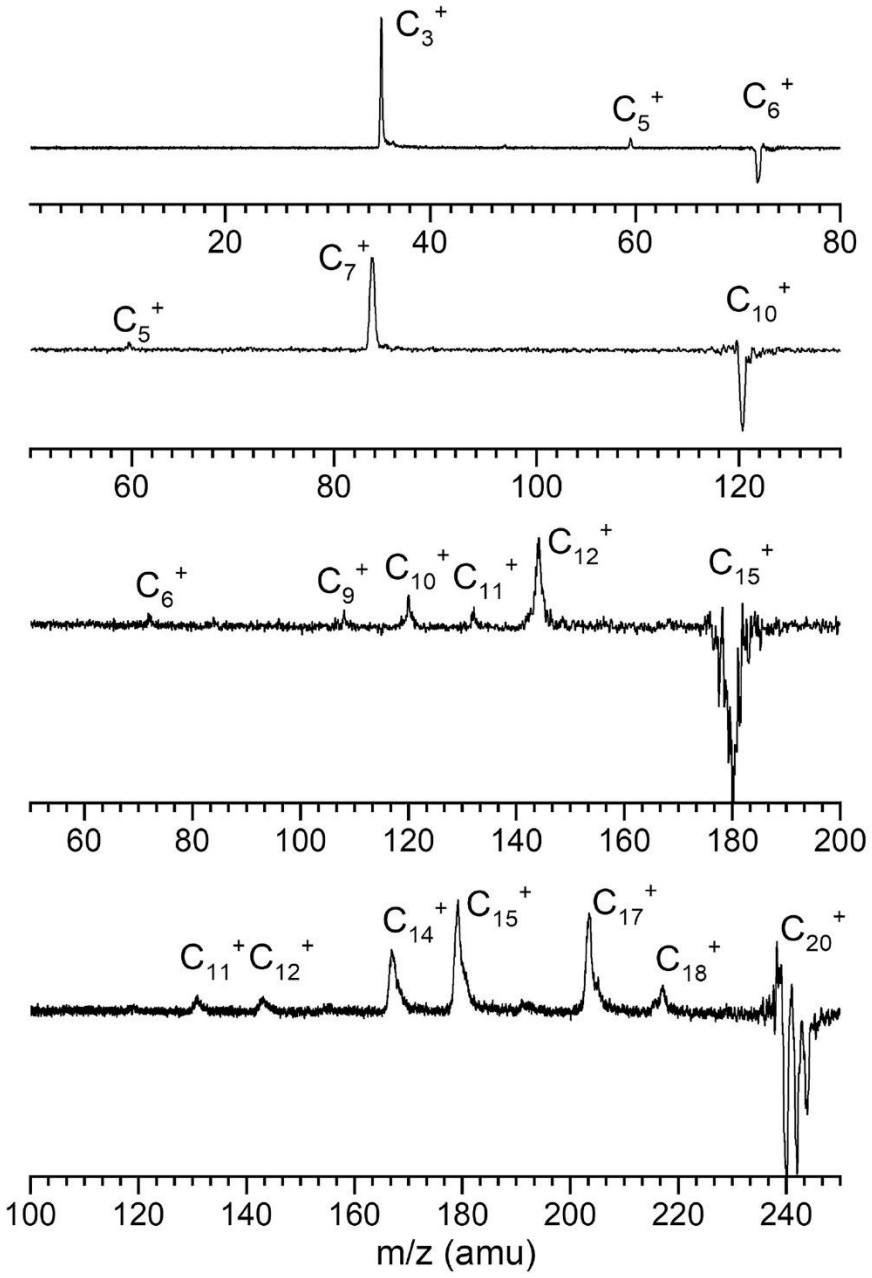

Figure 4.1. Photodissociation difference mass spectra of various carbon cluster sizes.

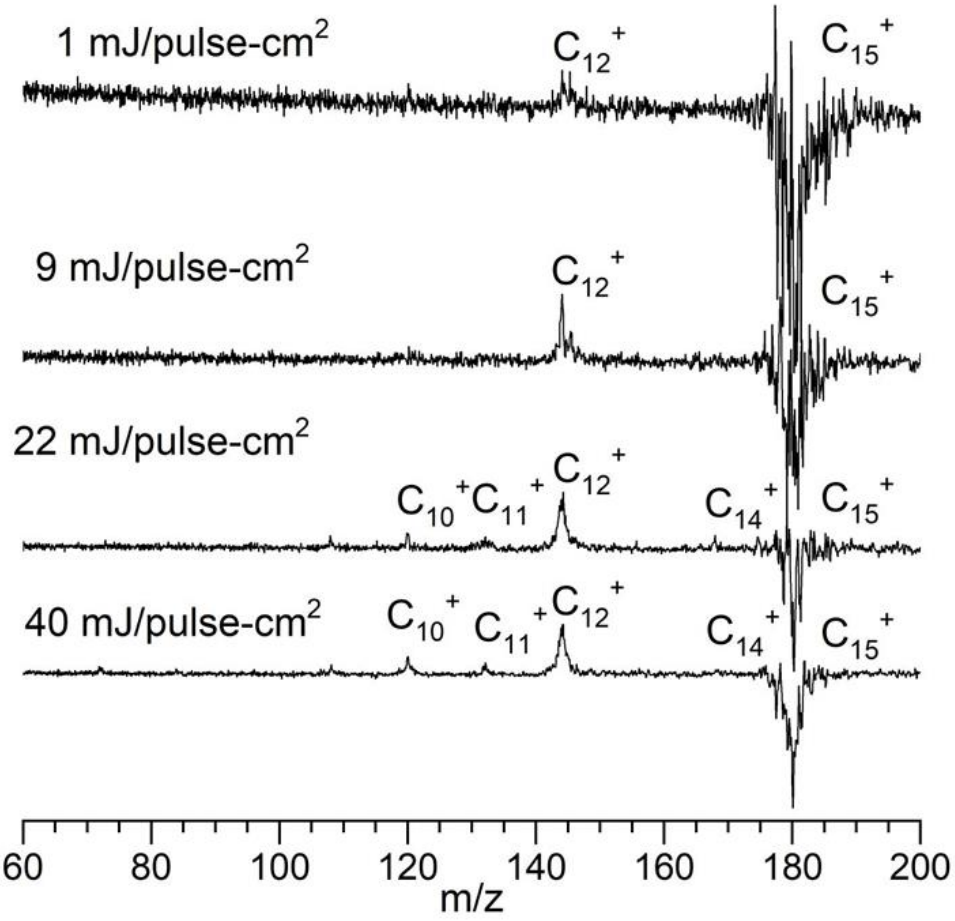

Figure 4.2. The photofragmentation yield of C_{15}^+ at various laser powers at 355 nm.

Theory was used to calculate the thermochemistry of carbon clusters cations, C_n^+, n = 4 – 20, using B3LYP at the Def2-TZVP level, which is shown in Table 4.1. The energy of each structure is zero-point corrected, and the relative energy of the linear structure compared to the cyclic is shown. For C_n^+, n > 7, linear structures were calculated to be more stable, whereas for n < 6, the cyclic structure is predicted to be lower in energy. These calculated values are shown compared to values determined by collision-induced dissociation,[59] which are the only bond dissociation energies determined experimentally. There is considerably more energy calculated to fragment the cyclic isomers due to the necessity of another bond breaking.

Table 4.1. Energetics computed for carbon cluster cations at the DFT/B3LYP/Def2-TZVP level. Calculated bond dissociation energies (BDE) are compared to values determined by collision induced dissociation from Reference 59 for the loss of C_3. The bond dissociation energy was not experimentally determined for C_{20}^+, so the calculated BDEs for the loss of C_3 and C_5 are shown.

	Sum of Electronic and Zero-point Energy		Relative energy		BDE (eV)		
	(Hartrees)		(kcal/mol)		$C_n^+ \rightarrow C_{n-3}^+ + C_3$		
n	Linear	Cyclic	Linear	Cyclic	Linear	Cyclic	Ref. 59
4	-151.72587	-151.713434	0	7.8092375	------	------	
5	-189.8627	-189.728818	0	84.010955	------	------	
6	-227.94959	-227.935163	0	9.05859	6.342	6.084	5.2
7	-266.05915	-266.084942	16.180087	0	6.876	7.577	6.0
8	-304.15704	-304.157493	0.2817475	0	5.816	5.828	5.0
9	-342.26063	-342.265822	3.256725	0	6.270	6.411	6.2
10	-380.35601	-380.425507	43.604347	0	5.885	7.775	6.2
11	-418.45567	-418.536549	50.74969	0	5.933	8.133	7.6
12	-456.54973	-456.613423	39.96673	0	5.673	7.407	6.8
13	-494.64722	-494.70885	38.667177	0	5.731	7.408	5.2
14	-532.73995	-532.847388	67.412325	0	5.542	8.466	5.8
15	-570.83609	-570.946265	69.13042	0	5.599	8.597	6.2
17	-647.02296	-647.117293	59.192702	0	5.508	8.074	5.6
20	-761.29874	-761.416201	73.70615	0	5.311	8.507	Loss of C_3
					5.595	8.791	Loss of C_5

Carbon clusters were previously investigated using photofragment imaging, as detailed in Reference 53. Photofragment imaging can be used to determine the bond dissociation energy for complexes, but it was shown that carbon clusters explode apart with much excess energy. While bond dissociation energies were not able to be determined, it was found that the multiphoton photofragmentation process for carbon clusters is very efficient.

Figure 4.3 presents the photodissociation spectrum of C_6^+, measuring the photofragmentation product C_3. A strong peak is observed at 23,994 cm^{-1} (416.8 nm), which is assigned to be the origin band. Its linewidth is 25 cm^{-1}, which may arise from predissociation and/or the rotational contour and is much wider than the linewidth of the laser (7 cm^{-1}). Two peaks lie higher in energy at 25,244 and 25,647 cm^{-1}. They may originate from vibronic excitations, where the cluster is excited vibrationally as well as electronically. The photodissociation laser used is an OPO, where the laser switches which frequencies are mixed at 25,000 cm^{-1}. Four bands lie to the red of the origin, at 21,290; 21,952; 22,322; and 22,606 cm^{-1}. These bands may represent electronic excitations from excited vibrational states, where the expansion does not sufficiently cool the clusters. Unfortunately, variations in conditions to better cool the clusters produced were unsuccessful, wherein not enough C_6^+ ions were produced to study. These four bands may also represent separate electronic transitions, but the spacing between them and the origin fit well with vibrational frequencies. As the origin band is more intense than these four peaks, the excited state likely has a structure similar to that of the ground state. There is also a broad feature underlying the four lower-energy bands, spanning from 20,500 to 23,000 cm^{-1}. This may be another electronic transition in the same region; the broad structure of the band may come from a repulsive upper state. Another feature of the spectrum is the weak band 79 cm^{-1} above the assigned origin band. This difference is feasible for the spin-orbit splitting for a $^2\Pi_u \rightarrow {}^2\Pi_g$ transition; if the clusters are cooled sufficiently, only the lower $^2\Pi_{1/2}$ level would be populated, giving two transitions into the excited $^2\Pi_{1/2}$ and $^2\Pi_{3/2}$ states. Should this be the case, the intensity of this satellite band should be comparable to the origin band, but the output of the OPO in this region is steeply declining. Furthermore, this same splitting would be seen for the hot bands as well, which is not observed. Likely, this satellite

peak is a sequence band of the origin. The bands detected may still be excitations into a $^2\Pi$ state with a smaller spin-orbit splitting than the laser can resolve.

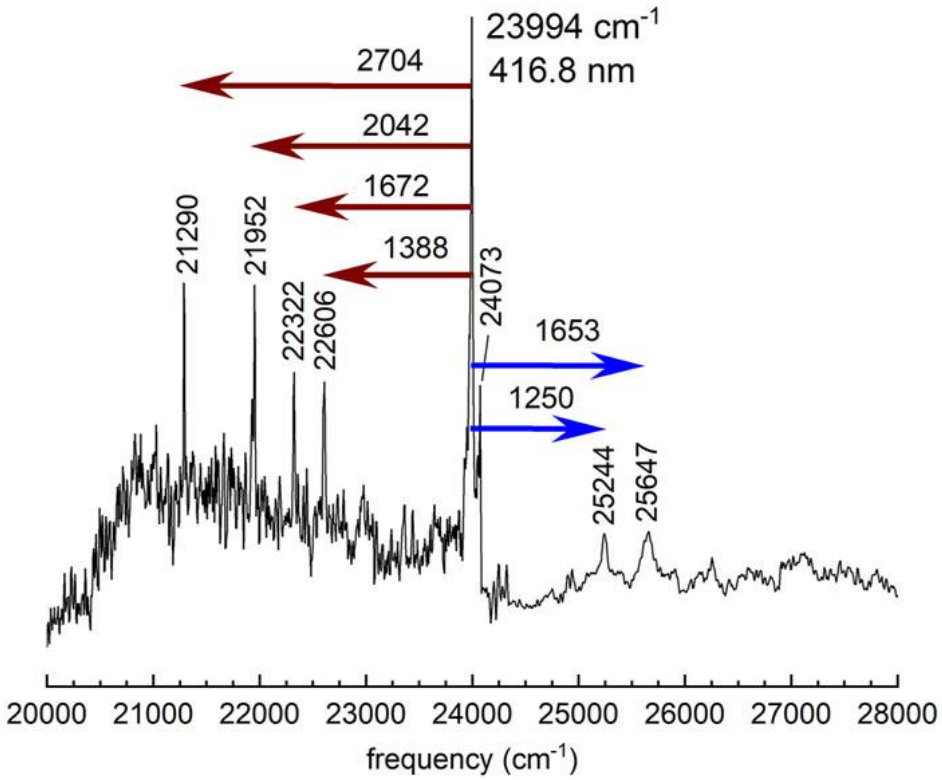

Figure 4.3. Resonance-enhanced photodissociation spectrum of C_6^+ measuring the C_3^+ fragment ion.

The lower energy bands of the spectrum are likely vibrational hot bands. To understand this better, Figure 4.4 shows the same spectrum in reverse from 24,000 to 21,000 (the center of the origin is zero on the x-axis) along with predicted frequencies by DFT for vibrations in a linear and cyclic structure. The computed frequencies are unscaled, harmonic values. Symmetric vibrations that do not change the symmetry of the wavefunction are usually active in an allowed electronic transition, which would be the σ_g modes for a linear structure and the a_1 modes for the cyclic structure. These symmetric vibrations are blue or magenta in the figure. There are many low-frequency vibrations predicted for each isomer, but no bands are detected in the

photodissociation spectrum. However, that is to be expected: collisional energy transfer (i.e. cooling) in an expansion is more efficient for lower energy vibrations.[60] The highest vibration for each structure is 2,186 cm^{-1} in a linear structure and 1,806 cm^{-1} for a cyclic isomer, so the highest-energy band measured would have to correspond to a combination or overtone band. Understandably, the theory does not perfectly predict the vibrations observed in the spectrum. However, the number of high-frequency vibrations and their positions in the linear structure provide a better fit.

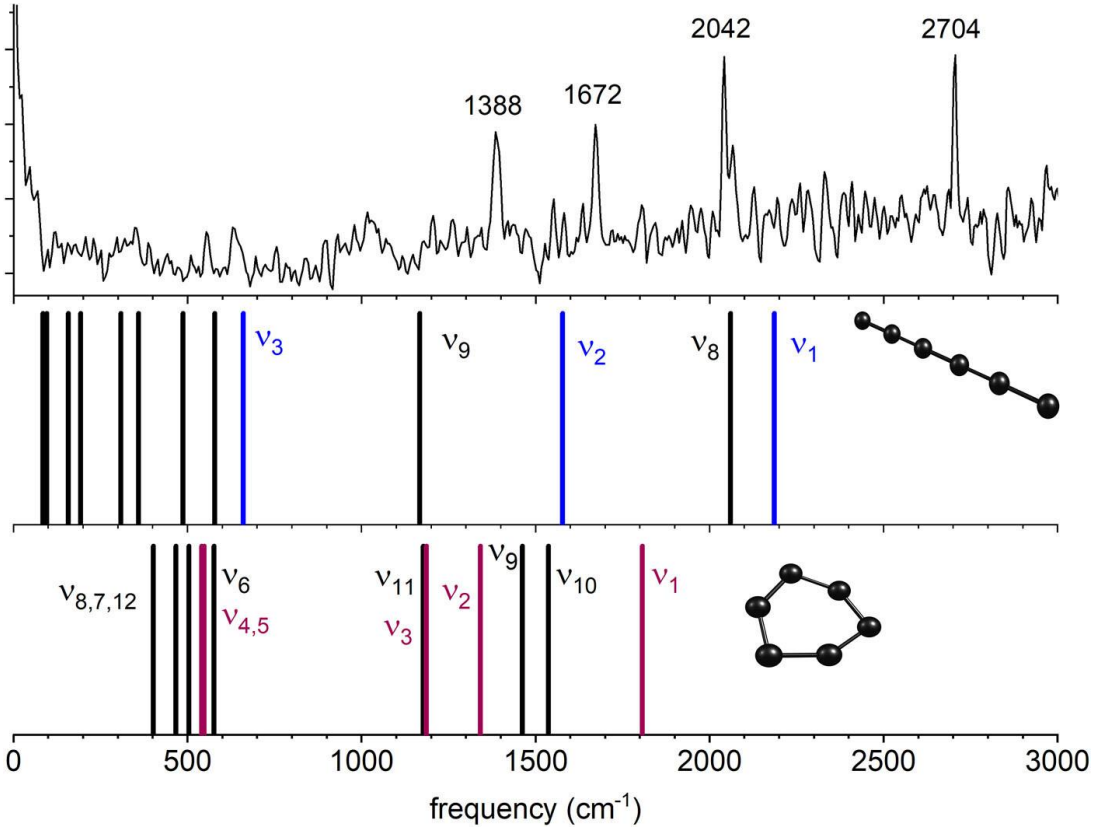

Figure 4.4. The comparison of the assigned hot bands to the vibrational frequencies predicted by DFT for linear vs cyclic structures. The σ_g vibrations for the linear structure and the a_1 vibrations for the cyclic structure are most likely to be Franck–Condon active in an electronic transition; these bands are colored blue in the middle trace and magenta in the bottom trace.

This spectrum is not the first measurement of the spectroscopy of C_6^+: Fulara et al.[46] measured the spectrum of isolated C_6^+ in a matrix of neon. They observed two lines at 15,485 and 17,556 cm^{-1} (645.8 and 569.6 nm), which they assign to the linear and cyclic structures,

respectively. There has been much theoretical work trying to match the bands measured in the Fulara study.[46,54,56,61-63] Both the linear and cyclic isomers are predicted to form, with the cyclic structure calculated to be more stable by about 8 kcal/mol.[61] Campbell and Dunk were able to cryogenically trap C_6^+ and study its spectrum by photodissociation via elimination of a helium tag; however, they only observed a very weak band near 646 nm assigned to the linear structure. Previous ion mobility measurements by Bowers and coworkers found only the linear structure for C_6^+ produced via laser vaporization.[40] These spectra of C_6^+ are trapped in a matrix or tagged with helium, which will have an unknown effect on the spectrum measured. A previous student of the Duncan lab used two-color laser photodissociation measurements of gas-phase C_6^+ and was able to observe two very weak bands at 15,430 and 15,800 cm^{-1} (648 and 633 nm, respectively).[64] These values lie close to the positions of the matrix bands that Fulara assigned to a linear structure, but little else can be gleaned from the spectrum. With a bond dissociation energy of 5.2 eV (as measured by collision-induced dissociation), the low-energy photon will make photofragmentation inefficient. No other study detected any transitions at higher energy. The spectrum shown in Figure 4.3 has only baseline at energies below 20,000 cm^{-1}.

Besides our calculations, the electronic transitions of C_6^+ have been studied with methods suited for multi-reference methods: Haubrich *et al.* using MRD-CI[62] and Gillery *et al.* using CASSCF.[63] Both studies found the ground state to be the $^2\Pi_u$ state for the linear structure and the $^2A_1$ state for the cyclic. Their predicted vertical excitation energies are presented in Table 4.2. The predicted electronic spectra of these two theoretical studies, Ticknor's measured two-color photodissociation spectrum,[64] and the presented photodissociation and predicted spectra are shown together in Figure 4.5. Dashed lines indicate the absorption bands seen in the matrix isolation study by Fulara *et al.*[46]

Table 4.2. Predicted vertical excitation energies and intensities of transitions of linear C_6^+ originating in the $^2\Pi_u$ ground state.

Theoretical Method	**Excited state**	**Vertical excitation energy, eV (cm^{-1})**	**Intensity**	**Source**
MRD-CI	$^2\Sigma_g^+$	1.45 (11 695)	0.001[a]	Haubrich *et al.*[62]
	$^2\Sigma_g^-$	1.46 (11 776)	0.003[a]	
	$^2\Pi_g$	2.31 (18 631)	0.0001[a]	
	$^2\Pi_g$	2.57 (20 728)	0.01[a]	
	$^2\Pi_g$	2.68 (23 195)	0.0003[a]	
	$^2\Pi_g$	2.94 (23 713)	0.008[a]	
	$^2\Sigma_u^-$	3.25 (26 213)	0.003[a]	
CASSCF	$^2\Sigma_g^-$	1.72 (13 873)	0.4779[b]	Gillery *et al.*[63]
	$^2\Pi_g$	2.11 (17 018)	0.6147[b]	
	$^2\Pi_g$	2.58 (20 809)	0.8326[b]	
	$^2\Pi_g$	2.70 (21 777)	1.2918[b]	
	$^2\Sigma_g^-$	3.25 (26 213)	0.3533[b]	
B3LYP/def2-TZVp	$^2\Pi_g$	1.41 (11 372)	0.0001[a]	This work.
	$^2\Delta_g$	1.60 (12 905)	0.0023[a]	
	$^2\Sigma_g^+$	1.86 (15 002)	0.0042[a]	
	$^2\Pi_g$	2.65 (21 374)	0.0092[a]	
	$^2\Sigma_g^-$	3.83 (30 891)	0.0034[a]	
Experiment	$^2\Pi_g$	1.91 (15 430)		Fulara *et al.*[44]
				and Ticknor *et al.*[64]
	$^2\Pi_g$	2.97 (23 994)		This work.

[a] Oscillator strength.
[b] Transition dipole moment in Debye.

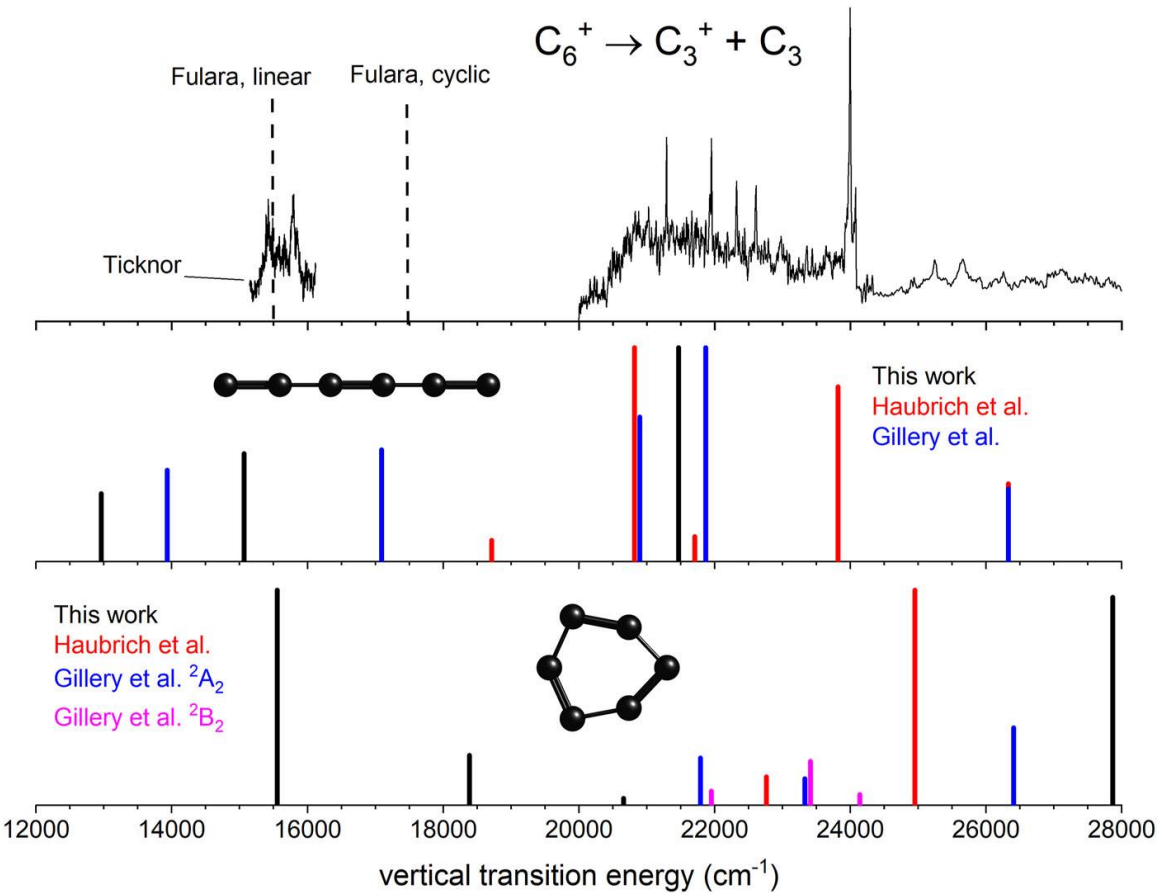

Figure 4.5. Comparison of the electronic transition measured for C_6^+ near 417 nm and that detected near 648 nm to the predictions of different theoretical methods for linear and cyclic isomers.

As seen in Figure 4.5, no theoretical method accurately describes the two measured electronic spectra. The work by Haubrich *et al.* predicted three bands near the blue spectrum at 20,728; 23,713; and 26,213 cm^{-1}. The predicted transition at 23,713 cm^{-1} is almost exactly where the origin transition at 23,995 cm^{-1} is, and it predicts a transition near the broad band observed from 20,500 to 23,000 cm^{-1}. However, neither their work on the linear nor the cyclic isomers predicts anything near the red spectrum measured by Ticknor or in matrix isolation work by Fulara *et al.* The spectrum predicted by Gillery *et al.* for the linear isomer has two bands near the observed doublet near 16,000 cm^{-1}, but there are no transitions predicted near the observed matrix isolation absorption for the cyclic isomer near 15,500 cm^{-1}. Finally, the DFT

computations carried out by our lab predict a band in the vicinity of the blue band (though it differs by 2,500 cm^{-1}), two bands in the red for linear structure, and one band in the red for the cyclic isomer. Overall, all three methods predict strong transitions near where they were observed experimentally for the linear structure, which provides strong evidence for linear C_6^+. The observed transition at 23,995 cm^{-1} can then be assigned the $X^2\Pi_u \rightarrow {}^2\Pi_g$ transition. While no method accurately predicts the spectrum, only TD-DFT correctly predicts transitions in the lower energy region, where Ticknor and Fulara *et al.* observed bands.

The photodissociation spectrum measured herein could be improved. For instance, because the photon energy of the photodissociation laser is not above the calculated bond dissociation energy (see Table 4.1), the photodissociation process relies on multiple photons; this may attenuate or amplify some of the bands seen in the spectrum. An attempt was made to address this, laser conditions were varied: two-color experiments were conducted using the tuned OPO together with 355 or 266 nm from a Nd:YAG laser, but no new bands were detected. Conditions were altered in an attempt to tag C_6^+ with a rare gas, but the ion signal for the tagged clusters was insufficient for photodissociation. Argon was used to create an expansion gas that would more efficiently cool the ions produced, but instead, only larger ions (e.g. C_n^+, n = 15 – 30) were produced.

When such experiments failed to further our understanding of the visible electronic spectrum of C_6^+, our next experiment was chosen to preempt these same complications: optimizing conditions for a colder expansion produced more carbon clusters, C_n^+, in the size range n = 11 – 20, so the next experiment would be on such ions. Furthermore, by using higher-energy photons, a single-photon process can be used for photodissociation. Figure 4.6 shows the

predicted electronic transitions for C_n^+, n = 10 – 20. As seen, each cluster size should have prominent bands in the UV.

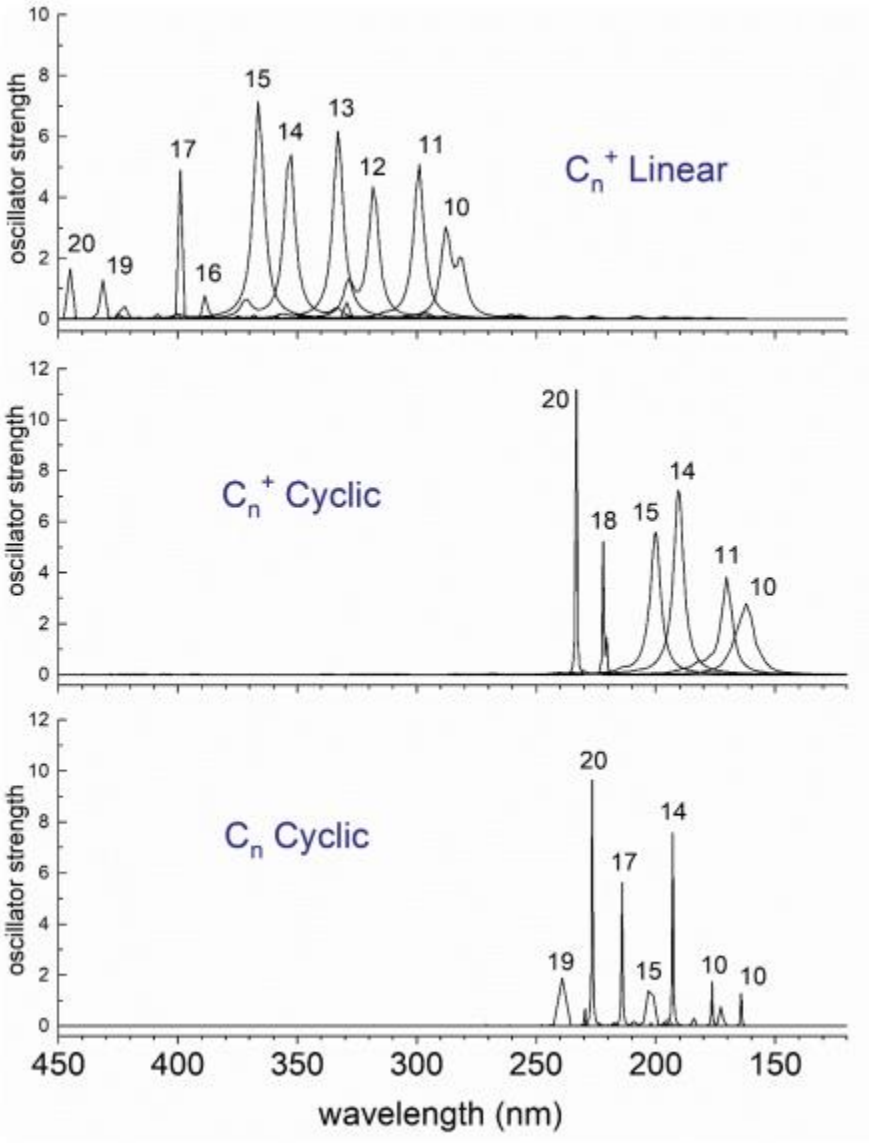

Figure 4.6. Predicted vertical transitions for C_n^+, n = 10 – 20 at the DFT/B3LYP/Def2-TZVP level.

Unfortunately, while the OPO system used for photodissociation provides tunable light throughout the visible and UV regions, the laser system has widely varying power not suited to broad scans through the deep UV. Figure 4.7 presents the photodissociation spectra for carbon clusters, C_n^+, n = 13 – 20. Each spectrum measures the wavelength dependence of multiple

photofragment products (usually the loss of C_2 and C_3), though there is no difference between the photodissociation spectrum of each product for a cluster size. There are broad bands seen around 350 and 260 nm in most spectra, but these wavelengths are in the middle of the crystal curves where the OPO performs especially well. When correcting for power, the bands observed can become noisy baseline instead; such is the case for the spectrum measured for C_{14}^+. However, there are some spectra that have features despite the inconsistent power.

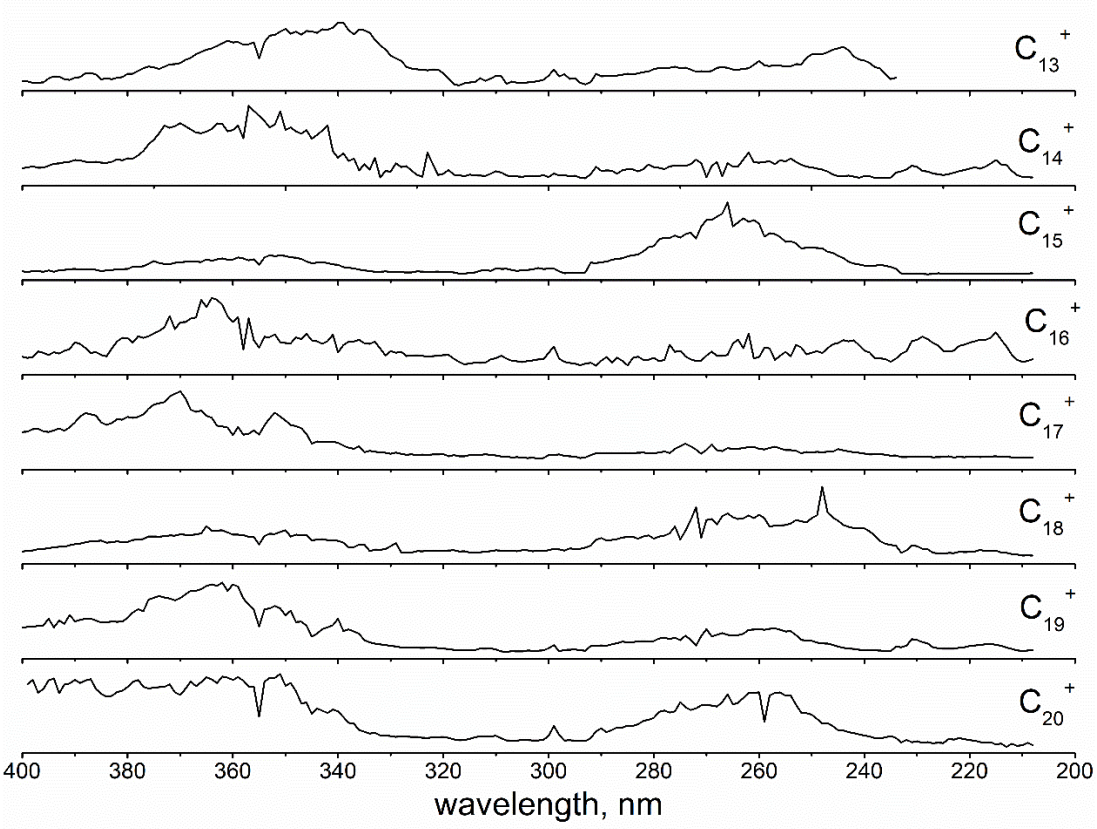

Figure 4.7. Measured photodissociation spectra for carbon clusters C_n^+, $12 < n < 21$. Spectra closely resemble the output power of the Horizon OPO in the UV.

Figures 4.8 and 4.9 present the photodissociation spectra of C_{15}^+ and C_{20}^+, respectively, after correcting for power. The photodissociation spectrum measured for C_{15}^+ measures the loss of C_3 and C_5. There is a broad peak centered at 270 nm, but the spectrum has been corrected for laser power, so this peak is not an artifact of laser power. This is also the case for the

photodissociation spectrum of C_{20}^+, where the loss of C, C_3, C_4, and C_5 are measured. For C_{20}^+, a gradual rise in photofragmentation yield is observed continuing into the visible region. While there is merit to measuring the photodissociation spectra for the rest of the carbon cluster sizes, the spectra collected so far are broad and difficult to understand. To improve on this, the experiment is being altered in hopes of learning more about carbon clusters. Specifically, the reflectron has been modified to include a fluorescence viewport and a photomultiplier detector. With this detector, should the mass-selected ion absorb light from the photodissociation laser and fluoresce, it would be recorded. Carbon clusters are expected to have efficient fluorescence at red wavelengths, but this experiment should be possible for any ion that can be produced efficiently and that fluoresces strongly.

Another possible study is a double resonance photodissociation experiment, where the photodissociation of a cluster size could be depleted by the transfer of population out of the ground state preceding the photodissociation laser firing. If the population in the excited state does not absorb the second photon (or if the absorption cross-sections are significantly different), a loss in photodissociation can be measured. This experiment will allow the spectroscopy of carbon clusters below the dissociation energy to be measured. For example, with a double resonance experiment, it may be possible to measure the photodissociation of C_6^+ at red wavelengths where absorption was detected previously.[46,64]

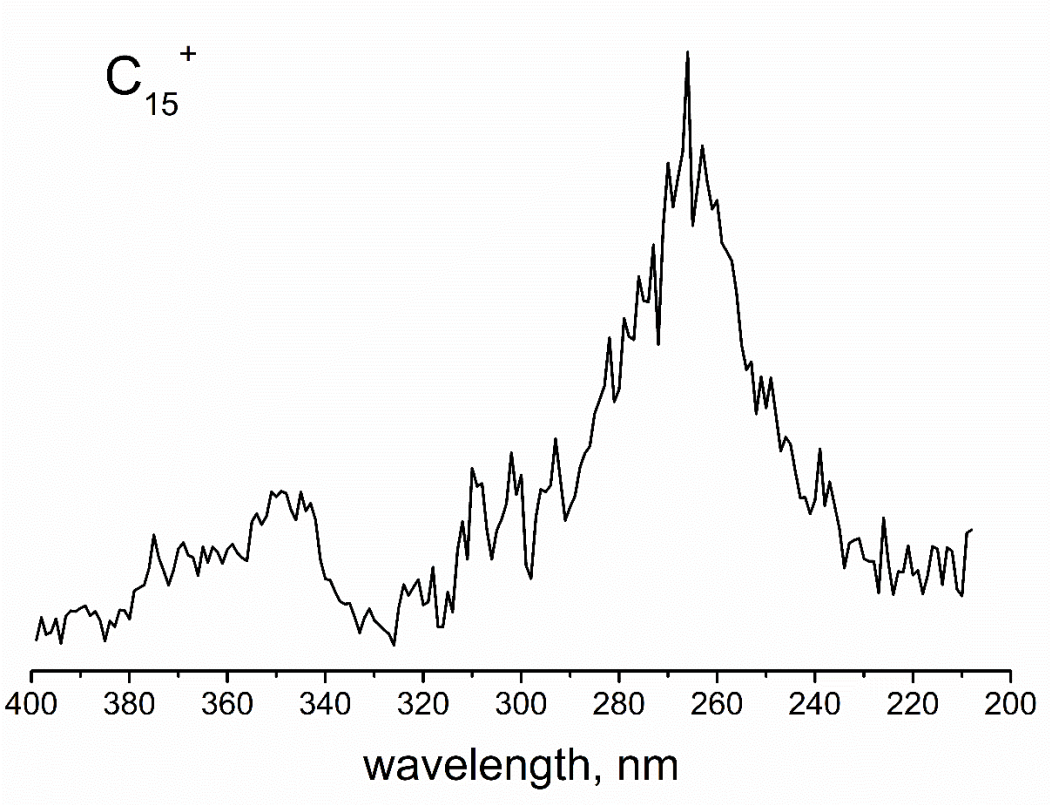

Figure 4.8. Power-corrected photodissociation spectra for C_{15}^+ measuring the appearance of C_{12}^+ and C_{10}^+.

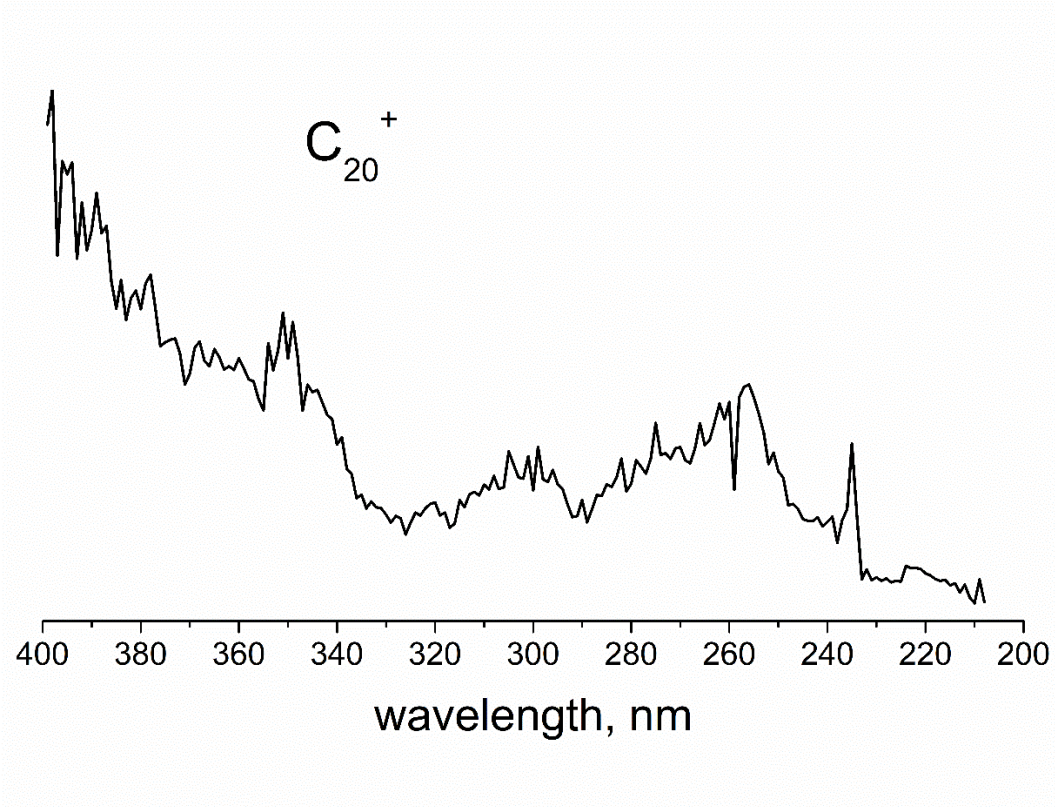

Figure 4.9. Power-corrected photodissociation spectra for C_{20}^+ measuring the appearance of C_{19}^+, C_{17}^+, C_{16}^+, and C_{15}^+.

CONCLUSIONS

Small carbon cluster cations are important targets for laboratory spectroscopy. Knowledge of their spectra will lead to further information on the chemistry of the interstellar medium and the possible growth of larger carbon allotropes and organic molecules. The exothermic growth of these clusters makes them challenging for laboratory measurements of a cold spectrum, and the strong multireference characteristic is difficult for theory to describe. The resonance-enhanced multiphoton photodissociation spectrum of C_6^+ is presented here. The transition measured at 23,993 cm^{-1} was assigned as the origin of the $X^2\Pi_u \rightarrow {}^2\Pi_g$ excitation of the linear isomer. Vibronic bands and vibrational hot bands were also measured which supports

the linear assignment. Experimental data was compared to theory to make this assignment. It was found that while no theoretical method accurately predicted the spectrum, B3LYP outperformed CASSCF and MRD-CI. Other small clusters can be measured in this way, but in order to ensure that clusters are more efficiently cooled, carbon cluster C_n^+, $10 < n < 20$ are the targets for further study. However, the photodissociation of carbon clusters in the UV is very susceptible to inconsistencies in the OPO output power. The instrument is, at the time of writing this, being modified to allow for the detection of fluorescence of mass-selected ions in the turning region of the reflectron. With such alterations, the laser induced fluorescence (LIF) of an ion can be measured. Carbon clusters are a prime target for LIF spectroscopy. These clusters remain an important focus for laboratory spectroscopy, and every spectrum measured is another step toward understanding the chemistry of the interstellar medium.

REFERENCES

1. Van Orden, A.; Saykally R. J. Small Carbon Clusters: Spectroscopy, Structure, and Energetics. *Chem. Rev.* **1998**, *98*, 2313-2358.
2. Weltner Jr., W.; Van Zee, R. J. Carbon Molecules, Ions, and Clusters. *Chem. Rev*. **1989**, *89*, 1713-1747.
3. Lifshitz, C. Carbon Clusters. *Int. J. Mass Spectrom*. **2000**, *200*, 423-442.
4. Dresselhaus, M. S.; Dresselhaus, G.; Eklund, P. C. *Science of Fullerenes and Carbon Nanotubes*, Academic Press, San Diego, 1996.
5. Hartquist, T. W.; Williams, D. A. *The Molecular Astrophysics of Stars and Galaxies*; International Series on Astronomy and Astrophysics; Oxford University Press: Oxford, New York, 1999.
6. Kirkwood, D. A.; Linnartz, H.; Grutter, M.; Dopfer, O.; Motylewski, C.-T.; Pachkov, M.; Tulej, M.; And, M. W.; Maier, J. P. Electronic Spectroscopy of Carbon Chains and Relevance to Astrophysics. *Faraday Discuss.* **1998**, *109*, 109–119.
7. Afshar, M.; Babaei, M.; Kordbacheh, A. H. First Principles Study on Structural and Magnetic Properties of Small and Pure Carbon Clusters (C_n, n = 2 – 12). *J. Theor. Appl. Phys.* **2014**, *8*, 103–108.
8. Kroto, H. W.; Heath, J. R.; O'Brien, S. C.; Curl, R. F.; Smalley, R. E. C_{60}: Buckminsterfullerene. *Nature* **1985**, *318*, 162–163.
9. Fulara, J.; Jakobi, M.; Maier, J. P. Electronic and Infrared Spectra of C_{60}^+ and C_{60}^+ in Neon and Argon Matrices. *Chem. Phys. Lett.* **1993**, *211*, 227–234.
10. Campbell, E. K.; Maier, J. P. Perspective: C_{60}^+ and Laboratory Spectroscopy Related to Diffuse Interstellar Bands. *J. Chem. Phys.* **2017**, *146*, 160901.

11. Souza, S. P.; Lutz, B. L. Detection of C_2 in the Interstellar Spectrum of Cygnus OB2 Number 12 (VI Cygni number 12). *Astrophys. J. Lett.* **1977**, *216*, L49-L51.

12. Hinkle, K. W.; Keady, J. J.; Bernath, P. F. Detection of C_3 in the Circumstellar Shell of IRC+10216. *Science* **1988**, *241*, 1319–1322.

13. Bernath, P. F.; Hinkle, K. H.; Keady, J. J. Detection of C_5 in the Circumstellar Shell of IRC+10216. *Science* **1989**, *244*, 562–564.

14. Maier, J. P.; Lakin, N. M.; Walker, G. A. H.; Bohlender, D. A. Detection of C_3 in Diffuse Interstellar Clouds. *Astrophys. J.* **2001**, *553*, 267.

15. *The Diffuse Interstellar Bands*, 1995th edition.; Tielens, A. G. G. M., Snow, T. P., Eds.; Springer: Dordrecht ; Boston, 1995.

16. *The Molecular Astrophysics of Stars and Galaxies*; Hartquist, E. by T. W., Williams, D. A., Eds.; International Series on Astronomy and Astrophysics; Oxford University Press: Oxford, New York, 1999.

17. Heath, J. R.; Van Orden, A.; Hwang, H. J.; Kuo, E. W.; Tanaka, K.; Saykally, R. J. Toward the Detection of Pure Carbon Clusters in the ISM. *Adv. Space Res.* **1995**, *15*, 25–33.

18. Maier, J. P. Electronic Spectroscopy of Carbon Chains. *J. Phys. Chem. A* **1998**, *102*, 3462–3469.

19. Thaddeus, P.; McCarthy, M. C. Carbon Chains and Rings in the Laboratory and in Space. *Spectochim. Acta, Part A.* **2001**, *57*, 757–774.

20. Maier, J. P.; Walker, G. A. H.; Bohlender, D. A. On the Possible Role of Carbon Chains as Carriers of Diffuse Interstellar Bands. *Astrophys. J.* **2004**, *602*, 286.

21. J. P. Maier, Electronic Spectroscopy of Carbon Chains and Their Relevance to Astrophysics. *In The Dense Interstellar Medium in Galaxies*; Pfalzner, S., Kramer, C., Staubmeier, C., Heithausen, A., Eds.; 2004; Vol. 91.

22. Herbst, E. Chemistry in the Interstellar Medium. *Annu. Rev. Phys. Chem*. **1995**, *46*, 27–54.

23. Brault, J. W.; Testerman, L.; Grevesse, N.; Sauval, A. J.; Delbouille, L.; Roland, G. Infrared Bands of C_2 in the Solar Photospheric Spectrum. *Astron. Astrophys.* **1982**, *108*, 201-205.

24. Draine, B. T.; Malhotra, S. On Graphite and the 2175 Å Extinction Profile. *Astrophys. J.* **1993**, *414*, 632-645.

25. de Heer, W. A.; Ugarte, D. Carbon Onions Produced by Heat Treatment of Carbon Soot and Their Relation to the 217.5 nm Interstellar Absorption Feature. *Chem. Phys. Lett.* **1993**, *207*, 480–486.

26. Blanco, A.; Fonti, S.; Orofino, V. On the Interstellar Extinction Hump and Laboratory Carbonaceous Grains. *Astrophys. J.* **1996**, *462*, 1020-1025.

27. Fitzpatrick, E. L. Correcting for the Effects of Interstellar Extinction. *Pub. Astron. Soc. Pac.* **1999**, *111*, 63-75.

28. Nicol, M.; Johnson, M. L.; Holmes, N. C. Chemiluminescence of Shock-Pyrolyzed Benzene. *Physica B+C* **1986**, *139*, 582–586.

29. Wodtke, A. M.; Lee, Y. T. Photodissociation of Acetylene at 193.3 nm. *J. Phys. Chem*. **1985**, *89*, 4744–4751.

30. Grunwald, R.; Lademann, J.; Homan, G.; Shibanov, A. N. Generation of Electronically Excited Radicals in the Collisionless Infrared Multiple-Photon Dissociation of Ethylene. *Khim. Fiz.* **1985**, *4*, 46–49.

31. Winicur, D.; Hardwick, J. L. Dynamics of C2($d^3\Pi_g$) Formation in the He* + C_2H_2 Diffusion Flame. *Chem. Phys.* **1985**, 94, 157–166.

32. Curtis, M. C.; Sarre, P. J. High-Resolution Laser Spectroscopy of the Swan System ($d^3\Pi_g$-$a^3\Pi_u$) of C_2 in an Organic Halide-Alkali Metal Flame. *J. Mol. Spectrosc.* **1985**, *114*, 427–435.

33. Lemire, G. W.; Fu, Z.; Hamrick, Y. M.; Taylor, S.; Morse, M. D. New Electronic Band Systems of Jet-Cooled Carbon Trimer: 266-302 nm. *J. Phys. Chem*. **1989**, *93*, 2313–2319.

34. Geusic, M. E.; McIlrath, T. J.; Jarrold, M. F.; Bloomfield, L. A.; Freeman, R. R.; Brown, W. L. Photofragmentation of Mass-Resolved Carbon Cluster Ions: Observation of a ″Magic″ Neutral Fragment. *J. Chem. Phys.* **1986**, *84*, 2421–2422.

35. Geusic, M. E.; Jarrold, M. F.; McIlrath, T. J.; Freeman, R. R.; Brown, W. L. Photodissociation of Carbon Cluster Cations. *J. Chem. Phys.* **1987**, *86*, 3862–3869.

36. O'Brien, S. C.; Heath, J. R.; Curl, R. F.; Smalley, R. E. Photophysics of Buckminsterfullerene and Other Carbon Cluster Ions. *J. Chem. Phys.* **1988**, *88*, 220–230.

37. Sowa, M. B.; Hintz, P. A.; Anderson, S. L. Dissociation Energies for Carbon Cluster Ions ($C^+_{2\text{-}15}$): A System Where Photodissociation Is Misleading. *J. Chem. Phys.* **1991**, *95*, 4719–4720.

38. Bouyer, R.; Roussel, F.; Monchicourt, P.; Perdrix, M.; Pradel, P. Energetics of C_{16}^+ to C_{36}^+ Photodissociation. *J. Chem. Phys.* **1994**, *100*, 8912–8919.

39. Pozniak, B. P.; Dunbar, R. C. Photodissociation Studies of C_n^+ at 193 nm (n = 5−19)1. *Int. J. Mass Spectrom. Ion Processes* **1997**, *165–166*, 299–313.

40. von Helden, G.; Hsu, M. T.; Gotts, N.; Bowers, M. T. Carbon Cluster Cations with up to 84 Atoms: Structures, Formation Mechanism, and Reactivity. *J. Phys. Chem.* **1993**. *97*, 8182–8192.

41. Herzberg, G. *The Spectra and Structures of Simple Free Radicals: An Introduction to Molecular Spectroscopy*, First Edition.; Dover Publications: New York, 2012.

42. Douglas, A. E. Laboratory Studies of the lambda 4050 Group of Cometary Spectra. *Astrophys. J.* **1951**, *114*, 466–468.

43. Rohlfing, E. A. Study of Small Carbon and Silicon Clusters using Negative Ion Photodetachment Techniques. *In Advances in Metal and Semiconductor Clusters: Spectroscopy and Structure*; Duncan, M. A., Ed.; JAI Press: Greenwich, CT, 1995; Vol. 3, pp 85–111.

44. Weltner, W.; Van Zee, R. J. Matrix-Isolated Polycarbon Molecules. *J. Mol. Struct.* **1990**, *222*, 201–207.

45. Vala, M.; Chandrasekhar, T. M.; Szczepanski, J.; Pellow, R. Infrared Spectrum of the Ionic Cyclic C_5^+ Cluster in an Argon Matrix. *J. Mol. Struct.* **1990**, *222*, 209–218.

46. Fulara, J.; Riaplov, E.; Batalov, A.; Shnitko, I.; Maier, J. P. Electronic and Infrared Absorption Spectra of Linear and Cyclic C_6^+ in a Neon Matrix. *J. Chem. Phys.* **2004**, *120*, 7520–7525.

47. Fulara, J.; Shnitko, I.; Batalov, A.; Maier, J. P. Electronic Absorption Spectra of Linear and Cyclic C_n^+ n = 7–9 in a Neon Matrix. *J. Chem. Phys.* **2005**, *123*, 044305.

48. Campbell, E. K.; Dunk, P. W. LV-DIB-s4PT: A New Tool for Astrochemistry. *Rev. Sci. Instrum.* **2019**, *90*, 103101.

49. Reedy, E. S.; Rademacher, J.; Szabla, R.; Campbell, E. K. Electronic Absorptions of C_5^+ Detected in the Visible through Action Spectroscopy in a Cryogenic Trap. *Mol. Phys.* **2022**, *120*, e1989070.

50. Rademacher, J.; Reedy, E. S.; Campbell, E. K. Electronic Spectroscopy of Monocyclic Carbon Ring Cations for Astrochemical Consideration. *J. Phys. Chem. A* **2022**, *126*, 2127–2133.

51. Buntine, J. T.; Cotter, M. I.; Jacovella, U.; Liu, C.; Watkins, P.; Carrascosa, E.; Bull, J. N.; Weston, L.; Muller, G.; Scholz, M. S.; Bieske, E. J. Electronic Spectra of Positively Charged Carbon Clusters—C_{2n}^+ (n = 6–14). *J. Chem. Phys.* **2021**, *155*, 214302.

52. Colley, J. E.; Orr, D. S.; Duncan, M. A. Communication: Electronic Transition of the l–C_6^+ Cation at 417 nm. *J. Chem. Phys.* **2022**, *157*, 121102.

53. Dynak, N. J.; Rittgers, B. M.; Colley, J. E.; Kellar, D. J.; Duncan, M. A. Photofragment Imaging of Carbon Cluster Cations: Explosive Ring Rupture. *J. Phys. Chem. Lett.* **2022**, *13*, 4786–4793.

54. Watts, J. D.; Bartlett, R. J. A Theoretical Study of Linear Carbon Cluster Monoanions, C_n^-, and Dianions, C_{n2}^- (n = 2–10). *J. Chem. Phys.* **1992**, *97*. 3445–3457.

55. Merino, G.; Méndez-Rojas, M. A.; Beltrán, H. I.; Corminboeuf, C.; Heine, T.; Vela, A. Theoretical Analysis of the Smallest Carbon Cluster Containing a Planar Tetracoordinate Carbon. *J. Am. Chem. Soc.* **2004**, *126*, 16160–16169.

56. Kosimov, D. P.; Dzhurakhalov, A. A.; Peeters, F. M. Theoretical Study of the Stable States of Small Carbon Clusters C_n (n = 2 – 10). *Phys. Rev. B* **2008**, *78*, 235433.

57. Kharisov, B. I.; Kharissova, O. V.; González, L. T.; Peña Méndez, Y.; Uflyand, I. E.; Kulkarni., N. Density Function Theory Predicted Carbon Allotropes: Recent Developments. *ChemistrySelect* **2023**, *8*, e202301567.

58. Belau, L.; Wheeler, S. E.; Ticknor, B. W.; Ahmed, M.; Leone, S. R.; Allen, W. D.; Schaefer, H. F.; Duncan, M. A. Ionization Thresholds of Small Carbon Clusters: Tunable VUV Experiments and Theory. *J. Am. Chem. Soc.* **2007**, *129*, 10229–10243.

59. Sowa-Resat, M. B.; Hintz, P. A.; Anderson, S. L. Dissociation Energies for Small Carbon Cluster Ions (C_{2-19}^+) Measured by Collision-Induced Dissociation. *J. Phys. Chem.* **1995**, *99*, 10736-10741.

60. Krajnovich, D. J.; Parmenter, C. S.; Catlett Jr., D. L. State-to-State Vibrational Transfer in Atom-Molecule Collisions. Beams vs Bulbs. *Chem. Rev.* **1987**, *87*, 237−288.

61. Giuffreda, M. G.; Deleuze, M. S.; François, J.-P. Structural, Rotational, Vibrational, and Electronic Properties of Ionized Carbon Clusters C_n^+ (n = 4−19). *J. Phys. Chem. A* **1999**, *103*, 5137–5151.

62. Haubrich, J.; Mühlhäuser, M.; Peyerimhoff, S. D. The Electronic Spectrum of Linear and Cyclic C_6^+. A Theoretical Study. *Phys. Chem. Chem. Phys.* **2002**, *4*, 2891–2896.

63. Gillery, C.; Rosmus, P.; Werner, H.-J.; Stoll, H.; Maier, J. P. A Theoretical Study of the Electronically Excited States in Linear and Cyclic C_6^+. *Mol. Phys.* **2004**, *102*, 2227–2236.

64. B. W. Ticknor, Ph.D. dissertation (University of Georgia, 2008).

APPENDIX

MORE ON THE LABVIEW CODE

LabVIEW is a graphical coding language designed to allow users with little coding experience to interface with scientific instruments. The code file, called a Virtual Instrument (VI), contains objects that the user connects together visually, so it is not necessary to know a coding language. A VI can contain subVIs with input and output terminals. Importantly, instrument manufacturers can provide VIs to implement in larger VI manifolds, which is the case for communication with the Horizon OPO and LeCroy oscilloscope used for data acquisition in the experiments of this dissertation.

This VI was written based on a project written by Travis Jones of the Douberly group to scan a PDL dye laser. As such, much of the code was changed to run with Continuum's Horizon OPO system. Continuum provided a laptop to communicate with the OPO system with corresponding LabVIEW and C++ codes to communicate with that laptop. The LabVIEW code provided is far from perfect, but with the amount of formatting needed for communication, I am hesitant to change it more than cleaning up a few loops. Below is a breakdown of what is done by this code.

This code operates using message queues to communicate between While loops that handle different operations, which in this case are UI, Oscilloscope, PDL (originally used for a dye laser), Acquisition, and Logging. There's an additional loop (Event Handling loop) on top that handles any 'button press' events that do not include the OPO controls. The UI loop handles interface operations, such as opening the settings window or disabling the start button after it has

been toggled. The Oscilloscope loop (not the Oscilloscope Main.vi) interacts with the oscilloscope, such as initializing and updating settings. In the same way, the PDL loop interacts with the laser; in the original code (written for use with a dye laser), this loop also handled conversion from motor position to wavelength and scanning start wavelength, end wavelength, and speed. In this version of the code (written for use with Continuum's Horizon OPO), this loop instead interacts with the laser *only* when moving to the next wavelength step in a scan. The Acquisition loop has been bundled into this PDL loop as well, so Acquiring data from the 'scope happens only when the laser stops at the next step of the scan. Finally, the Logging loop takes the data acquired and streams it into a TDMS file. Message queues take multiple lists of words (divided into the different operations) and feed them into the corresponding loops. If you want to learn more about message queues used in this way, take a look into the Continuous Data Acquisition example VI provided by LabView (which looks a lot like the original code).

The Event Handling loop is fairly straightforward: an event loop activates its contents when the event is tripped. For example, if the settings button is toggled during operation, the event loop inserts 5 new messages into the UI sub-message in the message queue. These messages tell the UI loop to enable/disable some controls, update the status bar (on the front panel), and open the Settings.vi. An event case should exist for all controls except those for the OPO.

The UI Message loop may look similar to the event handler loop above in some windows of the case structure, such as the Start case; messages are enqueued for other loops in the vi. There are some subVIs that appear in the case structure as well; one of which is the Oscilloscope Main.vi (you can open this subVI from the project or by double clicking it as it appears in the

Call By Reference node). The UI Message loop also includes subVIs for settings and the PDL, though that shouldn't be used.

The Oscilloscope loop is easy to understand for the most part. The only case of note is the "Scan" case. This case was added to handle the step-wise acquisition of data: the laser moves to a new wavelength and waits, while the Acquisition.vi averages a number of sweeps before sending a notifier to start logging and move to the next wavelength. There are two For loops in the Acquisition.vi to account for the number of averages wanted by the user and the number of cursors fixed on the Oscilloscope window (which is set on the physical Oscilloscope); the data is sorted into an array of clusters keeping track of the wavelength and peak area. As it stands, there is some fault causing the first few steps to not be logged, but hopefully, that will be fixed by the time you are reading this. If you want to learn more about this VI, check out the Continuous Data Acquisition example VI provided by LabView.

The Logging.vi is essentially a while loop acting in the same capacity as the others above, with the notable addition of an error case: if an error is detected, it will not run the While loop. This VI streams the data from the Acquisition.vi into a TDMS file, which is automatically updated at every data point; if the main VI crashes, the data up to that point will be saved. Again, if you want to learn more about this VI, check out the Continuous Data Acquisition example VI provided by LabView.

The Oscilloscope Main.vi operates when the Oscilloscope button on the main front panel is toggled. This VI handles the oscilloscope settings, including setting cursors for the integration gate channels, calibrating the mass spectrum, and logging said spectrum (different from logging data from the scan on the main VI). Its contents operate in a message queue similar to the main

VI. Artifacts of the original version appear here as well, for if a mass spec is wanted while the laser is set to a specific wavelength.

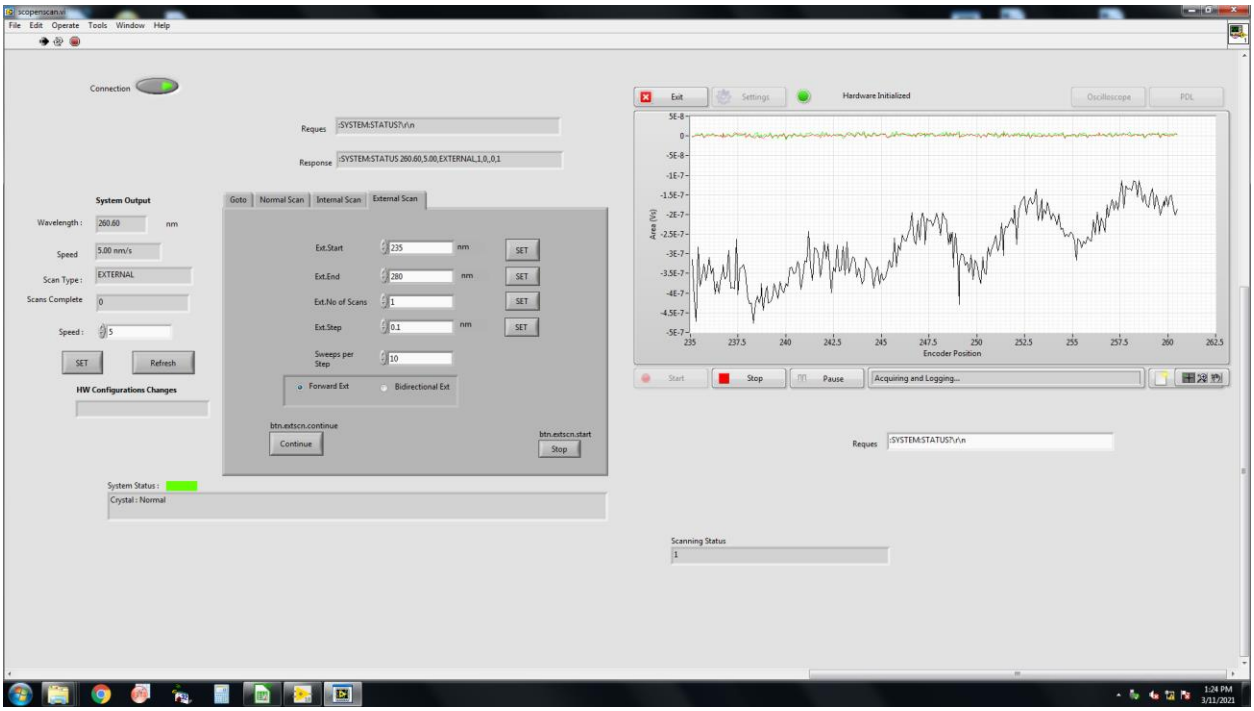

Above is the main screen pulled up immediately when launching the program. The right side of the screen is the GUI created by Travis Jones, but the scanning occurs in discreet steps with a pause at each step for a delay that is set by the user. The left side of the screen is the GUI that controls the Horizon OPO provided by Amplitude. The setting button pulls up the window shown below.

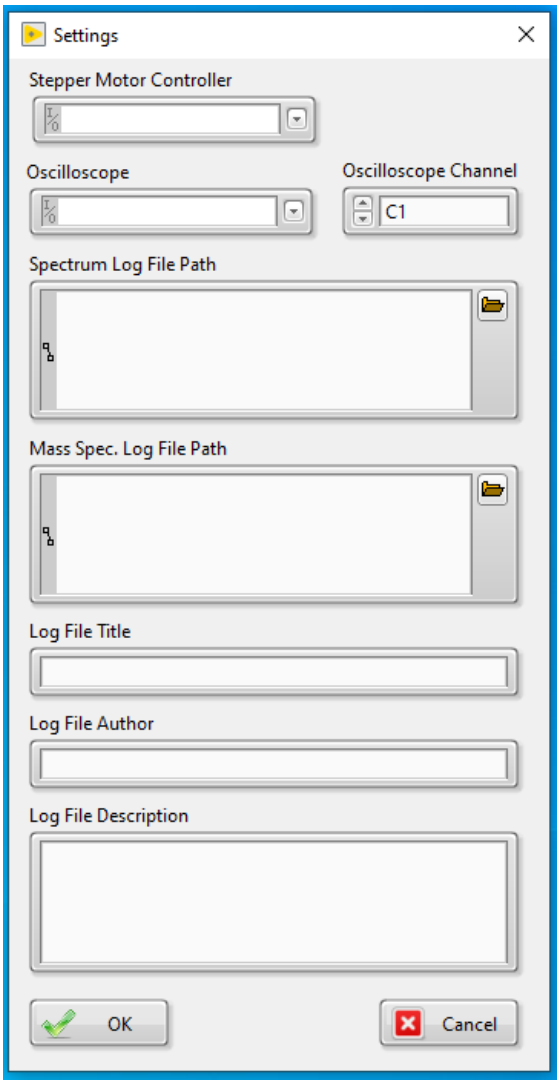

Once the settings are configured, the Oscilloscope window can be accessed, which is shown below. The Oscilloscope window shows what is recorded on the physical ‘scope, but mass peaks can be calibrated here.

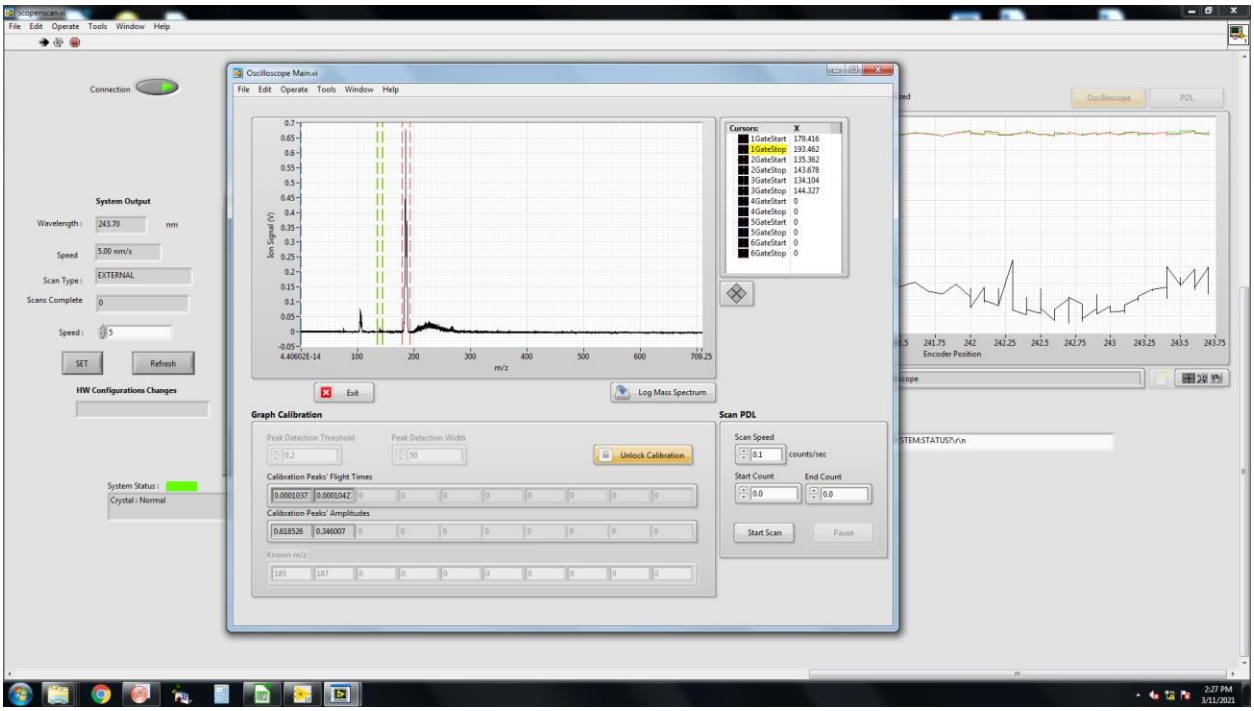
Oscilloscope Main.vi
File Edit Operate Tools Window Help
Connection
System Output
Wavelength : 243.70 nm
Speed 5.00 nm/s
Scan Type : EXTERNAL
Scans Complete 0
Speed : 5
SET
Refresh
HW Configurations Changes
System Status :
Crystal : Normal
Ion Signal (V)
m/z
Exit
Log Mass Spectrum
Cursors: X
1GateStart 179.416
1GateStop 193.462
2GateStart 135.362
2GateStop 143.678
3GateStart 134.104
3GateStop 144.327
4GateStart 0
4GateStop 0
5GateStart 0
5GateStop 0
6GateStart 0
6GateStop 0
Graph Calibration
Peak Detection Threshold
Peak Detection Width
Unlock Calibration
Calibration Peaks' Flight Times
Calibration Peaks' Amplitudes
Known m/z
Scan PDL
Scan Speed
counts/sec
Start Count
End Count
Start Scan
Pause
Encoder Position
Oscilloscope
PDL